



Physik Department

Zentralinstitut für Medizintechnik

**Advanced Cardiac Magnetic Resonance Imaging with  
Hyperpolarized  $^{13}\text{C}$  Acetate and Pyruvate**

**Ulrich Köllisch**

Vollständiger Abdruck der von der Fakultät für Physik der Technischen Universität München zur Erlangung des akademischen Grades eines

**Doktors der Naturwissenschaften (Dr.rer.nat.)**

genehmigten Dissertation.

Vorsitzende(r): Univ.-Prof. Dr. F. C. Simmel

Prüfer der Dissertation:

1. Univ.-Prof. Dr. A. Haase
2. Univ.-Prof. Dr. M. Zacharias

Die Dissertation wurde am 19.05.2015 bei der Technischen Universität München eingereicht und durch die Fakultät für Physik am 24.07.2015 angenommen.



## Abstract

Magnetic resonance imaging (MRI) is currently one of the most common imaging modalities. In classical MRI experiments, the properties of protons, namely, their concentration and relaxation behavior, make it possible to map a huge variety of injuries, tissue modifications and diseases. Carbon-13 MRI could offer a wide range of new applications by direct investigation of metabolic disorders, as they occur, for example in carcinogenic tissue. However, this was hindered by the combination of a low concentration of these nuclei and the generally low sensitivity of MR experiments, which is grounded in the low population difference between nuclear spin states. The road to in vivo  $^{13}\text{C}$  MRI was paved by the development of the concept of dissolution dynamic nuclear polarization (DNP), which directly addresses the low sensitivity by increasing the population difference by a factor of 10,000 from thermal equilibrium toward the hyperpolarized (HP) state.

The molecule most widely used with DNP is currently pyruvate, which is a marker for changes in cellular glycolytic activity, in particular in tumors. In addition to carcinogenic application, the investigation of cardiac metabolism, in which HP pyruvate conversion is altered under ischemia, is attracting interest. Recently, the short-chain fatty acid acetate has been proposed as a tracer for cardiac investigations, since its metabolism involves enzymes that regulate myocardial fatty acid consumption. Alterations in the activity arise in a variety of diseases and pathologies such as diabetic disorders, heart failure, ischemia, and obesity. Mapping acetate metabolism is challenging, since it is slower than the conversion of pyruvate, and thus the signal-to-noise ratio for the metabolite acetylcarnitine is relatively low during the time window of hyperpolarization experiments.

This work addresses this problem by developing an optimized acetate imaging framework. Spectrally selective excitation was combined with IDEAL spiral encoding and the saturation recovery technique. This enables time-resolved imaging of the conversion of acetate to its downstream metabolite acetylcarnitine. This imaging sequence was applied to investigate potential changes in cardiac acetate metabolism in healthy rats after pharmaceutical stress induction and in a rat model for diabetes mellitus. An increase in the conversion under stress was revealed in skeletal muscle but not inside the heart. The conversion rates in the myocardium, liver, and kidneys were stable under diabetes mellitus in comparison to healthy control animals. Finally, a three-dimensional imaging sequence was developed to map the cardiac conversion of HP pyruvate to lactate and bicarbonate in the porcine heart in a clinical 3 T scanner. The sequence produced accurate metabolic maps with convincing image quality and artifact behavior.

The described methods represent a worthwhile development in the implementation of acetate imaging for preclinical investigations and demonstrate potential for the implementation of clinical whole-heart imaging of cardiac metabolism in upcoming clinical trials.

## Zusammenfassung

Die Magnetresonanztomographie (MRT) ist heute in der Medizin eines der am häufigsten verwendeten bildgebenden Verfahren. In der klassischen MRT wird dafür der kernspinaktive Wasserstoffkern (Proton) genutzt, dessen Konzentration und Relaxationsverhalten vom Gewebetyp abhängig ist, so dass damit eine Vielzahl von krankhaften Veränderungen und Verletzungen lokalisiert werden kann. Das Isotop  $^{13}\text{C}$  könnte zusätzlich biochemische Informationen liefern, die es erlauben Veränderungen im Stoffwechsel, wie sie zum Beispiel in Tumorerkrankungen auftreten, zu identifizieren. Dagegen spricht allerdings die niedrige Konzentration der (dem Körper zuzuführenden Moleküle) im Zusammenspiel mit der generell niedrigen Sensitivität der MR Experiments, die in dem sehr niedrigen Besetzungsunterschied der Spin-Zustände begründet liegt. Die sogenannte Hyperpolarisation (HP) setzt genau an diesem Punkt an, indem dadurch dieser Unterschied um einem Faktor von bis zu 10,000 erhöht werden kann.

Das mit dieser Technik am häufigsten untersuchte Molekül ist Pyruvat, mit dem sich Änderungen der Glykolyseaktivität im Tumorgewebe feststellen lassen. Neben den Krebserkrankungen gibt es auch vielversprechende Ansätze, Pyruvat für die Lokalisierung von ischämischen Bereichen im Herzmuskel einzusetzen. Vor Kurzem wurde auch HP Azetat als Marker für Herzerkrankungen vorgeschlagen. In den Azetat Metabolismus sind Enzyme involviert, die die Aktivität des Fettsäurestoffwechsels regulieren, der im Herz besonders bedeutend und bei vielen Krankheiten verändert ist. Allerdings wird Azetat langsamer metabolisiert als Pyruvat. Um eine Quantifizierung in dem begrenzten Zeitintervall nach einer HP Injektion dennoch möglich zu machen wurde in dieser Arbeit eine Bildgebungssequenz entwickelt, die eine spektral-selektive Anregung von Azetat und dem Metaboliten Azetylcarnitin mit einer optimierten Akquisitionsstrategie verbindet.

Die Sequenz wurde zunächst dafür eingesetzt, Veränderungen nach pharmakologisch induziertem Stress in gesunden Ratten zu untersuchen. Hier konnte mehr Umwandlung im Rückenmuskelbereich nicht aber im Herzmuskel festgestellt werden. Der Azetat-Metabolismus wurde außerdem an einem Rattenmodell für Diabetes erforscht, dabei wurde im Herz, der Leber und den Nieren keine signifikanten Unterschiede zwischen den diabetischen und gesunden Tieren festgestellt.

Zusätzlich wurde eine Sequenz entwickelt um im HP-Experiment dreidimensionale Bilder des Pyruvat-Metabolismus im Herz von Schweinen am klinischen 3T Scanner aufzunehmen. Die entwickelte Sequenz zeichnet sich durch qualitativ hochwertige Bilder sowohl der Verteilung von Pyruvat, als auch der metabolischen Produkten Laktat und Bikarbonat aus.

Die Beschriebenen Experimente stellen eine bedeutende Entwicklung dar, indem sie metabolische Azetat Bildgebung für präklinische Studien zugänglich machen. Darüber hinaus zeigen die Pyruvat Messungen eine mögliche Sequenz, um in naher Zukunft die Bildgebung von HP Pyruvat im Herzen klinisch zu implementieren.



# Contents

|          |   |           |
|----------|---|-----------|
| <b>1</b> | <b>Introduction</b>   | <b>1</b>  |
| 1.1      | Historical Background of Magnetic Resonance Spectroscopy and Imaging . . . . .          | 1         |
| 1.2      | Metabolic Imaging with Hyperpolarized Compounds . . . . .                               | 2         |
| 1.3      | Outline . . . . .   | 3         |
| <b>2</b> | <b>Theoretical Background of Magnetic Resonance Imaging and Hyperpolarization</b>       | <b>6</b>  |
| 2.1      | Physical Principles of Magnetic Resonance . . . . .                                     | 6         |
| 2.1.1    | Nuclear Spin . . . . .  | 6         |
| 2.1.2    | Nuclear Zeeman Effect . . . . .   | 7         |
| 2.1.3    | Thermal Equilibrium . . . . .   | 7         |
| 2.1.4    | Radiofrequency Excitation . . . . .   | 9         |
| 2.1.5    | Relaxation . . . . .  | 10        |
| 2.1.6    | Chemical Shift . . . . .  | 12        |
| 2.1.7    | Bloch Equations . . . . .   | 14        |
| 2.1.8    | Free Induction Decay . . . . .  | 15        |
| 2.1.9    | Magnetic Resonance Imaging . . . . .  | 15        |
| 2.2      | Basic MRI Setup . . . . .   | 18        |
| 2.3      | Hyperpolarization . . . . .   | 19        |
| 2.3.1    | Dynamic Nuclear Polarization . . . . .  | 20        |
| 2.3.2    | Hyperpolarized $^{13}\text{C}$ Molecules . . . . .                                      | 21        |
| 2.4      | Signal to Noise Ratio for Hyperpolarization Magnetic Resonance Imaging . . . . .        | 22        |
| <b>3</b> | <b>Theory</b>   | <b>25</b> |
| 3.1      | Acetate Metabolism . . . . .  | 25        |
| 3.1.1    | Overview of the Acetate Metabolism . . . . .  | 25        |
| 3.1.2    | Chemical Shift Differentiation of the $[1-^{13}\text{C}]$ Acetate Metabolites . . . . . | 26        |
| 3.1.3    | Cardiac Acetate Metabolism under Dobutamine-Induced Stress . . . . .                    | 28        |
| 3.1.4    | Changes in Acetate Metabolism under Diabetes Mellitus . . . . .                         | 28        |
| 3.1.5    | HP Experiments with other Short Chain Fatty Acids . . . . .                             | 29        |
| 3.2      | Pyruvate Metabolism . . . . .   | 31        |
| 3.3      | Spectrospatial Pulse Design . . . . .   | 34        |
| 3.4      | Chemical Shift Imaging . . . . .  | 36        |
| 3.4.1    | CSI for Hyperpolarized $^{13}\text{C}$ Substances . . . . .                             | 36        |
| 3.4.2    | IDEAL Spiral CSI . . . . .  | 38        |

|          |  |            |
|----------|--|------------|
| <b>4</b> | <b>Experimental Setup</b>  | <b>41</b>  |
| 4.1      | Hardware . . . . .   | 41         |
| 4.2      | Preparation of [1- <sup>13</sup> C]Acetate for DNP . . . . .   | 45         |
| <b>5</b> | <b>Experiments with Hyperpolarized [1-<sup>13</sup>C]Acetate</b>   | <b>49</b>  |
| 5.1      | Spectrospatial Pulse for Alternating Acetate and Acetylcarnitine<br>Excitation . . . . .                               | 49         |
| 5.1.1    | Purpose of the SPSP Pulse . . . . .  | 49         |
| 5.1.2    | Pulse Design . . . . .   | 51         |
| 5.1.3    | In Vivo Spectroscopy . . . . .   | 53         |
| 5.2      | Metabolic Imaging of Hyperpolarized Acetate and Acetylcarnitine .  | 57         |
| 5.2.1    | Spiral <i>k</i> -Space Trajectories . . . . .  | 57         |
| 5.2.2    | Single-Timestep IDEAL Spiral CSI . . . . .   | 58         |
| 5.2.3    | Time-Resolved IDEAL Spiral CSI . . . . .   | 62         |
| 5.2.4    | Discussion . . . . .   | 66         |
| 5.3      | Investigation of the Effect of Dobutamine-Induced Stress on Acetate<br>Metabolism . . . . .                            | 68         |
| 5.3.1    | Methods . . . . .  | 68         |
| 5.3.2    | Results . . . . .  | 70         |
| 5.3.3    | Discussion . . . . .   | 76         |
| 5.4      | Investigation of Metabolic Changes in STZ-Diabetic Rats with Hy-<br>perpolarized [1- <sup>13</sup> C]Acetate . . . . . | 78         |
| 5.4.1    | Introduction . . . . .   | 78         |
| 5.4.2    | Methods . . . . .  | 78         |
| 5.4.3    | Results . . . . .  | 80         |
| 5.4.4    | Discussion . . . . .   | 82         |
| <b>6</b> | <b>3D Whole-Heart Cardiac Metabolic Imaging in the Pig with [1-<sup>13</sup>C]Pyruvate<br/>using IDEAL Spiral CSI</b>  | <b>85</b>  |
| 6.1      | Introduction . . . . .   | 85         |
| 6.2      | Methods . . . . .  | 85         |
| 6.3      | Results and Discussion . . . . .   | 90         |
| <b>7</b> | <b>Conclusion</b>  | <b>94</b>  |
| 7.1      | Summary . . . . .  | 94         |
| 7.2      | Outlook . . . . .  | 95         |
|          | <b>Literature</b>  | <b>98</b>  |
|          | <b>List of Publications</b>  | <b>111</b> |
|          | <b>Acknowledgements</b>  | <b>114</b> |



# 1 Introduction

## 1.1 Historical Background of Magnetic Resonance Spectroscopy and Imaging

Magnetic resonance imaging (MRI) is currently one of the most widely used clinical imaging modalities. Its enormous flexibility allows a broad range of applications in daily clinical praxis for diagnosis and in research on the formation of pathologies and diseases. The property of nuclear spin was shown in 1923 in the Stern-Gerlach experiment [1], which was seminal for quantum physics. This work investigated the interaction of neutral (silver) atoms with an inhomogeneous external magnetic field and thus demonstrated an intrinsic angular momentum of the particles (here stemming from the electrons) – called *spin* – associated with a magnetic moment. In the following years it was postulated and proven that several atomic nuclei possess a spin as well. The basics of nuclear magnetic resonance (NMR) were described in 1937 by Rabi [2], who showed that alternating electromagnetic fields can change the orientation of the nuclear spin. This result led to extensive investigation of the NMR response of liquids and solids, which were performed independently by Bloch [3] and Purcell [4] in 1947. Spectroscopic NMR developed into a very impressive method for studying the chemical structure of molecules. In particular, it allows the investigation of biomolecules assembled from peptides and proteins. The concept of combining NMR with spatially varying magnetic fields, published in 1973 by Mansfield [5] and Lauterbur [6], revealed the possibility of performing spatially resolved MR experiments, which is called MRI. This concept, together with technical developments, paved the way for magnetic resonance toward clinical practice, where MRI initially was applied mostly to investigate special pathologies related to soft tissue, in particular inside the central nervous system. Fast imaging strategies such as rapid acquisition with relaxation enhancement (RARE) [7] or fast low-angle shot (FLASH), [8] and the use of a multitude of receivers [9] – so-called parallel imaging techniques [10] [11] – dramatically decreased the scan time for MR images. These fast acquisition schemes are particularly interesting for cardiac acquisitions because they can reduce the effect of motion during the heart cycle on the image quality. In addition to the more rapid acquisition, novel contrast mechanisms were explored that exploit the flexibility of the technique. Functional MRI (fMRI) emerged, enabling the use of MRI not only for imaging anatomy but also for mapping complex biological properties such as the signalling pathways of nerve cells and brain function [12].

By combining spectral separation of different molecules with spatial localization of the signals, MR is in principle capable to perform metabolic imaging. In contrast to "classical" imaging, this potentially enables the investigation of the basics of diseases rather than their anatomical consequences. Observing metabolic alter-

ations opens the door to improved diagnosis and specification of diseased tissues, as well as for validation of treatment of diseases with altered cellular metabolism, such as cancer. Unfortunately, the sensitivity of conventional MR suffers from the low population difference of the spin energy states – given by the Boltzmann distribution – which makes it difficult to measure human metabolites at physiological concentrations. The low sensitivity can be improved to a limited extent by optimizing the hardware and sequences. However, direct alteration of the population difference – a technique called hyperpolarization – and the consequent increase in the signal offers a unique potential to perform metabolic MRI at reasonable resolutions *in vivo*.

## 1.2 Metabolic Imaging with Hyperpolarized Compounds

The most prominent hyperpolarization technique is called Dynamic Nuclear Polarization (DNP). It was shown that DNP can increase the polarization of molecules in aqueous solution (liquid state) up to five magnitudes for substances labeled with the MR-active isotope carbon-13 [13], which are of particular interest for investigation of metabolism *in vivo* and in cell culture. This allows real-time *in vivo* imaging of these processes for investigations of metabolic alterations as they occur in a variety of diseases in different tissues. Research on DNP applications first focused on tumor metabolism. Today, the quantification of aerobic glycolytic production of lactate from hyperpolarized (HP) pyruvate for the purpose of detecting cancer and monitoring treatment response [14] [15] [16] [17] is the most promising application. The clinical potential of this technique is currently being evaluated, and a recent trial with prostate cancer patients demonstrated the potential for clinical implementation [18]. In addition to studies of carcinogenic tissue, MR of HP  $^{13}\text{C}$ -pyruvate was investigated for exploration of cardiac metabolism in perfused hearts [19] and *in vivo* [20]. Cardiac pathologies such as ischemia [21], heart failure, and diabetic cardiomyopathy [22] were examined in rat and pig models. The investigation of cardiac disorders and injuries might be a future application for clinical trials [23].

Pyruvate metabolism serves as a marker of glycolytic metabolism; however, in the healthy human heart, the major energy contributor is fatty acid  $\beta$ -oxidation, which delivers approximately 60% to 90% of the necessary energy [24]. The preferred energy sources are altered in a variety of diseases such as heart failure, ischemia, or diabetes mellitus [25] [26] [27]. In contrast to pyruvate, acetate is metabolized in a glycolysis-independent pathway, in which several enzymes are involved, which regulate the myocardial fatty acid metabolism. Thus, acetate could serve as a marker for fatty acid metabolism and deliver valuable additional information on fuel selection in the heart.

In skeletal muscle tissue, the activity of acetyl coenzyme A synthetase (ACS)

was previously quantified by spectroscopy of HP [1-<sup>13</sup>C]acetate in rats [28]. An imaging study measured the distribution of HP acetate in the porcine myocardium on a clinical 3 T scanner without acquiring signals from the metabolites [29]. In isolated rat hearts, acetate studies revealed high potential for identification of an ischemic environment [30]. To obtain clinically relevant information using HP acetate, it is crucial to localize the activity of the metabolism in order to localize pathological changes in the heart, which was not shown previously.

Therefore, the major focus of this work was the establishment of an imaging sequence for acetate and its intermediate metabolite acetylcarnitine (ALCAR), which faces the objection of much lower metabolite concentrations of the metabolite during the time window of the hyperpolarization experiment.

The challenge of imaging with HP substances generally lies in the irreversible decay of the nonequilibrium population difference. The polarization – and with it the measureable magnetization – decays within about one minute; furthermore, every acquisition uses some of the magnetization. Therefore, only fast metabolic pathways, such as the conversion of pyruvate to lactate, alanine, and CO<sub>2</sub>, can be monitored. Exploring new potential substrates requires a careful optimization of the substrate toward high polarization levels and low relaxation rates, as well as the design of sequences tailored to the application of interest.

### 1.3 Outline

To provide the reader with background information, **chapter 2** briefly describes the basic theory of magnetic resonance, the concept of spatial encoding with gradients, and the technical setup for MRI. Furthermore, the physics related to the HP state and the basic concepts of the DNP technique are explained.

An overview of the metabolic pathways of acetate and pyruvate is given in **chapter 3**, as well as a detailed explanation of the concepts used for the implemented imaging sequences. Potential changes in cardiac acetate metabolism under stress and modifications associated with diabetes mellitus are analyzed. Furthermore, cardiac pyruvate metabolism is illustrated. The theory of the spectral separation technique IDEAL ([31]), a very efficient way of encoding information on molecules with different chemical shifts, is explained, and considerations regarding the design and implementation of two-dimensional (2D), spectrally and spatially selective radiofrequency (RF) pulses are presented.

**Chapter 4** gives a brief overview of the technical setup regarding the MR scanners, polarizers, coils, and other hardware used in the different labs this work was carried out. This chapter contains the preparation and optimization of the acetate recipe.

All the MR experiments with hyperpolarized [1-<sup>13</sup>C]acetate are described in **chapter 5**. The design, implementation and in vivo application of a spectrospatial (SPSP) pulse tailored to the two frequencies of interest is described. This

pulse was combined with an IDEAL spiral imaging sequence to improve the image quality by reducing artifact contamination of the ALCAR maps. In time-resolved ALCAR imaging, the saturation recovery technique enables quantitative analysis of the acetate conversion over several timepoints. The developed techniques were applied to investigate the effect of dobutamine-induced stress on acetate conversion. Finally, the application of the technique to the investigation of cardiac, liver and renal acetate metabolism in a rat model for diabetes mellitus is described.

In **chapter 6**, the development of a pulse sequence for three-dimensional (3D) in vivo imaging of the porcine pyruvate metabolism in the heart is explained, and promising metabolic maps of the myocardium over the entire left ventricle are presented.

The conclusion (**chapter 7**) summarizes the results of this work and gives an outlook for further applications of DNP and cardiac imaging. Finally, it presents some brief thoughts about the future development of the field of Hyperpolarization for preclinical science and clinical applications.



## 2 Theoretical Background of Magnetic Resonance Imaging and Hyperpolarization

### 2.1 Physical Principles of Magnetic Resonance

#### 2.1.1 Nuclear Spin

The principle of NMR is the interaction of nuclear magnetic moments inside an external field with an electromagnetic wave. These magnetic moments arise from the spin property some nuclei have. The combination of nucleons (the number of neutrons and protons in a nucleus) can produce a total intrinsic magnetic moment called the nuclear spin. This property is represented by the spin quantum number  $I$ .

| Nucleus         | $I$           | $\gamma$ [ $\frac{\text{MHz}}{\text{T}}$ ] | nat.ab. [%] |
|-----------------|---------------|--|-------------|
| $^1\text{H}$    | $\frac{1}{2}$ | 267.5                                      | 99.98       |
| $^2\text{H}$    | 1             | 41.1                                       | 0.015       |
| $^{12}\text{C}$ | 0             | –  | 98.89       |
| $^{13}\text{C}$ | $\frac{1}{2}$ | 67.3                                       | 1.1         |
| $^{14}\text{N}$ | $\frac{1}{2}$ | 19.3                                       | 99.60       |
| $^{15}\text{N}$ | 1             | -27.1                                      | 0.37        |
| $^{16}\text{O}$ | 0             | –  | 99.76       |
| $^{19}\text{F}$ | $\frac{1}{2}$ | 251.8                                      | 100.00      |

Table 1: NMR properties of some isotopes: Nuclear spin  $I$ , gyromagnetic ratio  $\gamma$  and natural abundance. Note that two of the most frequent isotopes in organic molecules,  $^{12}\text{C}$  and  $^{16}\text{O}$ , are NMR-silent.

The magnetic moment  $\boldsymbol{\mu}$  of a nucleus is proportional to the spin  $\boldsymbol{I}$ :

$$\boldsymbol{\mu} = \gamma \boldsymbol{I} \quad (1)$$

The proportionality constant  $\gamma$  is called the gyromagnetic ratio and depends on the isotope. It is an important factor for NMR experiments, as it defines the strength of the interaction of nuclei with external electromagnetic fields (Figure 1). The NMR-relevant properties of several nuclei are given in Table 1.

### 2.1.2 Nuclear Zeeman Effect

For a nucleus with the spin quantum number of  $I$ ,  $2I+1$  quantum mechanical eigenstates exist; however, these states are degenerated without an external field. As for any other magnetic moment, this degeneration vanishes if the nucleus is located inside an external magnetic field; this principle is called the Zeeman effect [32]. The field specifies one direction in space, referred to as the  $z$  direction; the projection of the spin onto this  $z$  direction is quantized as well. This quantization is expressed by the secondary spin quantum number  $m$ , which represents the eigenstates

$$m = -I, -I + 1, \dots, I - 1, I \quad (2)$$

and their  $2I+1$  dedicated eigenvalues:

$$m\hbar \quad (3)$$

The reduced Planck constant  $\hbar$  physically corresponds to the quantum of angular momentum, as it was first postulated by Niels Bohr.

In this work, the nuclei of the isotopes  $^1\text{H}$  and  $^{13}\text{C}$  are relevant. They both have the spin quantum number  $I = 1/2$ , so the two eigenstates  $m = \pm 1/2$  are possible inside a magnetic field, which leads to two possible magnetic moments in the  $z$  direction:

$$\mu_z = \gamma I_z = \pm \frac{1}{2} \gamma \hbar \quad (4)$$

and therefore to two energy levels:

$$E_{\pm} = \mu_z B_0 = \frac{1}{2} \mp \hbar \gamma B_0 \quad (5)$$

Transitions between these states are possible, fulfilling the spin and the energy conservation law, which says that a spin-one particle (a photon) with the energy  $\Delta E$  and the Larmor frequency  $\omega_L$  has to be emitted or absorbed (Figure 1).

$$\Delta E = \hbar \gamma B_0 = \hbar \omega_L \quad (6)$$

### 2.1.3 Thermal Equilibrium

In an MR experiment, a very large number ( $N$ ) of nuclear spins, which is called a spin ensemble, is considered in each voxel. Inside the field  $B_0$ , one of the two states (considering a spin-1/2 nucleus) is more populated, as it has a lower energy. For a positive gyromagnetic ratio, as is the case for most NMR-active nuclei (e.g.,  $^1\text{H}$  and

$^{13}\text{C}$ ; see Table 1), the state with the nuclear spin aligned along the magnetic field has a lower energy. The population of the two states ( $N_+$  and  $N_-$ ) is statistically given by the Boltzmann distribution

$$\frac{N_-}{N_+} = e\left(-\frac{\gamma\hbar B_0}{k_B T}\right) \quad (7)$$

where  $T$  is the temperature of the system, and  $k_B$  is the Boltzmann constant. As  $N_+ > N_-$ , the ensemble of  $I$  spins  $i$  yields a net magnetization in the  $z$  direction.

$$M_z = \sum_i \mu_i = (N_+ - N_-)\hbar\omega_L \quad (8)$$

The relative population difference  $\frac{N_+ - N_-}{N_+ + N_-}$  of the spin system at thermal equilibrium depends on the ratio of the energy difference  $\Delta E$  and the available thermal energy  $k_B T$  [eq. (7)]. At room temperature ( $T = 293$  K) and the field strength of a clinical MR scanner ( $B_0 = 3$  T), the thermal energy is orders of magnitude higher. Thus, the population difference is only about 20 parts per million (ppm) for the gyromagnetic ratio of  $^1\text{H}$  and 7 ppm for that of  $^{13}\text{C}$ . As the net magnetization  $M_z$  generates the ability to perform MR experiments, the low population difference, and hence the low net magnetization, is the reason for the inherently low sensitivity of NMR. An increase in the population difference leads to a stronger imbalance of the two states. This is the basic principle of the hyperpolarization technique and will be described in chapter 2.3 in more detail.

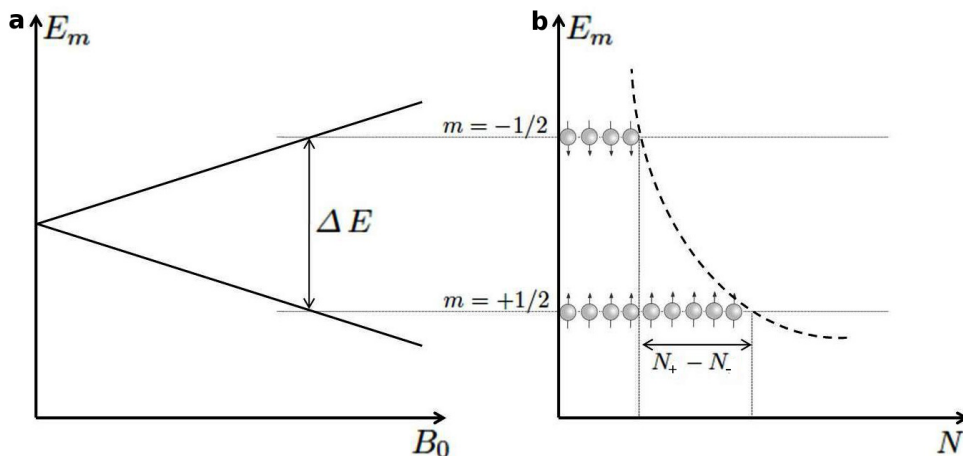


Figure 1: Energy diagram of a spin-1/2 nucleus. a: Energy gap  $\Delta E$  increases with the external magnetic field; the slope of the graph is determined by the gyromagnetic ratio  $\gamma$ . b: The states are populated according to the Boltzmann distribution (from [33]).

### 2.1.4 Radiofrequency Excitation

In an external static field, any magnetization precesses with the Larmor frequency  $\omega_L$  around the field vector. This rotating magnetic dipole sends an electromagnetic wave, which can be received by induction of an alternating voltage in a coil. To generate the rotation, the magnetization has to be tipped away from the  $z$  direction. Therefore, the thermal equilibrium has to be disturbed by an additional external electromagnetic field. An RF field  $\mathbf{B}_1$ , applied to the ensemble at the Larmor frequency of the nuclei ( $\omega_{RF} = \omega_L$ ) rotates the net magnetization away from the longitudinal  $z$  direction toward the transverse  $xy$  plane. The definition of a frame that rotates with the Larmor frequency  $\omega_L$  helps us to understand this process, called excitation, in a classical view: In the rotating frame, the static magnetic field  $\mathbf{B}_0$  can be neglected, as it is already accounted for by the frame selection. An external field  $\mathbf{B}_1$  rotating with the Larmor frequency  $\omega_L$  in the laboratory frame corresponds to a static field in the rotating frame. Here, the trajectory of the magnetization vector  $\mathbf{M}$  can be interpreted as precession around  $\mathbf{B}_1$  with the Larmor frequency referring to the RF field  $\omega_1 = \gamma B_1$  (see Figure 2).

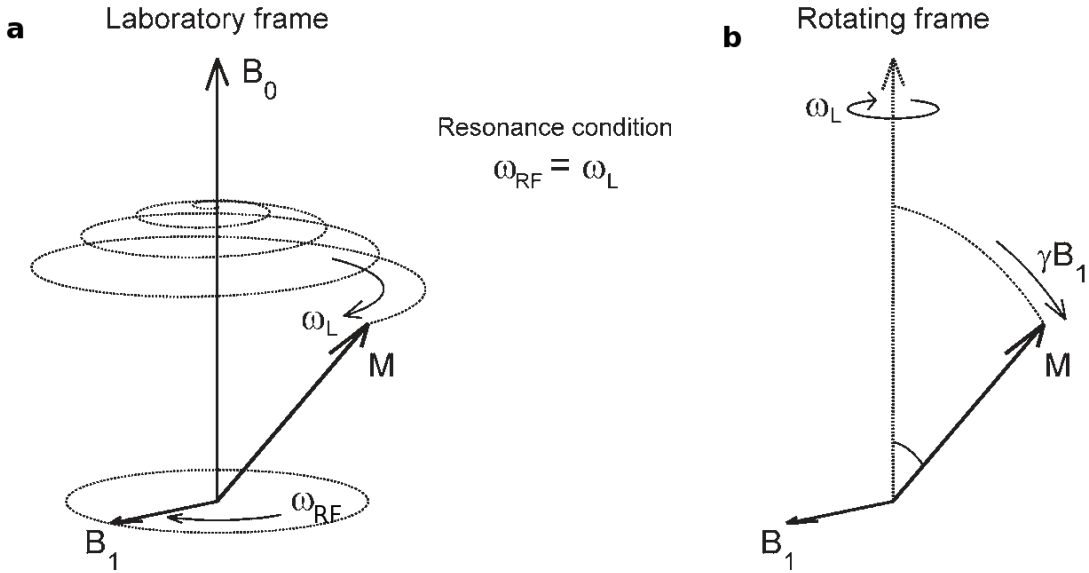


Figure 2: A resonant rotating field  $\mathbf{B}_1$  tips the magnetization  $\mathbf{M}$ . a: In the laboratory frame, the magnetization vector precesses helically on the surface of a sphere. b: In the rotating frame, the resonant field  $\mathbf{B}_1$  is static (resonance condition), inducing rotation of  $\mathbf{M}$  toward the  $xy$  plane (from [34]).

The RF field, with a constant amplitude  $B_1$  and a duration of  $\tau$ , rotates the magnetization vector  $\mathbf{M}$  from the  $z$  axis towards the  $xy$  plane by the flip angle  $\vartheta$

$$\vartheta = \omega_1 \Delta t = \gamma B_1 \Delta t \quad (9)$$

Starting with a magnetization  $M_0$  in the  $z$  direction, the transverse and longitudinal magnetizations can easily be calculated (see Figure 2).

$$M_{xy} = M_0 \sin(\vartheta) \quad \text{and} \quad M_z = M_0 \cos(\vartheta) \quad (10)$$

## 2.1.5 Relaxation

### Longitudinal Relaxation

During excitation, the thermal equilibrium of the ensemble is disturbed by the application of a field  $B_1$  via an RF pulse. Subsequently, the system has a statistical tendency to return to thermal equilibrium. The time constant defining the speed of this process is called the longitudinal relaxation time  $T_1$ . The longitudinal relaxation process during the time  $t$  can be described phenomenologically by a differential equation:

$$\frac{dM}{dT} = \frac{M_0 - M_z}{T_1} \quad (11)$$

with the solution

$$M_z(t) = (M_z(0) - M_0)e^{-t/T_1} + M_0 \quad (12)$$

The physical reason for longitudinal relaxation (spin–lattice relaxation) is energy exchange between the spins and their surroundings (the lattice). Since the molecules, and therefore the nuclear spins in an ensemble, are moving, they are influenced magnetically by their environment. This happens by dipole–dipole interactions (dipolar coupling), chemical shift anisotropies, or electric quadrupole moments. Thus, the spins experience fluctuations in the local field  $B_0$ , which result in a nonzero probability of transitions between the energy states and therefore in relaxation of the ensemble. The speed of this dynamic process depends strongly on the external physical factors of the molecule inside the investigated probe, such as the temperature, solution viscosity or magnetic field strength. However, the time  $T_1$  also depends on the environment surrounding the spin of interest inside the molecule.  $^{13}\text{C}$  nuclei that are geometrically close to one or more  $^1\text{H}$  nuclei (for example, inside a methyl group  $^{13}\text{CH}_3$ ) exhibit faster longitudinal relaxation (lower  $T_1$ ) than spins with no NMR active nucleus as nearest neighbors (for example, inside a carboxylic group  $^{13}\text{COOH}$ ).

The longitudinal relaxation time  $T_1$  is a very important factor for evaluating a molecule as a potential tracer for HP MR. Since the HP state is a nonequilibrium state, the longitudinal magnetization  $M_z$  decays as

$$M_z(t) = (M_z(0) - M_0)e^{-t/T_1} + M_0 \approx M_z(0)e^{-t/T_1} \quad (13)$$

Note that the thermal magnetization  $M_0$  can be neglected when hyperpolarization generated by DNP is considered because the magnetization at the end of the dissolution process,  $M_z(0)$  (see chapter 2.3), is about 10,000 times higher.

### Transverse Relaxation

The mechanism for relaxation of transverse magnetization is described as transverse or spin–spin relaxation. An ensemble contains transverse magnetization if the many single spins inside the ensemble rotate coherently around the  $z$  axis. However, if the external magnetic field is not perfectly homogeneous – as is the case in any practical setup – each spin rotates with a slightly different Larmor frequency  $\omega_L$ . Therefore, the ensemble of spins loses its correlation, so the transverse magnetization of the ensemble decays (see Figure 3). The local field can vary owing to molecular interactions, as quantified by the transverse relaxation time  $T_2$ , or owing to inhomogeneities of the  $B_0$  field itself, as described by  $T_{2inho}$ . The latter variations occur, for example, because of susceptibility changes inside a biological probe, which induce a locally changing magnetic field.

Since both relaxation factors have the effect of dephasing the transverse magnetization, they are summarized by the combined time constant  $T_2^*$ , which is called the effective transverse relaxation time:

$$\frac{1}{T_2^*} = \frac{1}{T_2} + \frac{1}{T_{2inho}} \quad (14)$$

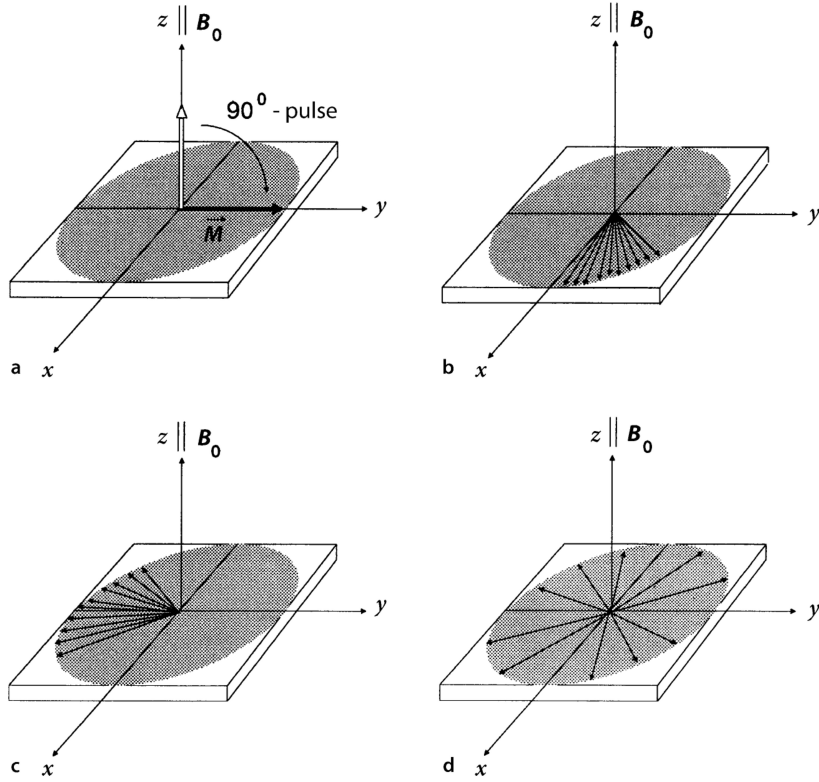


Figure 3: Transverse relaxation: The transverse magnetization  $M_{xy}$  of the ensemble consists of many rotating magnetization components. a: Immediately after the RF pulse, the magnetizations rotate coherently. b to d: They precess with slightly differing Larmor frequencies around  $z$ , so they lose their coherence; thus, the macroscopic transverse magnetization decays. (From [34])

### 2.1.6 Chemical Shift

As mentioned in chapter 2.1.5, the molecular environment influences the relaxation behavior of a nucleus because the nucleus experiences field distortions from neighboring atoms. This leads to slightly different magnetic fields “seen” by nuclei at different positions inside a molecule and, therefore, to different Larmor frequencies  $\omega_{L,i}$ . The electron shells of the atoms inside the molecule diamagnetically shield the external field  $B_0$ , lowering the local Larmor frequency, which can be expressed using the shielding constant  $\sigma_i$ .

$$\omega_{L,i} = \omega_L(1 - \sigma_i) \quad (15)$$

The shielding depends on the intramolecular distance from the nucleus of interest to neighboring atoms, the type of electron bonds, and the type of binding partners, because all of these parameters change the electron density in the region surrounding the nucleus. The factor  $\sigma$  is in the range of  $\sim 1\text{--}200$  ppm; consequently, the exact frequencies of a spin ensemble provide information about the structure of a molecule. This makes it possible to quantify the concentration of different molecules with distinct chemical shifts by measuring their spectroscopic intensity using NMR. As an example, Figure 2.1.6 shows  $^1\text{H}$  spectra acquired in voxels of the human brain in a region inside a glioma (a) and in a healthy area of the brain (b). Here, alterations in the concentration of several molecules (for example, lactate, N-acetylaspartic acid, creatine, and choline) can provide information about the pathological status of the tissue. As a standard [35], the chemical shift is usually referred to the frequency of tetramethylsilane in chloroform as reference to define 0.0 ppm on the chemical shift scale of  $^1\text{H}$  and  $^{13}\text{C}$  MR.

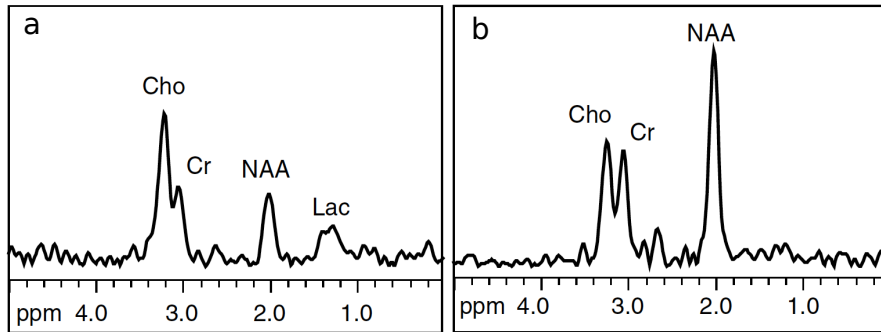


Figure 4: Example of chemical shift spectroscopy with voxel-selective spectroscopy inside the human brain. Malignant glioma tissue (a) shows elevated concentrations of choline (Cho) and lactate (Lac) and reduced levels of N-acetylaspartic acid (NAA) compared to healthy tissue (b). Figure reprinted from [36].

### 2.1.7 Bloch Equations

The time evolution of the macroscopic magnetization  $\mathbf{M}(t)$  can be described mathematically by the Bloch equations, a set of coupled differential equations. They include the influence of an external magnetic field  $\mathbf{B}(t)$ , which applies a torque to the magnetization, as well as the relaxation processes described above.

$$\dot{\mathbf{M}} = \begin{pmatrix} \dot{M}_x(t) \\ \dot{M}_y(t) \\ \dot{M}_z(t) \end{pmatrix} = \gamma \begin{pmatrix} (\mathbf{M}(t) \times \mathbf{B}(t))_x \\ (\mathbf{M}(t) \times \mathbf{B}(t))_y \\ (\mathbf{M}(t) \times \mathbf{B}(t))_z \end{pmatrix} - \begin{pmatrix} \frac{M_x(t)}{T_2^*} \\ \frac{M_y(t)}{T_2^*} \\ \frac{M_z(t) - M_0}{T_1} \end{pmatrix} \quad (16)$$

Consider the example of excitation by a resonant RF pulse with the Larmor frequency,  $\omega_{RF} = \omega_L$ , and a constant amplitude  $B_1$  for a duration of  $\tau$  (chapter 2.1.4).

This is represented by a constant magnetization vector  $B_1 = (B_1, 0, 0)$  (for  $t < \tau$ ) in the rotating frame (here, along the  $x$  axis), as depicted in Figure 2. If  $\tau$  is short compared to the relaxation rates  $T_1$  and  $T_2^*$ , the relaxation term in eq. (16) can be neglected:

$$\begin{pmatrix} \dot{M}_x(t) \\ \dot{M}_y(t) \\ \dot{M}_z(t) \end{pmatrix} = \begin{pmatrix} 0 \\ \gamma M_z B_1 \\ -\gamma M_y B_1 \end{pmatrix} \quad (17)$$

If we assume that at the beginning of the pulse ( $t = 0$ ) the system was in thermal equilibrium, with the magnetization vector aligned along the  $z$  direction,  $\mathbf{M}_0(t) = (0, 0, M_0)$ , the system is solved by:

$$\begin{pmatrix} M_x \\ M_y \\ M_z \end{pmatrix} = \begin{pmatrix} 0 \\ M_0 \sin(\gamma B_1 t) \\ M_0 \cos(\gamma B_1 t) \end{pmatrix} \quad (18)$$

This result mathematically describes the rotation of the magnetization during an RF pulse where  $B_1$  is directed along the  $y$  axis in the rotating frame (see eq. (10); Figure 2).

### 2.1.8 Free Induction Decay

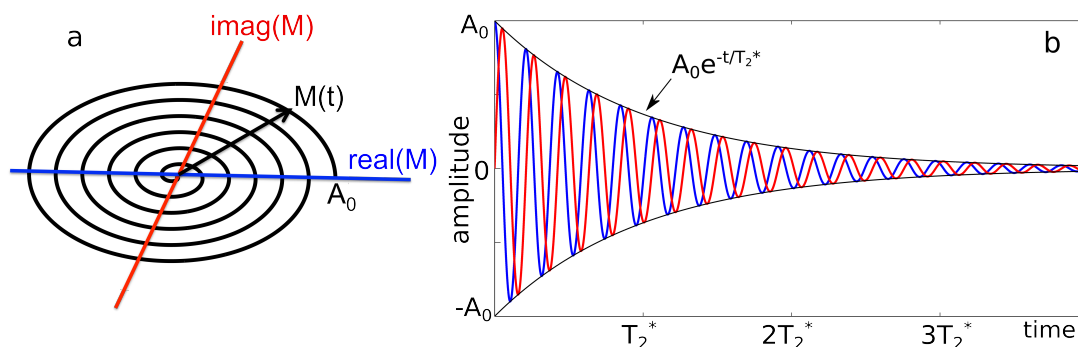


Figure 5: Free induction decay: a: The transverse magnetization vector rotates on a spiral in the transverse plane. b: The signal can be interpreted as a complex number with alternating real and imaginary parts and decaying amplitude. The development of the MR signal without any external disturbance (e.g., a gradient field) is called free induction decay (FID).

After excitation [consider an excitation around the  $y$  plane in the rotating frame, as in eq. (16)], the direction of the ensemble's initial magnetization is static. In the laboratory frame (where measurement with the RF-coil takes place), however, the magnetization rotates with the Larmor frequency. At the same time, it decays because of transversal relaxation (Figure 3). The combination of these two movements leads to a spiral trajectory of the transverse magnetization vector  $\mathbf{M}(t)$  (Figure 5a). The rotating magnetization creates an electromagnetic wave, which is recorded with the RF coil. The signal is split into two signal channels by the introduction of a  $90^\circ$  phase shift for one of the two channels. This concept enables the detection of two orthogonal signals, the  $x$  (by definition the real part of  $\mathbf{M}$ ) and the  $y$  (imaginary part of  $\mathbf{M}$ ) components. Now the  $x$ - $y$  magnetization can be described by the imaginary number  $M(t)$  (Figure 5b).

### 2.1.9 Magnetic Resonance Imaging

To acquire spatial information, the classical one-dimensional (1D) NMR experiment described above is expanded by applying a locally varying magnetic field  $B_0$  and, therefore, causing the Larmor frequency to be a function of the spatial coordinates  $\omega_L(x, y, z)$ . This principle, published by Sir Peter Mansfield [5] and Paul Lauterbur [6] in 1973, won them the Nobel Prize in Physiology and Medicine in 2002. The Larmor frequency for the field  $\mathbf{B}_0$  superimposed with the gradient field  $\mathbf{G}(x, y, z)$  can be expressed as

$$\omega_L(x, y, z) = \gamma(B_0 + \mathbf{G} \cdot \mathbf{r}) = \gamma(B_0 + G_x x + G_y y + G_z z) \quad (19)$$

The signal  $dS$  originating from a spin ensemble in the volume  $dV$  located at the position  $\mathbf{r}$  with the local spin density  $\rho(\mathbf{r})$  is then given by

$$dS(t) = \rho(\mathbf{r}) \exp(i(\gamma B_0 + \gamma \mathbf{G} \cdot \mathbf{r})t) \quad (20)$$

Considering this inside the rotating frame, which means physically demodulating the signal at the receiver with the Larmor frequency  $\omega_L = \gamma B_0$ , the first part of the exponent vanishes. Volumetric integration of eq. (20) yields

$$S(t) = \int \int \int \rho(\mathbf{r}) \exp(i\gamma \mathbf{G} \cdot \mathbf{r}t) d\mathbf{r} \quad (21)$$

This illustrates that the applied gradient dephases the signal. Transverse relaxation was neglected in eq. (20), so eq. (21) holds true for strong gradients, where the phase spread due to the gradients is much larger than the dephasing due to transverse relaxation. With the definition of the reciprocal, the so-called  $k$ -space vector [37]

$$\mathbf{k}(t) = \int d\mathbf{k} = \int \frac{\gamma \mathbf{G}(t)}{2\pi} dt \quad (22)$$

the spin density  $\rho(\mathbf{r})$  and the signal in  $k$ -space  $S(\mathbf{k})$  become a Fourier pair:

$$S(\mathbf{k}) = \int \int \int \rho(\mathbf{r}) \exp(i2\pi \mathbf{k} \cdot \mathbf{r}) d\mathbf{r} \quad (23)$$

$$\rho(\mathbf{r}) = \int \int \int S(\mathbf{k}) \exp(-i2\pi \mathbf{k} \cdot \mathbf{r}) d\mathbf{k} \quad (24)$$

The reconstruction of the data acquired at discrete  $k$ -space positions to calculate the pixels of the image,  $\rho(\mathbf{r})$ , is an inverse 3D discrete Fourier transformation.

### Slice Selection

In most MRI experiments,  $k$ -space encoding is not performed in all three spatial directions (which is called a 3D sequence). As shown in Figure 6, the magnetization can be excited in a distinct slice of the probe (slice thickness  $\Delta z$ ) by a slice-selective pulse. Therefore, an RF pulse with the bandwidth  $\Delta\omega$  is combined with the gradient  $G_z$ .

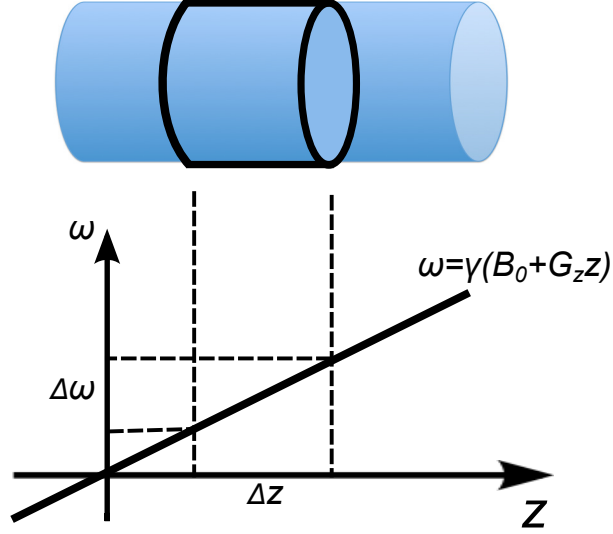


Figure 6: The spectral bandwidth  $\Delta\omega$  and applied gradient strength  $G_z$  define the thickness of the excited slice.

With slice-selective excitation, 2D gradient encoding can be performed to acquire the image inside the selected slice. Eq. (23) simplifies to

$$S(k_x, k_y) = \int \int \rho(x, y) \exp(i2\pi(k_x x + k_y y)) dx dy \quad (25)$$

Since the signal at one point in the  $k$ -space,  $(k_x, k_y)$ , is the Fourier transform of the spin density  $\rho(x, y)$ , the reconstruction of the image from the data  $[S(k_x, k_y)]$  is an inverse Fourier transform. For Cartesian  $k$ -space coordinates, this is usually computed using a fast Fourier transform (FFT) [38]. For non-Cartesian encoding patterns, such as spirals, either the encoding matrix in eq. (25) has to be calculated and inverted numerically, or the  $k$ -space data are interpolated onto a Cartesian grid with a subsequent Fourier transformation of the data [39].

## 2.2 Basic MRI Setup

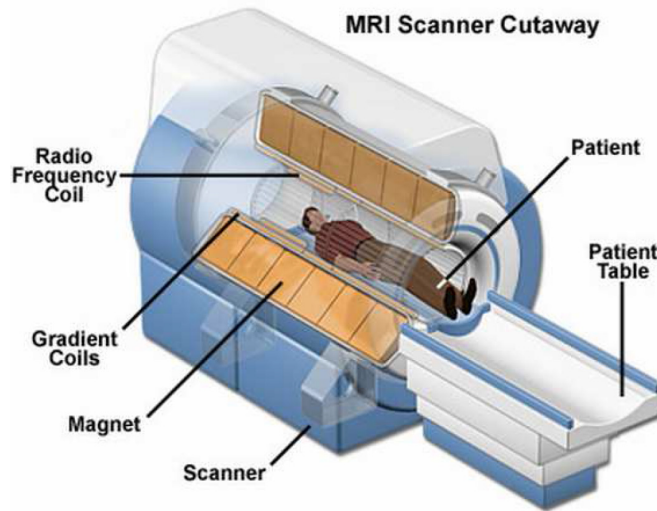


Figure 7: Scheme of a whole-body MRI scanner (from [40]).

The MRI scanner hardware consists of three main parts. A large magnet generates the external magnetic field  $B_0$ . In clinical systems, this is a superconducting coil cooled with liquid helium. Most clinical scanners operate at a field strength of 1.5 T or 3 T; however, human scanners operating at 7 T are available. The second part is the gradient system, which contains several coils inside the magnet. They create the time-dependent alternating magnetic fields necessary to localize the signal inside the patient's body (chapter 2.1.9). The third system is the transmission and reception system, in which the RF coil is the first and most important part: It excites and receives the signals for MR experiments via electromagnetic induction. In addition to the coil itself, there are several components involved in the receive chain, such as amplifiers, digitizers, and a computer that finally handles the data and performs the reconstruction to visualize the results. A schematic drawing of the structure of an MRI scanner is shown in Figure 7.

## 2.3 Hyperpolarization

As described in chapter 2.1.3, the population difference between the two states of spin-1/2 nuclei is very low at regular (body) temperature levels. The polarization of a two-energy ( $E_{\pm}$ ) system can be defined as the relative population difference

$$P = \frac{N_- - N_+}{N_- + N_+} \quad (26)$$

Insertion of the Boltzmann distribution [eq. (7)] into eq. (26), in combination with the definition of the hyperbolic tangent function, yields the expression

$$P = \tanh\left(\frac{\gamma\hbar B_0}{2k_B T}\right) \quad (27)$$

The concept behind hyperpolarization techniques is to disturb the thermal equilibrium, that is, to transfer more nuclei into the lower-energy state. Since the signal-to-noise ratio (SNR) is proportional to the polarization, this offers an immense potential for increasing the signal in order to gather metabolic information *in vivo*. Several methods of realizing the HP state have been proposed.

- Brute force: Thermal polarization is applied at extremely low temperatures in very strong magnetic fields [see eq. (27)]. Rapid heating and a transition to a moderate field of the MR scanner leaves the probe in the nonequilibrium (polarized) state. However, for  $^{13}\text{C}$  probes, an extremely low temperature (millikelvins) would be needed to reach high ( $\sim 10\%$ ) polarization levels.
- Spin-exchange optical pumping (SEOP) can be used to hyperpolarize noble gases ( $^3\text{He}$  and  $^{129}\text{Xe}$ ). This procedure is based on the polarization of the unpaired electron spins of alkali metals by irradiation with circularly polarized light. Their polarization can be transferred to the nuclear spins of noble gases during gas-phase collisions [41].
- Parahydrogen-induced polarization exploits the correlation between nuclear spins in parahydrogen, which react chemically to move toward the  $^{13}\text{C}$  or  $^{15}\text{N}$  nuclei of interest. The polarization of the protons is transferred by RF-based or field-cycling approaches [42]. The advantage of this technique is that it creates the HP state rapidly (in seconds). However, it modifies the molecules of interest, and the polarization levels are not high compared to those obtained by DNP.
- The DNP technique is based on the transfer of spin polarization from electrons to nuclei via microwave irradiation using suitable radicals at low temperature inside a strong magnetic field. This technique is most suitable for  $^{13}\text{C}$  molecules and will be described below.

### 2.3.1 Dynamic Nuclear Polarization

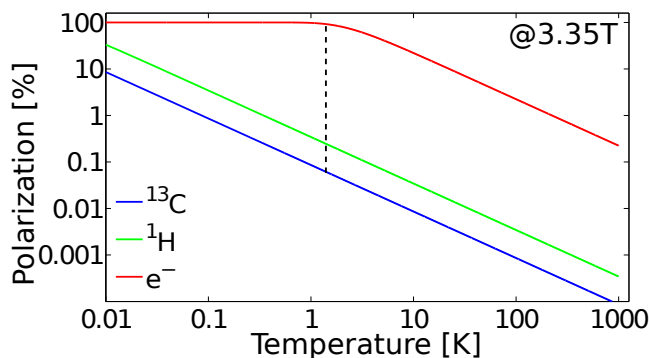


Figure 8: Polarization level of  $^{13}\text{C}$ ,  $^1\text{H}$ , and electrons versus temperature  $T$  at 3.35 T in a double-logarithmic plot [eq. (27)].

It is evident from eq. (27) that the thermal polarization level depends not only on the external factors of temperature and magnetic field, but also on the gyromagnetic ratio  $\gamma$ . Since electrons have a gyromagnetic ratio that is 660 times larger than that of protons and 2600 times larger than that of  $^{13}\text{C}$ , their thermal polarization level is generally higher. Temperature-dependent polarization is illustrated in Figure 8 for these three  $\gamma$  values at a magnetic field of 3.35 T. In this field, the  $^{13}\text{C}$  polarization at low temperatures (e.g., 1 K) is still relatively low (less than 0.1%); however, the electrons are already polarized by more than 90%. The basic idea of the DNP method is to transfer polarization from unpaired electrons to  $^{13}\text{C}$  nuclei. Therefore, the molecule of interest (e.g.,  $[1-^{13}\text{C}]$ pyruvate) is mixed with a stable free radical inside a solvent, which forms a glass matrix at low temperature. If this probe is then irradiated inside the magnetic field with a high-frequency microwave field with a frequency equal to the Larmor frequency of the electrons, the electron polarization can be partially transferred to the  $^{13}\text{C}$  nuclei [13]. The time scale for polarization build-up is about one hour. In the final step of this process, the probe is rapidly melted and dissolved in a heated solution to obtain an injectable liquid for in vivo applications. This can be performed with low polarization losses in a few seconds, so a final polarization of up to 20%–40% can be reached, depending on the chemical structure of the molecule of interest.

### 2.3.2 Hyperpolarized $^{13}\text{C}$ Molecules

There is a huge variety of molecules that are interesting for examination of in vivo metabolism using the DNP technique. However, they have to fulfill several criteria to be suitable for this technique.

For biomedical applications, it is important that the in vivo longitudinal relaxation rate  $T_1$  has a reasonable value so that biological processes can occur during the observation period. The HP probe has to be dissolved, transferred to the animal or human, and injected into the blood. Then the substrate is distributed via blood circulation to the organ of interest. If metabolism occurs inside the cell, the molecule must be transported into the cytosol or even into the mitochondria, where finally the metabolic step of interest takes place.

Owing to the comparatively high gyromagnetic ratio  $\gamma$  of protons, their time  $T_1$  is relatively short (water protons,  $\sim 1.5$  s) [43]. However, spin-1/2 nuclei with a lower  $\gamma$  can have much longer relaxation times. Several isotopes were proposed for hyperpolarization, among them the noble gas  $^3\text{He}$  [44] for lung imaging and  $^{15}\text{N}$  molecules [45], which are characterized by long  $T_1$  values [46], making them particularly interesting for perfusion measurements. However,  $^{13}\text{C}$  is of special biochemical and medical interest, since the labeled organic molecules are incorporated into the cellular metabolism. Thus, they can serve as markers for pathological changes in a variety of diseases, including changes in tumors [47] [16], malfunctions in cardiac [23] [48] or renal [49] metabolism, or metabolic changes during diabetes [50].

The natural abundance of the isotope is only about 1% , so the background signal is negligible. However, the components used for HP experiments have to be labeled with  $^{13}\text{C}$  at the position best suited for the experiment to increase the detection sensitivity.

## 2.4 Signal to Noise Ratio for Hyperpolarization Magnetic Resonance Imaging

### SNR in MR

Together with the contrast and artifact occurrence, the SNR is the most important characteristic of MR image quality. It is dependent of the overall performance of the hardware components, pulse sequence and reconstruction for a specific application.

The SNR can be measured phenomenologically by dividing the signal strength of a region of interest ( $ROI_{sig}$ ) by the background noise derived from a region outside of the probe, where no signal is expected ( $ROI_{noise}$ ). This can be calculated using the standard deviation in the noise area; however, since the noise in a magnitude image is not Gaussian but is Rice distributed, a factor of  $(2 - \frac{\pi}{2})$  has to be taken into account [51]:

$$SNR = \sqrt{2 - \frac{\pi}{2}} \frac{\text{mean}(ROI_{sig})}{\text{std}(ROI_{noise})} \quad (28)$$

The SNR generally depends on the acquired voxel size  $\Delta V$ , the number of averages  $N_{av}$ , the acquisition time  $T_{aq}$ , the system resistance  $R$  (which includes the resistance of the receiver circuit and the measured object), and finally, the effective temperature  $T_{eff}$  of the measured object and the receiver circuit.

$$SNR \propto \frac{\sqrt{\Delta V N_{av} T_{aq}}}{4k_B T_{eff} R} \quad (29)$$

It is obvious that a high resolution, which means a small voxel volume  $\Delta V$ , decreases the SNR. For any SNR-limited MRI technique, the appropriate resolution is a trade-off between the SNR necessary for robust information and the precision needed for tissue differentiation (e.g., healthy tissue or tumor). For HP  $^{13}\text{C}$  MRI, the low in vivo concentrations and relatively rapid  $T_1$  decay in vivo limit the resolution to an order of about 0.5 cm.

### Hyperpolarized Signal Properties

Since the HP ensemble is not in thermal equilibrium, the magnetization is non-renewable and decaying (chapter 2.3). In addition to thermal relaxation, which is quantified by the longitudinal relaxation time  $T_1$ , each excitation by a pulse with the flip angle  $\vartheta$  converts the spin ensemble toward thermal equilibrium. By simple geometric considerations, the signal intensity of the  $k^{\text{th}}$  excitation of a series is related to the previously applied flip angles  $\vartheta_i$  and the actual flip angle  $\vartheta_k$ :

$$I_k \propto M_0 \prod_{i=1}^{k-1} \left\{ e^{\left(\frac{-T_R}{T_1}\right)} \cos(\theta_i) \right\} \sin(\theta_k) \quad (30)$$

with the repetition time  $T_R$ , longitudinal relaxation time  $T_1$ , and initial magnetization  $M_0$ .

### SNR in Multichannel Arrays

When data acquired with multiple coils are reconstructed, it is important to review the method for combining the single-channel data. Summing up the data before reconstruction leads to incoherence in the acquired data and, therefore, loss of SNR because of phase shifts in the individual receiver circuits. If the coil sensitivities of an array are not known, it is SNR-optimal to reconstruct an image  $i_c$  for each channel  $c$  and finally combine the images in a sum-of-squares sense for each pixel [52].

$$I(x, y) = \sqrt{\sum_{c=1}^C i_c(x, y)^2} \quad (31)$$



## 3 Theory

### 3.1 Acetate Metabolism

Several of the enzymes involved in acetate metabolism play an important role in the regulation of fatty acid oxidation. In contrast to pyruvate, free coenzyme A (CoA) and acetate are esterified in a glycolysis-independent pathway. Thus, acetate serves as a marker for fatty acid metabolism and delivers valuable additional information on fuel selection, especially in the myocardium.

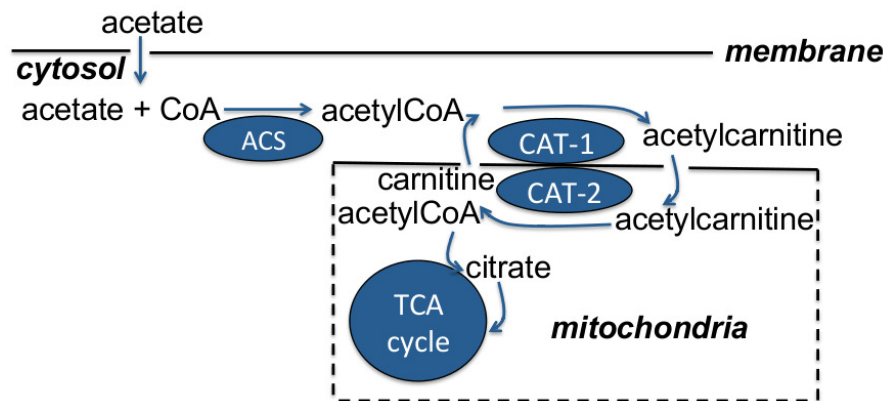


Figure 9: Overview of acetate metabolism: Acetate is activated by ACS to acetyl coenzyme A (AcCoA). After conversion to ALCAR via carnitine acetyltransferase (CAT-1), it can enter the mitochondria. There, ALCAR is converted back to AcCoA (via CAT-2), which can be metabolized in the tricarboxylic acid (TCA) cycle. (Figure previously published in [53]).

Acetate is the unprotonated ionic form of acetic acid, a short-chain fatty acid. It is metabolized in skeletal muscle cells [28], and particularly in myocardial muscle cells [54] [30]. In the body, acetate is usually a low-concentration molecule; however, it is produced from ethanol in the liver [55]. Furthermore, it can be taken up in the gastrointestinal tract after heterolactic fermentation by fecal microbes [56].  $[1-^{13}\text{C}]$ acetate (Figure 10a) has a relatively large longitudinal relaxation time  $T_1$ , which makes this labeling favorable for HP experiments (see chapter 2.1.5).

#### 3.1.1 Overview of the Acetate Metabolism

An overview of acetate metabolism is shown in Figure 9; this scheme is valid for myocardial and skeletal muscle cells as well as acetate metabolism in the kidneys

and liver.

From the blood, acetate is transported into the cytosol and ACS converts it to acetyl coenzyme A (AcCoA) in the initial metabolic step (Figure 10a). The concentration of ACS is comparatively high in the rat myocardium and renal cortex, but lower in the liver [57]. This reaction is inhibited under ischemic conditions because of a low concentration of free CoA [30], so acetate might be a valid marker for myocardial ischemia.

AcCoA can be transformed into ALCAR; this process is catalyzed by carnitine acetyltransferase (CAT) (see Figure 10b), specifically, CAT-1 residing on the outer mitochondrial membrane [58]. CAT-1 is a key enzyme in the regulation of fuel selection, in particular in myocardial muscle cells. This enzyme is effectively inhibited by malonyl-CoA, which is the first step in fatty acid biosynthesis. Fatty acid and glucose consumption are interdependent; this glucose–fatty acid cycle is referred to as the Randle cycle [59]. An alteration of the malonyl-CoA level leads to a decrease in ALCAR production and hence less oxidation of AcCoA (and acyl-CoA). This shifts the preferred energy source of the heart away from fatty acids toward glucose [24]. Cardiac alterations in this fuel selection occur in a variety of diseases and pathologies such as diabetes mellitus [60] or cardiomyopathy [61] [62].

A similar effect was observed in tumor tissues, in particular in prostate tumors. Human tumors incorporate acetate in order to catabolize the lipids necessary for their growth [63]. Hence, fatty acid synthesis is upregulated, which includes increased production of malonyl-CoA and inherently decreased CAT-1 activity [64]. Therefore, acetate uptake into tumors was investigated by positron emission tomography (PET) [65] [66], and HP acetate could potentially be used to investigate the tumor uptake in vivo [67]. In addition to PET, HP acetate studies might have the potential to quantify changes from acetate consumption toward fatty acid synthesis.

After the two described enzymatic reactions (ACS and CAT-1), the product ALCAR can be transferred into the mitochondria via the carnitine shuttle system. Here it is converted back into AcCoA (via CAT-2), which enters the TCA cycle and is oxidized for energy production. The product of the first step, after AcCoA is shuttled into the TCA cycle, is citrate.

### 3.1.2 Chemical Shift Differentiation of the [1-<sup>13</sup>C]Acetate Metabolites

The cytosolic AcCoA pool is regulated and maintained to be over 10 times smaller than that of ALCAR [54], so this intermediate metabolite has a very low SNR in MR experiments, even when HP compounds are used. The small chemical shift difference between [5-<sup>13</sup>C]citrate and [1-<sup>13</sup>C]acetate (Figure 10d) makes it difficult to distinguish the citrate signal from the acetate peak during in vivo experiments at a field strength of 3 T. Thus, in studies performed in this work using clinical

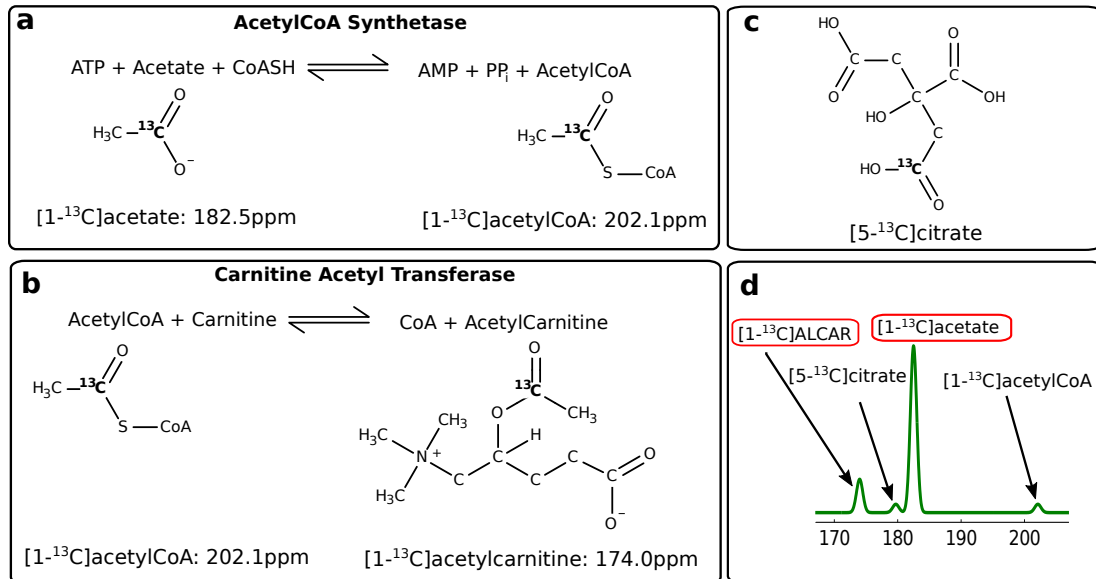


Figure 10: a: Acetylation of CoA via ACS: Acetate is bound to CoA at the thiolic (SH) group and forms AcCoA. b: CAT catalyses the formation of free CoA and ALCAR, which can be transported into the mitochondria. The activity of CAT-1 is the key mechanism controlling fuel selection in the myocardium. c: Citrate is the first product of the TCA cycle. d: The chemical shifts of interest for the metabolic products after [1-<sup>13</sup>C]acetate injection.

3 T scanners, the focus was on the quantification of the [1-<sup>13</sup>C]acetate and [1-<sup>13</sup>C]ALCAR signals.

### 3.1.3 Cardiac Acetate Metabolism under Dobutamine-Induced Stress

Dobutamine is a catecholamine that is primarily a  $\beta_1$ -adrenoreceptor agonist. It has a positive inotropic effect, which increases the strength of cardiac contractions, and a positive chronotropic effect, which increases the heart rate. To match the higher energy demand in the left ventricle under dobutamine-induced stress, the myocardial blood flow, and therefore the myocardial oxygen uptake, increase [68]. The higher demand for fuel in the myocytes leads to increased uptake of fatty acids [69] [70]. In perfused piglet hearts, dobutamine reportedly produces a higher proportion of esterified carnitine (as ALCAR) in the total carnitine pool, which also increases, as a reaction to the stress [71]. In perfused rat hearts, enhanced acetate oxidation with increased workload of the heart was observed; however, the oxidation of longer-chain fatty acids was more affected [72].

### 3.1.4 Changes in Acetate Metabolism under Diabetes Mellitus

Diabetes is one of the most common chronic diseases; it is accompanied by changes in glucose and fatty acid metabolism, in particular in the heart [24] [50] [27], but also in other organs such as the liver [73] or kidneys [49].

In diabetes mellitus, the upregulation of fatty acid consumption at the cost of glycolysis is mediated by CAT-1 [24]. This key enzyme is effectively inhibited by malonyl-CoA. The myocardial malonyl-CoA concentration depends on the blood insulin level [74]. Under diabetic insulin deficiency, increased malonyl-CoA decarboxylase activity and expression was detected in diabetic rats, whereas the AcCoA carboxylate activity was constant [60]. This decreases the concentration of malonyl-CoA and consequently lowers the inhibition of CAT-1 (Figure 11). This fact may be important for the high fatty acid oxidation rates in diabetic hearts. In agreement with this, it was shown that the malonyl-CoA concentration is lowered in pig hearts with streptozotocin (STZ)-induced diabetes [69]. In summary, this suggests the hypothesis investigated in chapter 5.4 that myocardial conversion of acetate to ALCAR might be increased under diabetic conditions.

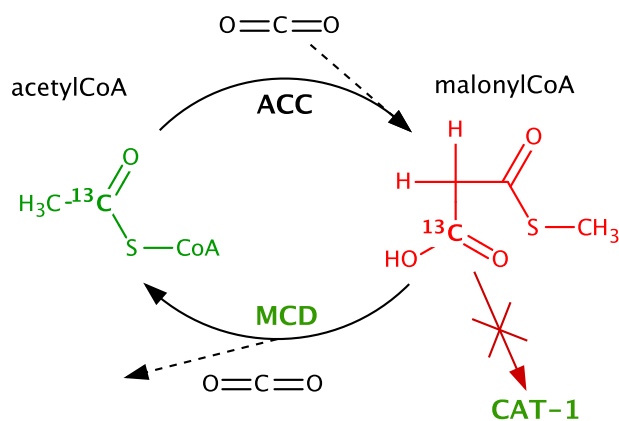


Figure 11: The enzyme malonyl-CoA decarboxylase (MCD) is more active under diabetes, leading to more decarboxylation of malonyl-CoA. Since the AcCoA carboxylase (ACC) activity is not affected, the malonyl-CoA concentration decreases. Consequently, there is less inhibition of CAT-1.

Free fatty acids (FFAs) concentration in plasma is increased under insulin deficiency. This increases the level of lipids in the liver, causing increased ketone body production and reduced conversion of acetate to FFAs. Under this condition, the ACS activity might decrease [73].

It has previously been reported that there is a correlation with declining renal function and reduced uptake of acetate and reduced renal clearance as seen in diabetic nephropathy (DN) [75]. DN is directly connected with renal hypoxia [76], which was recently shown to alter the renal pyruvate metabolism in STZ-diabetic animals [49] [77]. The reduced consumption of acetate in diabetic kidneys most likely occurs because a lower amount of AcCoA is oxidized through the TCA cycle. However, it is not clear whether there is decreased activation of acetate via AcCoA to the membrane-transportable molecule ALCAR.

### 3.1.5 HP Experiments with other Short Chain Fatty Acids

The use of acetate as a marker for fatty acid metabolism and the conversion of acetate via ALCAR lacks the ability to directly investigate the  $\beta$ -oxidation of fatty acids. Here, the length of the fatty acid gets reduced inside the mitochondria by cleaving two carbons in every cycle to form one acetylCoA. This is not the case for acetate, since the two-carbon aliphatic tail of acetate is too short to go through this reaction. The four-carbon fatty acid butyrate has been proposed recently for DNP experiments and demonstrated to be a suitable substrate to reveal additional information about cardiac metabolism in the perfused rat heart and in vivo [78] [79]. More specifically, the intermediate step of the  $\beta$ -oxidation, the ketone-bodies

acetoacetate and  $\beta$ -hydroxybutyrate, could be detected as well as ALCAR, built from acetylCoA, the end product of the  $\beta$ -oxidation and the TCA-cycle products citrate and glutamate. Yet, it has to be shown, whether this approach can also be suitable for preclinical in vivo studies, because the SNR of the metabolites is very low, which makes it difficult to draw quantitative conclusions. The challenge here is, that the polarization reached for HP butyrate is lower (7%) and the  $T_1$ -time of the (compared to acetate) bigger molecule was reported to be relatively short (20 s in the dissolution media).

## 3.2 Pyruvate Metabolism

Pyruvate is the final product of glycolysis, the intracellular pyruvate metabolism can serve as a marker to study the cellular energy metabolism and its changes during diseases such as cancer [14] [16] [80] and ischemia [81] [48] [50].

Pyruvate is transported into the cell, where the majority of it is reduced to lactate by the coenzyme nicotinamide adenine dinucleotide (NADH). This rapid reaction is catalyzed by the enzyme LDH. In the organism the lactate concentration is much higher than the pyruvate concentration, the rapid exchange of the HP  $^{13}\text{C}$  label from pyruvate to lactate via LDH is able to detect altered lactate concentrations in the tissue [82]. Alternatively, pyruvate undergoes transamination with glutamate to form alanine; this reaction is catalyzed by alanine transaminase (ALT). LDH and ALT cause reversible reactions inside the cytosol. Finally, pyruvate can enter the mitochondria, where it is catalyzed via the enzyme pyruvate dehydrogenase (PDH) to  $\text{CO}_2$  and AcCoA, which subsequently can enter the TCA cycle for further energy production. The produced  $\text{CO}_2$  is rapidly interconverted with bicarbonate via carbonic anhydrase. After an injection of HP  $[1-^{13}\text{C}]$ pyruvate  $[1-^{13}\text{C}]$ lactate,  $[1-^{13}\text{C}]$ alanine, and  $[1-^{13}\text{C}]$ bicarbonate are detectable. Figure 12 gives an overview of the reactions, the chemical formulas, and the chemical shift of the molecules of interest.

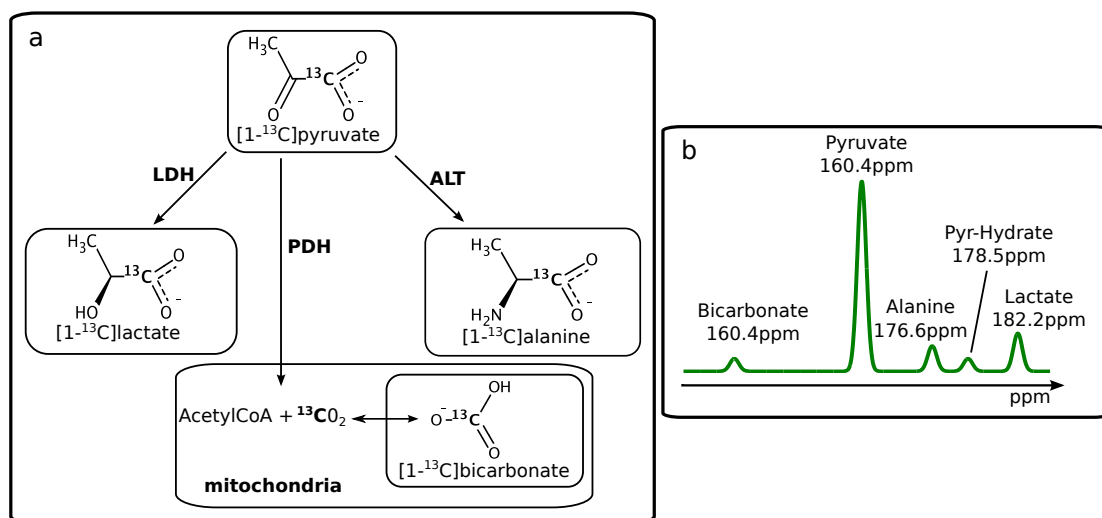


Figure 12: a: Overview of the metabolic pathways of  $[1-^{13}\text{C}]$ pyruvate: In the cytosol,  $[1-^{13}\text{C}]$ lactate and  $[1-^{13}\text{C}]$ alanine can be produced via LDH and ALT, respectively. Pyruvate can enter the mitochondria, where it is catalyzed to  $^{13}\text{CO}_2$ , which is in rapid interconversion with  $[1-^{13}\text{C}]$ bicarbonate. b: The chemical shifts of interest after infusion of  $[1-^{13}\text{C}]$ pyruvate.

### **Pyruvate in Tumors**

In healthy tissue, lactate conversion via LDH is highest when oxygen levels are reduced, e.g., in muscle cells under high workload. Tumors exhibit a high level of lactate formation even in the presence of oxygen, an effect referred to as the Warburg effect [83] [84]. Tumor studies with mice indicate an increase in lactate formation after HP pyruvate injection with increasing tumor grade [15]. Furthermore, the flux of the HP  $^{13}\text{C}$  label between pyruvate and lactate was found to decrease after drug treatment in vitro and in vivo [47] [16]. Hence, the change in pyruvate metabolism measured using DNP is a potential early marker of tumor progression as well as of response to chemotherapeutic treatment.

### **Pyruvate in the Myocardium**

Furthermore, detection of the metabolic products of HP [1- $^{13}\text{C}$ ]pyruvate was also demonstrated in vitro [81] and in vivo in the myocardial muscle of pigs [48] and rats [50]. Spectra of HP [1- $^{13}\text{C}$ ]pyruvate and its products have been shown to provide information about myocardial ischemia, viability, and nutrient selection [23]. In necrotic myocardial tissue, lactate,  $\text{CO}_2$ , and the resulting bicarbonate cannot be produced from HP [1- $^{13}\text{C}$ ]pyruvate. Brief ischemia (10 min) in isolated hearts was associated with increased lactate but lowered bicarbonate signals. The hearts recovered under reperfusion after the ischemic phase, as indicated by a normalization of oxygen consumption, mechanical function, and high-energy phosphate concentration. With this recovery, the lactate and bicarbonate values returned to normal [81]; these results are reprinted in Figure 13. Hence, the presence of lactate proves delivery and transport of pyruvate into the cytosol, as well as LDH activity. This evidently shows the viability of the myocardial tissue. The presence of HP bicarbonate furthermore demonstrates flux through PDH inside the mitochondria, which is a negative indicator for an ischemic area. This makes chemical shift imaging (CSI) with HP [1- $^{13}\text{C}$ ]pyruvate a highly interesting field for potential clinical diagnosis in patients with left ventricular dysfunction, since the differentiation of nonviable, viable but ischemic, and healthy tissue is of particular interest for planning appropriate treatment. This information cannot be extracted using other metabolic imaging modalities such as PET or single-photon emission computed tomography (SPECT), since these techniques cannot provide information about the metabolic state of the tracer. This inherently limits the interpretation of the images, which depend on the metabolism, tracer transport, and perfusion in regard to metabolic information.

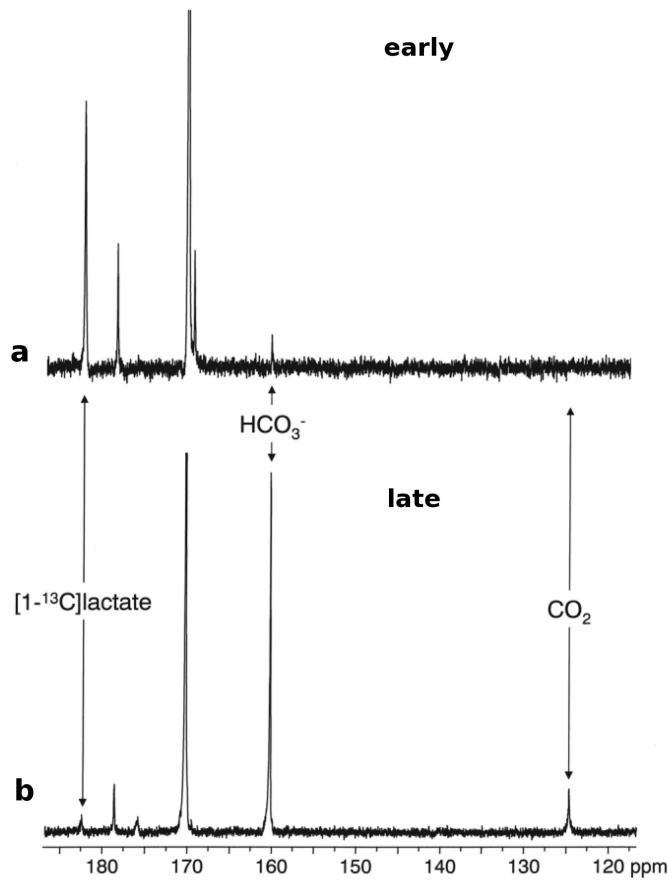


Figure 13: Spectra acquired during perfusion of isolated rat hearts with HP [1- $^{13}\text{C}$ ]pyruvate. Soon after ischemia, induced for 10 min, the (still viable) myocardium produces much more lactate than  $\text{CO}_2$  (represented by bicarbonate in aqueous solution). The PDH activity is stopped by the lack of free CoA. Under reperfusion, the  $\text{CO}_2$  production normalizes to the values measured previously. Thus, HP pyruvate can serve as a marker for both viability and ischemia in myocardial tissue. Figure redrawn from [81].

In addition to ischemia, the PDH activity could be an interesting diagnostic pattern in diabetes, since it changes with myocardial fuel selection. Increased lactate conversion (via LDH) at the cost of  $\text{CO}_2$  conversion (via PDH) was observed with HP pyruvate in rats with induced type-1 diabetes mellitus [54] (see also chapter 3.1.4).

### 3.3 Spectrospatial Pulse Design

SPSP pulses are 2D RF pulses that combine a frequency-selective (spectral) and a slice-selective (spatial) excitation [85]. These pulses were initially developed for targeted excitations of fat and water in proton imaging [86], where they can be used for fat–water excitation as well as for suppression. It was further demonstrated that SPSP pulses are advantageous for metabolic imaging of HP  $^{13}\text{C}$  compounds [87]. Here, efficient use of the decaying and nonreplenishing magnetization is crucial. Excitation by a flip angle  $\vartheta$  causes the HP magnetization to decay by a factor of  $\cos \vartheta$  (chapter 2.3). The injected HP substrate (e.g., pyruvate) usually has a much higher signal than its metabolites (e.g., lactate and bicarbonate). Therefore, the substrate can be excited using a lower flip angle; thus, less magnetization is lost. The metabolite(s), however, need to be acquired with a higher flip angle to obtain reasonable image quality. Different molecules with different chemical shifts can be excited using separate alternating excitations of the substrate and metabolite [87] [88] [89] or within the same excitation using a so-called multiband pulse [90] [91]. Separate excitation has the advantage that the spectral pulse design is less demanding, so the pulse can be designed with a shorter duration, hence reducing the  $T_2^*$  decay during the pulse. With the multiband approach (applied for cardiac pyruvate imaging in chapter 6), the measured metabolic maps can be acquired at the same time with different flip angles for different frequencies. However, this method requires an additional spectral encoding scheme (see chapter 3.4.2).

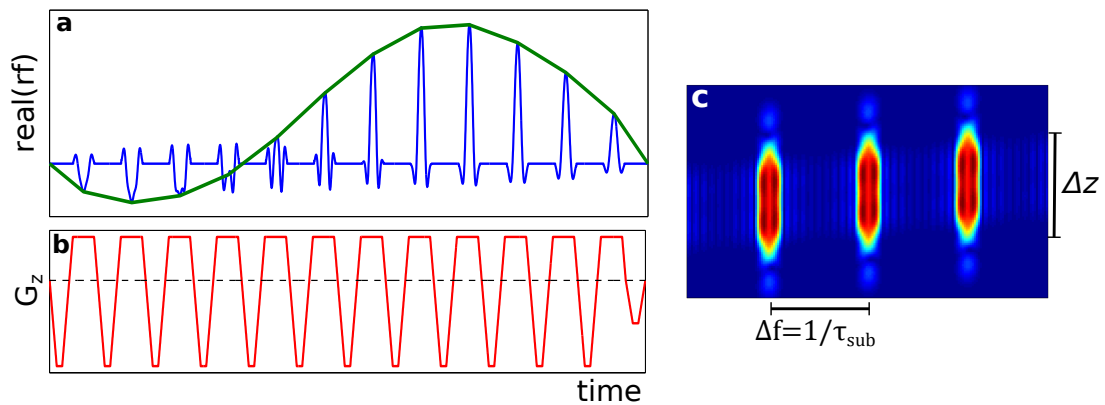


Figure 14: Shape of an SPSP pulse combining an RF pulse (a) with an alternating flyback  $z$  gradient (b). The resulting SPSP profile (c) was calculated using the Bloch equations and the small-tip-angle approximation.

The 2D excitation can be expressed using the  $k$ -space interpretation of the gradient during excitation, which is derived from the small-tip-angle approximation

for the solution of the Bloch equations [92]. Repeated coverage of the (spatial)  $k_z$  space adds the time domain as a Fourier transform of the spectral domain. This allows additional spectrally selective excitations [85]. Typically, the bandwidth required for the spatial dimension is much larger than that for the spectral dimension. Therefore, the relatively short sublobes define the encoding of the spatial dimension, for example, with Gaussian or Sinc-shaped subpulses. For the spectral dimension, only a limited number of points (number of sublobes) is available. The time between two sublobes  $\tau_{sub}$  defines the frequency distance  $\Delta f$  of the aliasing pattern in the spectral domain (Figure 14c). The overall envelope of the pulse (green line in Figure 14a) determines the spectral pulse profile.

In pulse design, first the number of sublobes has to be defined. This is a trade-off, as a very large number requires longer RF pulses and hence larger signal losses due to  $T_2^*$  decay. Lowering the number of sublobes, however, degrades the spectral profile. Second, the gradient shape  $G_z(t)$  has to be set. Several alternating gradient profiles are possible, which have different aliasing patterns (for a more detailed description, see [93]). The so-called flyback gradient (shown in Figure 14b) is a very robust approach in which the RF pulse is active only during the constant gradient. The maximal gradient strength and slew rate are used only during the return to the start of the  $k_z$  line.

The spatial  $k$ -space trajectory is defined by  $k_z(t) = \frac{2\pi}{\gamma} \int G(t') dt'$  (see chapter 2.1.9). For the spectral domain, the  $k$ -space can be defined as the inverse frequency domain, which is equivalent to the time domain  $k_\omega(t) = T - t$ , where  $T$  is the total pulse duration. For numerical calculation and simulation of the pulse profile from a known pulse shape, the pulse has to be discretized onto  $N$  timepoints  $t_n$ , so the spectral-spatial  $k$ -space  $(k_{z,n}, k_{\omega,n})$  also has  $N$  points. Then, the excitation with the discrete RF shape  $\rho(t_n) = \rho_n$  can be described using the so-called forward model:

$$b_m = A_{m,n}(k_n) * \rho_n \quad (32)$$

The discrete spectral-spatial profile has  $M$  points  $b_m$  at the spatial position  $z_m$  and the spectral frequency  $f_{\omega,m}$  and follows from the pulse shape via the excitation matrix  $A_{m,n}(k_n)$  [93].

$$A_{m,n} = \exp(-2\pi i(z_m k_{z,n} + f_{\omega,m} k_{\omega,n})) \quad (33)$$

With the known excitation matrix  $A_{m,n}$  [eq. (33)] and the desired 2D excitation profile  $b_n$ , the inverse problem of eq. (32) has to be solved in order to calculate the RF pulse  $\rho_n$ . This overdetermined ( $m > n$ ) problem can be solved in a linear least squares sense:

$$\rho_n = (A_{m,n}^T A_{m,n})^{-1} (A_{m,n}^T b_m) \quad (34)$$

## 3.4 Chemical Shift Imaging

### 3.4.1 CSI for Hyperpolarized $^{13}\text{C}$ Substances

The huge potential of the DNP technique is its ability to map metabolic processes with CSI in real time. Quantitative kinetic information about the metabolism is of huge interest, as alterations in the conversion rates of several enzymatic reactions are key characteristics of diseases and pathologies. The challenge for this technique, however, lies in the nonrenewability of the HP spin state.

The signals of different molecules can be separated by their chemical shift in the spectral domain (chapter 2.1.6). The time development of the signals after injection of the substrate has to be recorded to obtain information about the enzymatic activity. Metabolic mapping for preclinical or clinical applications is used to detect the sources of the signals inside a region of interest (ROI), e.g., an organ. Therefore, 3D spatial encoding has to be performed (see chapter 2.1.9). This produces five-dimensional information overall, which needs to be encoded very efficiently, as the magnetization decays with the experimental time and additionally with every excitation.

In the past few years, many CSI approaches for HP  $^{13}\text{C}$  substances have been published, most of them adapted from proton MR spectroscopy imaging sequences. FIDCSI [47] [16] is a straightforward encoding strategy. A FID (and, via Fourier transformation, a spectrum) is acquired with a preceding phase-encoding gradient to scan the  $k$ -space pointwise using multiple excitations (Figure 15a). Because this is a time-inefficient encoding scheme, typically only one chemical-shift-resolved image is acquired before the HP signal has decayed.

Frequent coverage of a  $k$ -space line after a single excitation is more efficient. This scheme acquires the signal recorded at each  $k$ -space position at several timepoints and therefore encodes the spectral information. One application of this approach is echo-planar spectroscopic imaging (EPSI) [15] [94], in which the readout direction of a Cartesian  $k$ -space pattern ( $k_x$ ) is covered repeatedly for each phase-encoding step ( $k_y$ ) (Figure 15b). This is basically the same principle as described in chapter 3.3 for the case of excitation.

A non-Cartesian  $k$ -space sampling pattern can be chosen, e.g., for spiral CSI [95] [96] (Figure 15c), which can further reduce the number of necessary acquisitions; however, it might require more challenging gradient performance. A very efficient CSI pattern is obtained by combining spatial encoding by a spiral  $k$ -space trajectory with the IDEAL approach for the spectral domain.

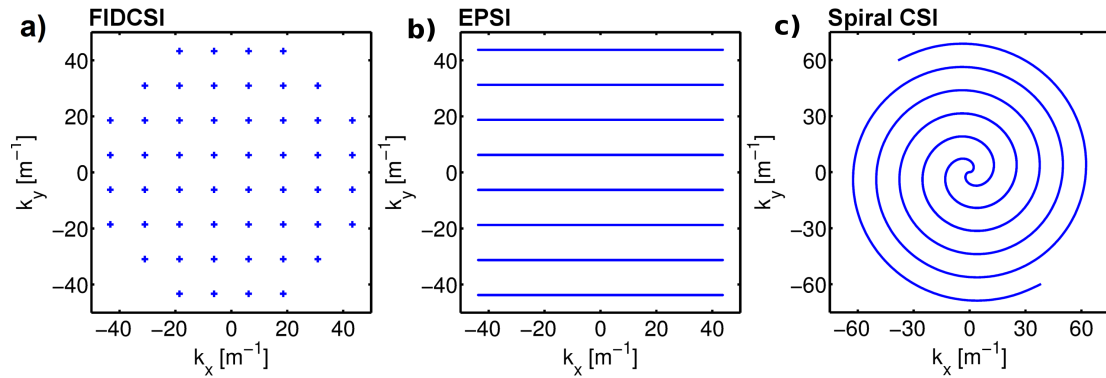


Figure 15: Different encoding schemes for HP CSI; in this example, an 8.0 cm field of view is encoded with a real resolution of 1.0 cm. a: With FIDCSI, a FID is acquired at each  $k$ -space point. After a 3D Fourier transform, a complete spectrum is available at every image position; however, this approach requires many excitations. b: After one excitation, EPSI covers each  $k$ -space line several times, which provides more time-efficient encoding (less excitations per chemical-shift-resolved image). c: The same principle can be applied using non-Cartesian trajectories, such as spirals, and the number of acquisitions per image can be further reduced. Here a two-arm spiral is shown as the  $k$ -space trajectory. Figure redrawn from [97].

For a detailed comparison of the described sequences, the reader is referred to [97]. Here we describe a detailed simulation framework of different CSI sequences as well as in vivo tests of the performance of these sequences applied in rats with subcutaneous tumors. For the  $^{13}\text{C}$  imaging studies presented in this work, IDEAL spiral CSI was used.

### 3.4.2 IDEAL Spiral CSI

The basic concept behind IDEAL (Iterative decomposition with echo asymmetry and least-squares estimation) was initially developed for fat–water separation in proton imaging [31]. Therefore, the known frequency difference  $\Delta\omega$  between fat and water can be used to calculate two images with at least two excitations acquired with different echo times  $T_{E,p}$  adapted for  $\Delta\omega$ , which is a development of the Dixon method [98]. The IDEAL approach was previously applied for the frequency set of HP  $^{13}\text{C}$  pyruvate with Cartesian  $k$ -space trajectories [99] and combined with an SNR-optimal single-arm spiral encoding [100].

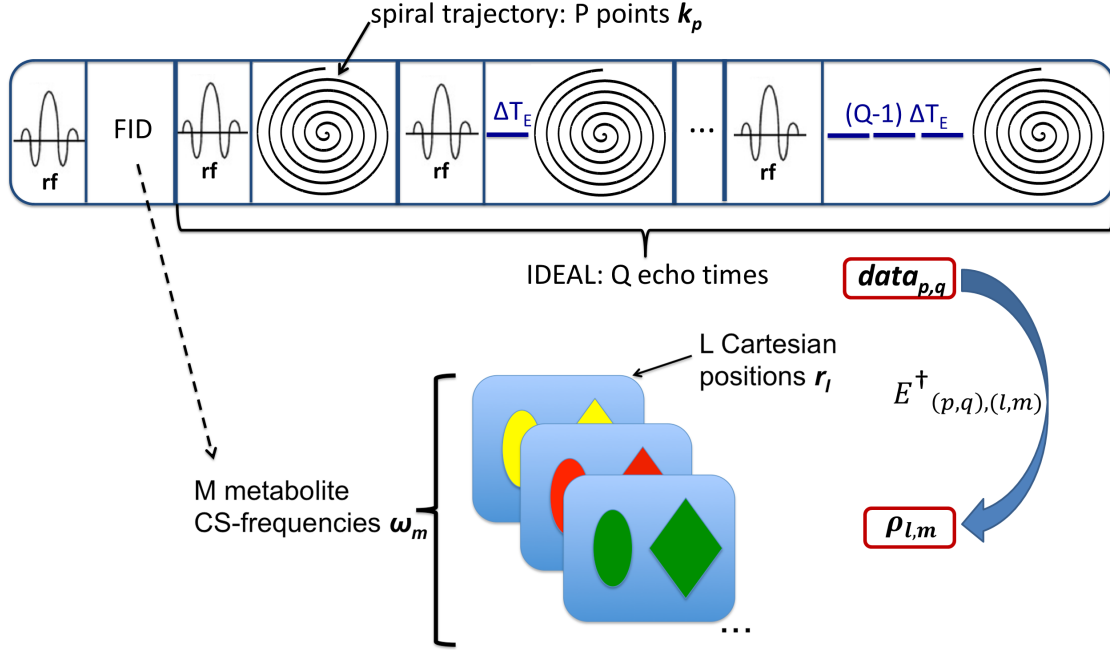


Figure 16: IDEAL spiral acquisition scheme: Spatial encoding with a spiral  $k$ -space trajectory is combined with  $Q$  equidistant IDEAL timesteps for encoding the spectral domain. For reconstruction, the spectral–spatial encoding matrix  $E_{(p,q),(l,m)}$  has to be inverted to calculate  $M$  metabolic maps. The metabolite frequencies  $\omega_m$  necessary to set up the encoding matrix can be measured with a FID before IDEAL spiral acquisition.

IDEAL CSI with the (spiral) trajectory  $k_p$  (length:  $P$ ) encodes the spin density  $\rho_{(m,l)}$  of  $M$  metabolites with the CS frequencies  $\omega_m$  at  $L$  (Cartesian) positions  $r_l$ . The IDEAL acquisition scheme uses  $Q$  different echo times, equidistantly shifted by an increment of  $\Delta T_E$ . The encoding times of each of the  $Q \cdot P$  signal points are given as  $t_{(p,q)} = t_p + (q - 1) \cdot \Delta T_E$ , where  $t_p$  describes the timing of the  $k$ -space

trajectory. The encoding of the spin density to the complex signal vector  $S_{(p,q)}$  can be formulated by the forward model, in which the encoding matrix  $E_{(p,q),(l,m)}$  (size:  $P \cdot Q \times L \cdot M$ ) is multiplied by the spin density vector (length:  $L \cdot M$ ):

$$S_{(p,q)} = E_{(p,q),(l,m)} \cdot \rho_{(l,m)} \quad (35)$$

with the known spectral-spatial encoding matrix

$$E_{(p,q),(l,m)} = e^{ik_p r_l} \cdot e^{i\omega_m t_{(p,q)}} = e^{ik_p r_l} \cdot e^{i\omega_m t_p} \cdot e^{i\omega_m t_q} \quad (36)$$

The first term describes the spatial ( $k$ -space) encoding  $F_{p,l} = e^{ik_p r_l}$ , the second term is a modulation of the signal stemming from metabolite  $m$  with the frequency  $\omega_m$ , and the third is the spectral (IDEAL) encoding  $G_{m,q} = e^{i\omega_m t_q}$ . These terms are independent of each other, so the inverse problem can be solved separately, leading to smaller matrices and hence shorter reconstruction times. To reconstruct the data, the inverse problem has to be solved:

$$\rho_{(l,m)} = E_{(p,q),(l,m)}^\dagger \cdot S_{(p,q)} \quad (37)$$

The calculation of the inverse encoding matrix can be split into three steps:

- IDEAL decoding of the  $k$ -space data:  $\mathbf{G}_{(m,q)}^\dagger \cdot S_{(p,q)}$
- Demodulation of the data:  $e^{-i\omega_m t_p} \mathbf{G}_{(m,q)}^\dagger \cdot S_{(p,q)}$
- Spatial reconstruction:  $\rho_{l,m} = \mathbf{F}_{p,l}^\dagger \cdot e^{-i\omega_m t_p} \mathbf{G}_{(m,q)}^\dagger \cdot S_{(p,q)}$

This separate reconstruction scheme is possible as long as the spatial and the spectral reconstruction are independent. This no longer holds true, if a spatial varying external field is taken into account for a correction of  $B_0$ -inhomogenities [101]. However, this was not applied in this work, since the field inside a clinical scanner is relatively homogeneous inside small animals like rats.

IDEAL decoding can cause noise amplification if the echo time spacing  $\Delta T_E$  is not chosen appropriately, leading to poor conditioning of the matrix  $G_{(m,q)}$ . The metric that is used to quantify this is the effective number of signal averages (NSA) [99] [95]:

$$NSA_q = \frac{1}{(G^H G)_{q,q}^{-1}} \quad (38)$$

where  $H$  denotes the complex conjugate transpose. To optimize the echo time  $\Delta T_E$  for a set of frequencies  $\omega_m$ , this number can be maximized numerically, which causes minimal noise amplification.

Spatial reconstruction can be performed either by numerical inversion of the spectral encoding matrix  $F_{(p,l)}$ , or by a combination of a gridding algorithm and the fast Fourier transform [39], which is less time consuming.



## 4 Experimental Setup

### 4.1 Hardware

The studies presented in this work were performed at different laboratories with different combinations of hardware components in the setup. Therefore, this section provides a short overview of the devices used. The development of the acetate imaging framework described in chapters 5.1 and 5.2 and the rat study presented in chapter 5.3 were performed in the lab of *GE Global Research* in Munich, Germany. A follow-up study using the developed methods to investigate acetate metabolism in diabetic rats (chapter 5.4) was conducted at the MR Research Centre of the Department of Clinical Medicine at Aarhus University in Denmark. A 3D multi-band imaging sequence for the investigation of cardiac metabolism of HP pyruvate in pigs (presented in chapter 6) was implemented at the *Fondazione CNR Regione Toscana* in Pisa, Italy.

#### MR Scanner

The three labs were equipped with the same scanner model, a GE HDx 3T Scanner (*GE Healthcare*, Milwaukee, WI, US). This is a clinical whole-body scanner with a bore diameter of 60 cm. Its gradient system can generate a maximum gradient amplitude of 40 mT/m in all three spatial dimensions. The maximum slew rate, which describes the maximum time derivative of the gradient, is 150 T/m/s in each direction.

#### DNP Polarizer

Two different types of DNP polarizer were used. In Munich and Pisa, a 3.35 T HyperSense DNP polarizer (*Oxford Instruments*, Abington, UK) (see Figure 17a) was available. In Aarhus, a 5 T SPINlab polarizer (*GE Healthcare*, Broendby, Denmark) was operated (see Figure 17b).

The basic configuration of both polarizers is the same: Each consists of a superconducting magnet (3.35 T or 5.00 T) cooled by liquid helium and nitrogen, a solid-state microwave source operating at the electron resonance frequency (about 94.14 GHz) for  $e^- - {}^{13}\text{C}$  polarization transfer (chapter 2.3.1), and a variable temperature insert (VTI). During polarization, the sample is kept in the VTI, which is connected to the surrounding liquid helium reservoir. The inflow of helium, in combination with a reduction in the pressure inside the VTI by an electrical vacuum pump, allows the temperature to be reduced to  $\sim 1.3$  K. This low temperature is essential for polarization, as the thermal equilibrium of the  ${}^{13}\text{C}$  polarization described by the Boltzmann distribution depends strongly on the temperature [see Figure 8 and eq. (27)]. After the solid  ${}^{13}\text{C}$  sample is polarized, it is rapidly dissolved into a hot (100°C) pressurized (10 bar) aqueous dissolution agent. This

solves the solid sample completely and flushes it out through a hose into a glass container, where it can then be withdrawn with a syringe and injected into the animal. The minimum time from the beginning of dissolution until the start of substrate injection is about 12 to 15 s.

The SPINlab can be seen as a development of the HyperSense polarizer. In addition to the higher magnetic field, it has the advantage of having four polarization chambers, so it is not necessary to wait after one polarization for the polarization of the next sample (about an hour). The waiting time between two injections can thus be reduced to about 15 min, which is needed for a cleaning procedure and loading the new dissolution agent.

Both polarizers are equipped with a  $^{13}\text{C}$  spectrometer, which is used to monitor the polarization buildup. This information is essential for optimizing the recipe of newly introduced HP substances.

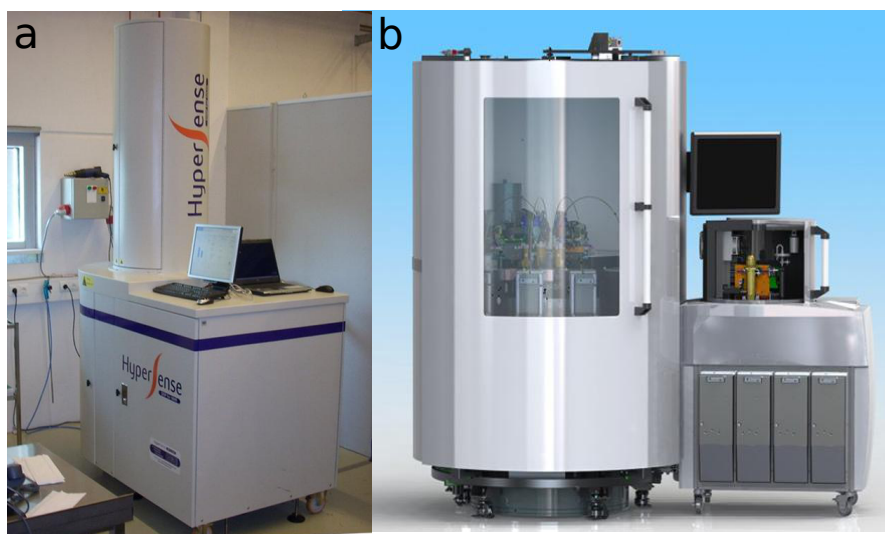


Figure 17: The two DNP polarizer models used in this work: 3.35 T HyperSense Polarizer (a) and 5 T GE SPINlab (b).

### RF Coils

RF excitation and signal detection for the rat experiments were realized using the same coil type in Munich and Aarhus, a double-tuned  $^1\text{H}$ - $^{13}\text{C}$  volume coil [102] adapted to the size of rats (inner diameter of 8.0 cm), which provides a high filling factor and thus good SNR properties. It consists of a saddle-shaped coil for  $^{13}\text{C}$  and a birdcage coil for  $^1\text{H}$  signaling, both operated in quadrature mode. The setup with a rat lying inside the coil on a rat bed, constructed by *Rapid Biomedical* (Rimpar, Germany) is shown in Figure 18a.

For the pig experiments, a combination of two RF coils for transmission and reception was used. Transmission was performed on a single-tuned quadrature

$^{13}\text{C}$  birdcage coil (*Rapid Biomedical*) with an inner diameter of 35 cm. The signal was received with a 16-channel phase array coil (*Rapid Biomedical*) [103]. Proton images for location and reference scans were acquired with the product's body coil integrated into the MR scanner. The coil setup for pigs is illustrated in Figure 18b.

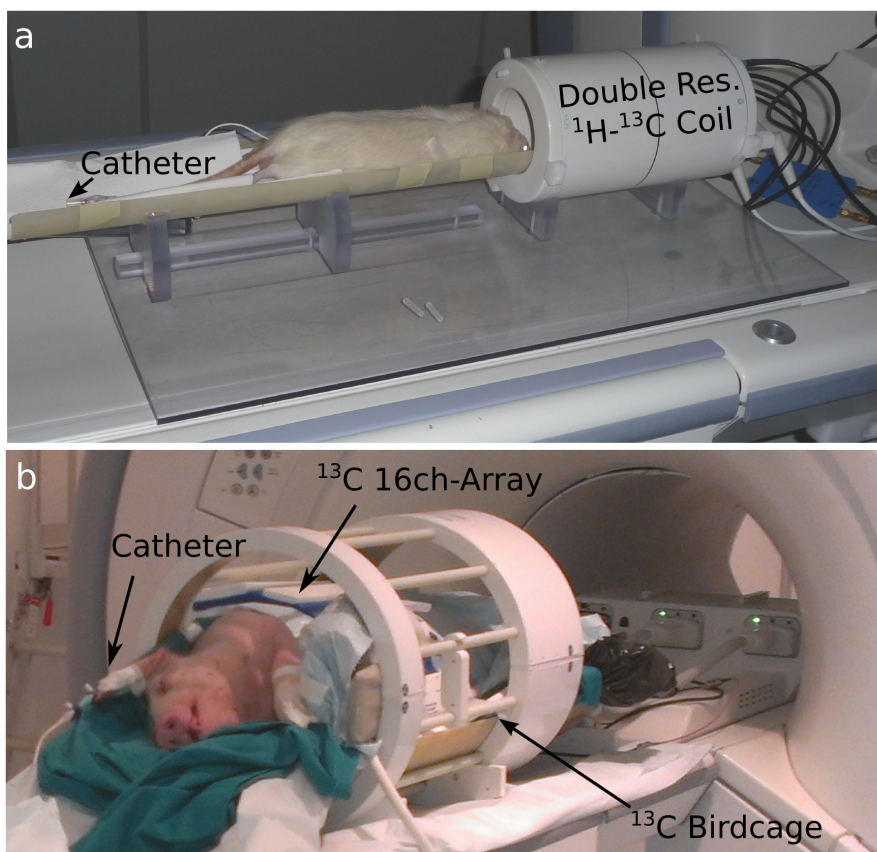


Figure 18: a: Rat setup with the double-resonant  $^{13}\text{C}$ - $^1\text{H}$  coil outside of the scanner.  
b: For the pig setup, a birdcage coil for transmission was combined with a 16-channel receive array.

### Other Hardware

A Bruker Minispec 1 T tabletop spectrometer (*Bruker*, Karlsruhe, Germany) was available in Munich and Pisa. This was used for in vitro quantification of the relaxation times and polarization levels of the HP probes. These parameters are very important during recipe optimization (chapter 4.2) as well as during animal studies for quality control of the HP substrate.

### Computational

The implementation of the waveforms and all simulations and reconstructions were performed in MATLAB (*Math Works, Inc.*). All software was run on a MacBook Pro with 8 GB of RAM and a 2.7 GHz Intel Core i7 processor. Timescales stated in this work to characterize the performance of programs and algorithms are given for this setup.

## 4.2 Preparation of [1- $^{13}\text{C}$ ]Acetate for DNP

The first step in establishing an HP  $^{13}\text{C}$  substance for preclinical in vivo experiments is to find an optimized recipe of the probe for hyperpolarization. This should be optimized with regard to a maximal tracer concentration in the sample, the final polarization level, and the time it takes to reach this level. The recipe for a DNP sample consists of four basic ingredients: The molecule to be polarized, a glassing agent that dissolves the molecule at a high concentration, the radical providing electrons for DNP transfer, and finally a low dose of a relaxation agent, which increases with its optimal concentration the speed of the polarization process as well as the final polarization level. The underlying physical effect of this benefit is the rapid relaxation of the electron spin ensemble to thermal equilibrium (polarization of almost 1), so that the electron polarization can be transferred more rapidly to the  $^{13}\text{C}$ -nuclei.

Trityl OXO63 (*Oxford Instruments*, Abingdon, UK) was used as the radical. For electron relaxation, gadoteric acid (Dotarem, *Guerbet*, Villepinte, France), which contains a gadolinium atom and is a relaxation agent widely used for clinical MR experiments, was mixed into the sample.

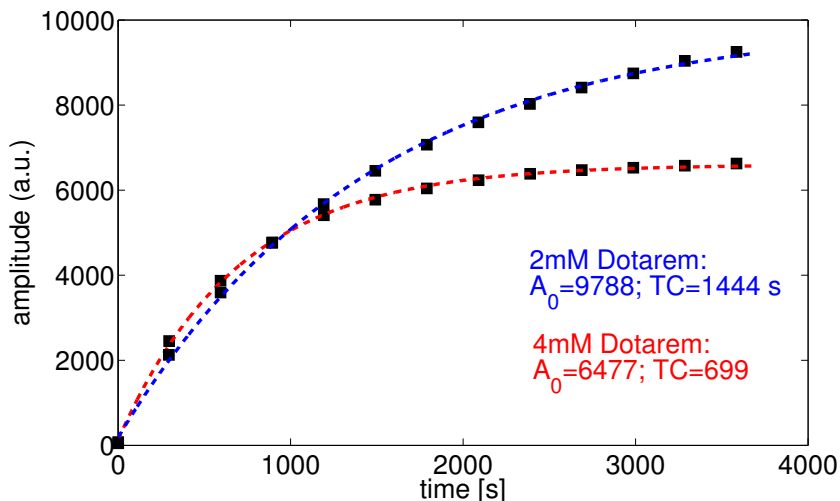


Figure 19: Build-up and fitting curves of acetate samples with different Dotarem concentrations (other parameters kept the same). For the final formulation, the amplitude should be as large as possible to obtain a high polarization level. However, the build-up time constant  $TC$  has to be reasonably short to avoid long waiting times during in vivo studies.

The concentrations of the chemicals (and their effects) have to be well balanced, which leads to a trade-off between the solid-state polarization level and polarization

speed. The build-up curve gives the relationship between the time  $t$  and the measured signal amplitude  $A$  during polarization. The polarization speed and level can be estimated phenomenologically by fitting the build-up data to the model:

$$A(t) = A_0(1 - \exp(\frac{-t}{TC})) \quad (39)$$

$A_0$  is the final amplitude, representing the solid-state polarization (for a fixed amount of tracer), and the time constant  $TC$  gives the time needed to develop  $1 - \exp(-1) \approx 63\%$  of the polarization. As an example, two build-up curves acquired for the examination of different Dotarem concentrations with the same concentration of acetate and OXO63 are shown in Figure 19.

The  $[1-^{13}\text{C}]$ acetate probes were prepared beginning with  $[1-^{13}\text{C}]$ acetate sodium salt, which was dissolved at the maximal solubility (4.5 M) in glycerol. Then, the probe was mixed in a ultrasonic bath for about 2 h at  $70^\circ\text{C}$ . When cooled inside the polarizer, glycerol forms a glassy probe with the dissolved salt, which would not be the case for water. The optimal Dotarem and OXO63 concentrations were found to be 30 mM for OXO63 and 1.6 mM for Dotarem. This mixture was polarized in a 3.35 T HyperSense DNP polarizer for 75 min.

A dissolution agent has to be prepared so that the solution can finally be injected into the animal. Therefore, a physiological pH and osmolarity must be guaranteed. The solution used here contained 5 mM phosphate-buffered saline (PBS) buffer in  $\text{D}_2\text{O}$ , resulting in a 120 mM acetate solution.  $\text{D}_2\text{O}$  instead of water increases the relaxation time compared to water, since the  $^{13}\text{C}$  nucleus experiences less dipolar coupling. Of course, this holds true only until the substrate is injected and is in contact with the animal's blood.

The relaxation behavior of the HP solution can be evaluated using a 1 T tabletop spectrometer by fitting a time series of flip-angle-corrected [according to eq. (30)] intensities to a monoexponential decay curve (see Figure 20). Furthermore, a comparison of the signal intensity measured in the polarized probe  $I_h$  with the intensity of the same probe in thermal equilibrium  $I_{th}$  provides the information needed to calculate the polarization level. The measured thermal intensity is therefore related to the known thermal polarization level  $P_{th}$  in eq. (27) depending on the probe's temperature and the field  $B_0$ . The polarization measured at  $\Delta T$  after dissolution is then

$$P_{hyp}(\Delta T) = \frac{I_h}{I_{th}} \cdot P_{th} \quad (40)$$

By using the measured time  $T_1$ , this can be backprojected to the time of dissolution:

$$P_{hyp}(0) = P_{hyp}(\Delta T) \exp(\frac{\Delta T}{T_1}) \quad (41)$$

The average liquid-state polarization level during the animal experiments ( $n = 25$ ) was  $22.3 \pm 5.2\%$ , and the relaxation time in the solution was  $T_1 = 71.8 \pm 3.2$  s. With these values, the polarization level at the start of the injection ( $15 \pm 2$  s after the dissolution) is stated to  $18.1 \pm 4.3\%$ , calculated with propagation of error. Note, that this calculation can only consider the  $T_1$ -time measured at 1 T, which might be slightly different during the transportation to the scanner, so that this analysis should serve as an estimation only. However, this polarization level is significantly higher than the value previously reported in [28] where a DNP polarization level of  $13 \pm 2$  ahead of injection was measured for sodium[1- $^{13}\text{C}$ ]acetate solved in a 1:2 mixture of  $\text{d}_6\text{-EtOD}/\text{D}_2\text{O}$ .

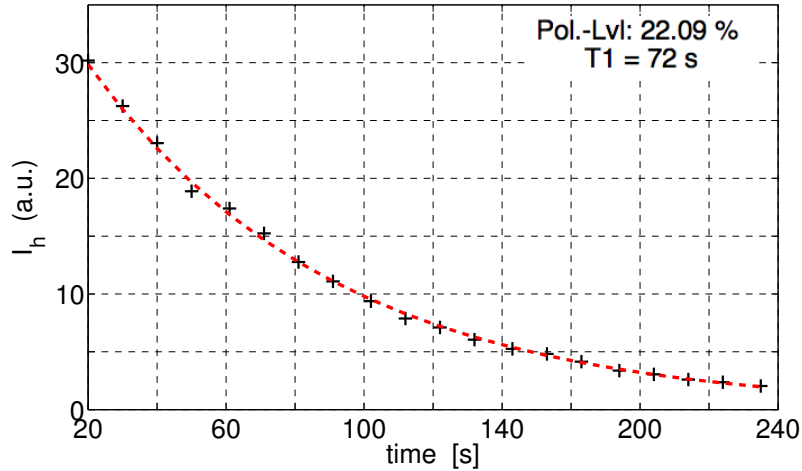


Figure 20: The  $T_1$  decay can be calculated via a monoexponential fit of the intensities. The liquid-state polarization after dissolution can be calculated using  $T_1$  and an additional measurement of the thermal signal from the same probe.

The optimized recipe was used for the HP acetate measurements performed with the HyperSense polarizer in the acetate CSI development presented in chapters 5.1 and 5.2 and for the rat study presented in chapter 5.3. For the acetate experiments in Aarhus (chapter 5.4), a previously published procedure [104] for polarization in the 5 T SPINlab was applied. The major difference from the recipe described above is that a water/glycerol combination is proposed as the glassy agent. This makes a higher final acetate concentration possible but has the drawback of a lower polarization level.



## 5 Experiments with Hyperpolarized [1-<sup>13</sup>C]Acetate

In this chapter the development and results of all in vivo experiments with HP [1-<sup>13</sup>C]acetate are presented. This includes the design of a SPSP pulse for selective excitations of acetate (chapter 5.1) and its metabolite ALCAR and the development of an IDEAL spiral CSI sequence (chapter 5.2). This techniques were firstly tested in vivo and afterwards applied for two studies. The first study investigates the effect of stress and following increased cardiac workload on the acetate metabolism, induced with the catecholamine dobutamine (chapter 5.3). The methods and results presented in the chapters 5.1 to chapter 5.3 were previously published as a full paper in *Magnetic Resonance in Medicine (MRM)* [53] and presented with a talk at the 22<sup>nd</sup> *ISMRM* conference 2014 [105]. Finally, the second study investigates the effect of STZ-induced diabetes and the inherent hyperglycemia on the ALCAR/acetate ratio in chapter 5.4.

### 5.1 Spectrospatial Pulse for Alternating Acetate and Acetylcarnitine Excitation

#### 5.1.1 Purpose of the SPSP Pulse

The first tests of the acetate study were run with a slice-selective so-called soft pulse. They showed that it is challenging to gather information from this metabolic system: The peak of one metabolic product, which was recognized as ALCAR, was visible in spectra acquired over the heart and kidneys, yet with a low SNR. The aim was to develop a sequence capable of acquiring localized information, which means obtaining maps of ALCAR. Since this sequence had to be designed as SNR-optimal for acquisition of ALCAR, an SPSP pulse was implemented to optimally exploit the magnetization during acquisition (see chapter 3.3). Designed to explore a potential imaging approach, this pulse furthermore enables the acquisition of quantifiable time-resolved spectra.

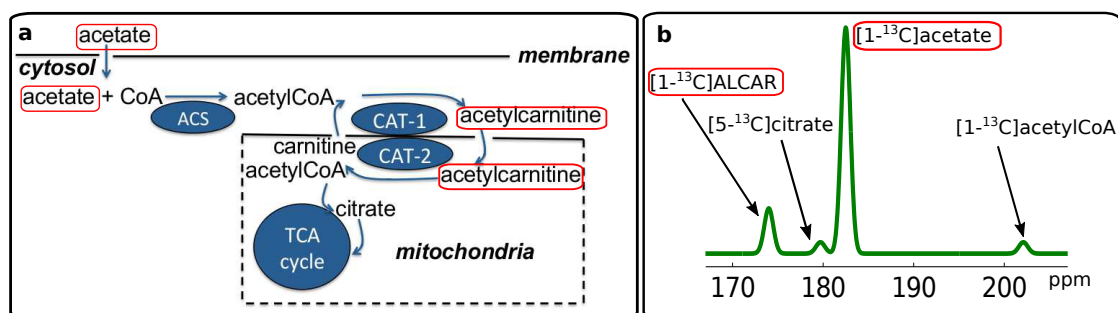


Figure 21: a: Acetate is present outside the cell and inside the cytosol; ALCAR shuttles AcCoA into the mitochondria. b: Schematic spectrum shows the chemical shifts of the metabolic products of  $[1-^{13}\text{C}]$ acetate.

Figure 21a shows an overview of the acetate metabolism and the related frequencies of interest after  $[1-^{13}\text{C}]$ acetate injection. During the intermediate metabolic steps, the  $^{13}\text{C}$  label remains in the 1 position; the relevant chemical shifts are 182.5 ppm for  $[1-^{13}\text{C}]$ acetate, 174.0 ppm for  $[1-^{13}\text{C}]$ ALCAR, and 202.1 ppm for  $[1-^{13}\text{C}]$ AcCoA [30]. After  $[1-^{13}\text{C}]$ AcCoA enters the TCA cycle via citrate synthase, the label is transferred to  $[5-^{13}\text{C}]$ citrate, which has a chemical shift of 179.7 ppm [106]. Because the difference between the chemical shifts of  $[5-^{13}\text{C}]$ citrate and  $[1-^{13}\text{C}]$ acetate signal is relatively small (about 90 Hz at 3 T), the citrate signal can hardly be quantified, as it overlaps with the large peak of the administered substrate. Furthermore, the free AcCoA pool in the cell is much smaller than the ALCAR pool. Therefore, focus was placed on the ALCAR signal in addition to the substrate signal in order to quantify acetate activation.

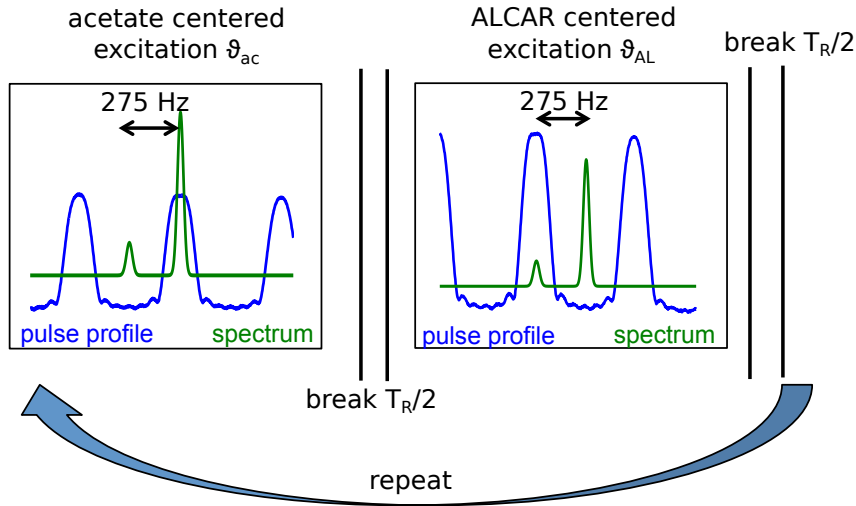


Figure 22: Alternating acquisition scheme: The two species are acquired separately, and the acetate signal is acquired with a lower flip angle than the ALCAR signal ( $\vartheta_{ac} < \vartheta_{AL}$ ).

The ALCAR signal is about one to two orders of magnitude lower than the acetate signal, which strongly limits the SNR of ALCAR and makes quantification of this metabolic pathway challenging. To address this problem and optimize the ALCAR SNR, an SPSP pulse was designed to selectively excite one of the two target frequencies, which differ by 275 Hz at 3 T. As described in chapter 2.3, excitation by a flip angle  $\vartheta$  causes the HP magnetization to decay by a factor of  $\cos(\vartheta)$ . To maintain magnetization, the SPSP pulse facilitates acetate excitation at a lower flip angle than ALCAR (Figure 22). The SPSP pulse additionally improves separation of the ALCAR signal from the dominant acetate signal even shortly after substrate administration (Figure 36).

### 5.1.2 Pulse Design

The pulse (see Figure 23) was designed by direct matrix inversion as described in chapter 3.3. A flyback design was chosen for the gradient waveform because of its high robustness against gradient errors. The pulse is composed of eight sublobes each lasting 1.82 ms, for a total pulse duration of 15.5 ms. The time reference of the RF pulse amplitude is shifted toward the end of the pulse, which reduces the relaxation losses as well as the flow and motion artifacts. The resulting isodelay of the pulse,  $t_{iso} = 5.5$  ms, leads to an acceptable signal loss due to  $T_2^*$  decay of  $d = 1 - \exp(-t_{iso}/T_2^*) \approx 13\%$ , with an assumed  $T_2^* = 1/(\pi \cdot 15\text{Hz}) = 21.2\text{ms}$ . As a drawback, the low number of sublobes degrades the spectral profile and causes residual acetate excitation during ALCAR acquisition.

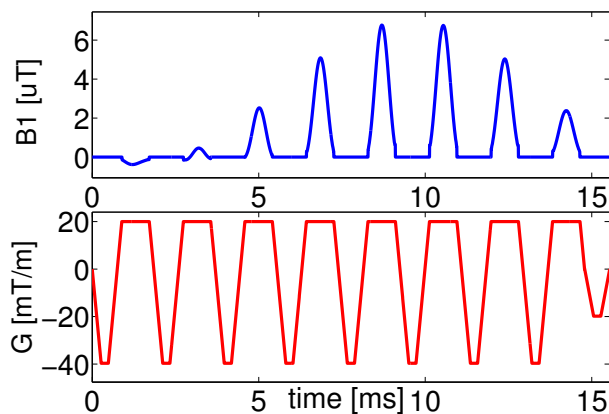


Figure 23: SPSP excitation pulse with modulation of the RF (blue) amplitude and  $z$  gradient (red) alternating in flyback mode.

### Phantom Tests

To characterize the pulse performance – in particular, the residual excitation of the acetate signal during ALCAR excitation – a spectral–spatial pulse profile was acquired. The profile was measured on the proton (water) frequency with a thin NMR tube filled with water and doped with 4% Dotarem. The test tube was aligned along the  $z$  direction during acquisition and slice excitation as well as a readout gradient was set along the  $z$  direction. The scanner excitation frequencies were swept in 4 Hz steps from  $-750$  to  $750$  Hz. For each frequency, a 1D dataset spatially encoded along  $z$  was acquired with a  $90^\circ$  flip angle and a repetition time of  $T_R = 1.0$  s. For each frequency, the 1D data were reconstructed along the  $z$  axis, yielding a directly measured 2D profile. This profile finally was interpolated by a factor of two in both dimensions and is depicted in Figure 24a. In the spectral domain (Figure 24b), the stopband, indicated by the red line, is below 5% of the intensity of the  $90^\circ$  pulse. Since the intensity is proportional to the sine of the flip angle  $\sin(\vartheta)$ , a residual flip angle of about  $3^\circ$  can be estimated. In the spatial domain (Figure 24c), where false excitation would lead to signal folding in the spectra or images from other slices, the excitation outside the transition band is very low (about 3% for the first sidelobe).

In conclusion, the pulse shows a well-defined profile in both the spectral and spatial dimensions and thus is an adequate compromise between profile degradation and pulse duration.

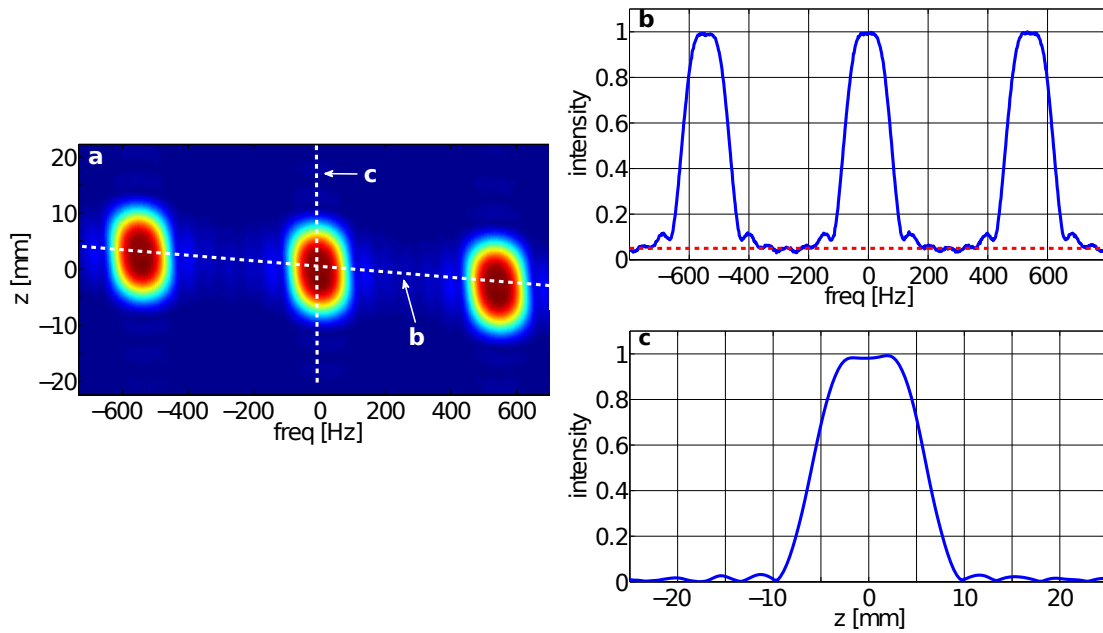


Figure 24: a: Spectral-spatial profile of the pulse. Excitation intensities in the spectral dimension (b) and spatial dimension (c) along the dotted lines in (a).

### 5.1.3 In Vivo Spectroscopy

The pulse was tested in vivo in a healthy male Lewis rat (animal prepared as described in chapter 5.3) with a repetition time of 3 s for each metabolite and flip angles of  $4^\circ$  for acetate and  $15^\circ$  for ALCAR. Three slices with a thickness of 12 mm were acquired, covering the heart, liver, and kidneys. As an example, the resulting absolute spectra after acetate and ALCAR excitation acquired in the heart slice and filtered with a 15 Hz Gaussian filter are shown in Figure 25. The acetate signal contains very huge intensities at the beginning as the substrate bolus arrives in the heart via venous blood. The ALCAR spectra show high intensities of acetate dominating the spectra during bolus arrival. This is explained by residual excitation of acetate, which arises from a combination of pulse imperfection and the huge concentration difference of the two substances. The SNR of the ALCAR peak is relatively low; however, the amplitude values can be separated from those of the acetate peak and quantified. The time development of the amplitudes of the acetate signals after acetate excitation and the ALCAR signals after ALCAR excitation are illustrated in Figure 26. The acetate signal accumulating in the kidney slice is higher than that in the other organs. This result is not surprising if the relatively large volume of both kidneys in this slice and the exceptional perfusion of this organ is considered. Additionally, the highest ALCAR signal

values could be detected in the kidneys; however, the relative ALCAR/acetate ratio is clearly highest in the heart slice, indicating the highest conversion rate in the cardiac region, which agrees with the expectations described in chapter 3.1. The maximal ALCAR signal can be observed about 15 s after the arrival of the bolus in both organs. The conversion of acetate to ALCAR inside the liver, unlike that in the heart and kidneys, is relatively low, and the measured ALCAR intensities are not much above the noise level.

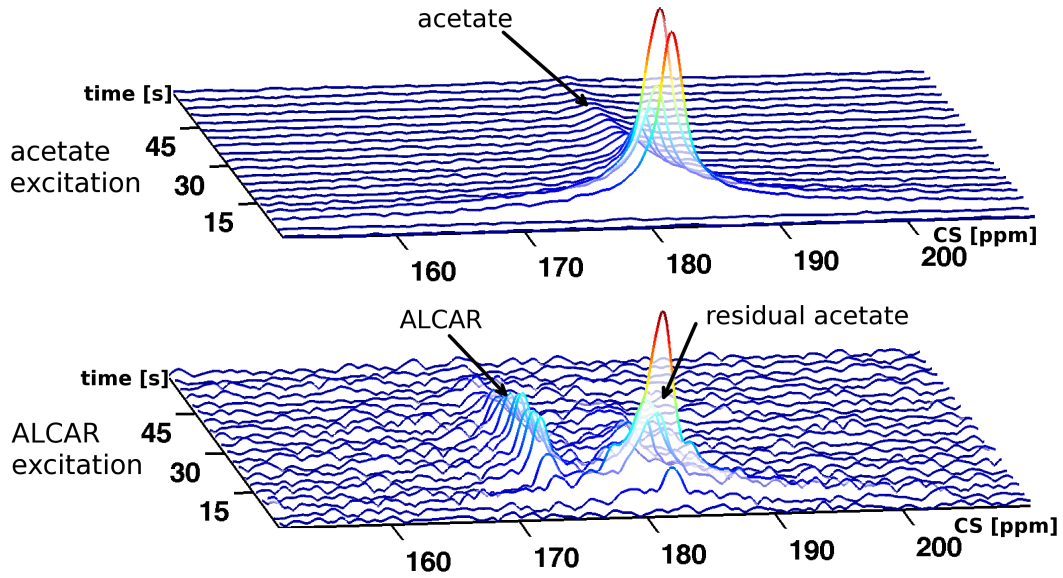


Figure 25: Absolute spectra acquired in rat heart in vivo after excitation centered on the acetate frequency (top) (4°) and on the ALCAR frequency (bottom) (15°).

The residual excitation of acetate is analyzed in Figure 27. After the excitations soon after the injection (<10 s after substrate administration), the residual acetate signal dominates; however, the ALCAR signal gradually increases over time. This finding demonstrates that the spectral separation by the pulse is not adequate for image acquisition during or immediately after bolus arrival after substrate injection with a single-shot technique. Therefore, it is necessary to also apply a CSI technique such as IDEAL additionally to the SPSP pulse.

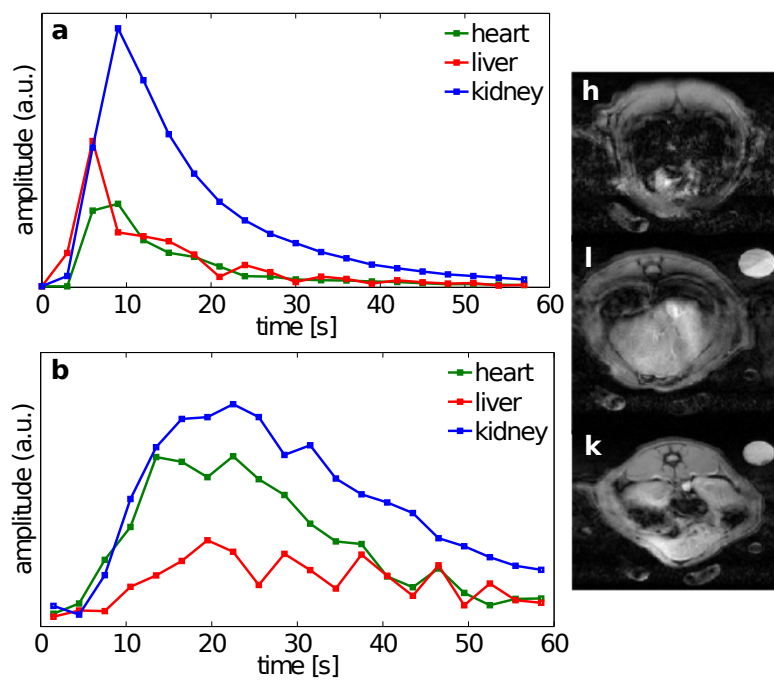


Figure 26: Signal development over time of the acetate (a) and ALCAR (b) intensities for three slices covering heart, liver, and kidneys.

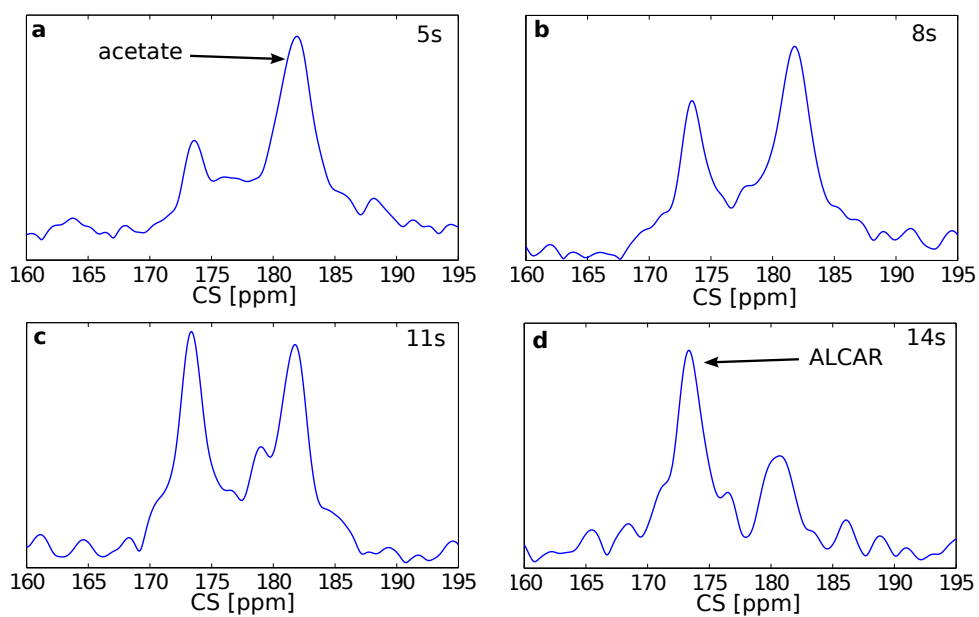


Figure 27: Absolute spectra acquired at the ALCAR frequency at different times after HP acetate injection. Residual acetate dominates the spectra shortly after injection. However, both signals are separable for quantification at all timepoints.

## 5.2 Metabolic Imaging of Hyperpolarized Acetate and Acetylcarnitine

### 5.2.1 Spiral $k$ -Space Trajectories

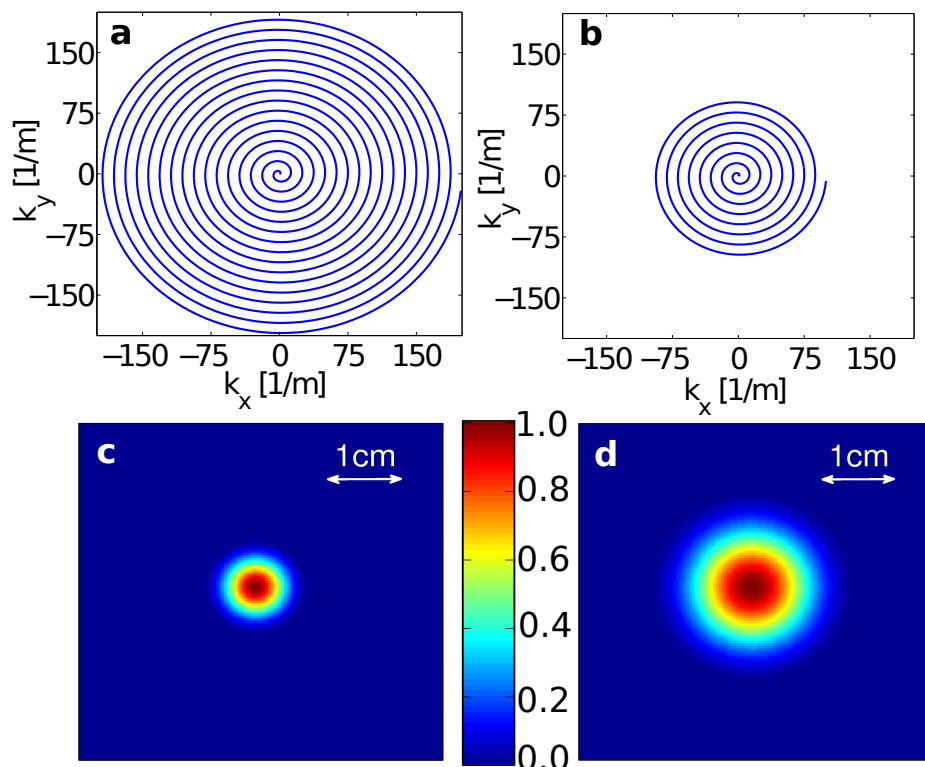


Figure 28: The two  $k$ -space trajectories and their point spread functions (maximum set to 1.0). a and c: Higher-resolution trajectory with a real resolution of 5 mm; b and d: lower-resolution trajectory with a real resolution of 10 mm.

Single-arm spiral trajectories were used for encoding the two spatial dimensions after excitation with the SPSP pulse. An acetate map can be obtained without additional spectral encoding when the pulse is centered on the acetate frequency, as the residual ALCAR excitation is negligible because of the low concentration (see Figure 25). For the acetate map, a flip angle of  $\vartheta_{Ac} = 15^\circ$  was chosen. To account for the huge signal difference, the two molecules were acquired with two different trajectories. Each was designed for a field of view (FOV) of 8.0 cm and a 45 ms total readout time; the trajectories are shown in Figure 28a/b. The trajectory for acetate imaging (Figure 28a) had a real resolution of  $5 \times 5 \text{ mm}^2$  [107], and

the second one (Figure 28b), with a lower real resolution of  $10 \times 10 \text{ mm}^2$ , was used for time-resolved ALCAR imaging, where the SNR is too low for the higher resolution. The  $T_2^*$  decay and relatively long trajectory cause the outer  $k$ -space frequencies to be noisy. This was accommodated by applying a Gaussian filter to the  $k$ -space data with an assumed  $T_2^*$  of 21 ms. The point spread functions (PSFs) of both trajectories are shown in Figure 28c/d, where both the signal decay and the filter are accounted for during the reconstruction process. Owing to the filter and the relatively low resolution (compared to the proton trajectories) the jinc sublobes characteristic of a spiral PSF are nearly degraded. The spiral data were reconstructed by direct inversion of the spatial encoding matrix  $\mathbf{F}_{p,l}^\dagger$  (see chapter 3.4.2) onto a circular  $64 \times 64$  Cartesian grid. Therefore, the Moore–Penrose pseudoinverse of  $\mathbf{F}_{p,l}^\dagger$  was computed via regularized singular value decomposition. The matrix inversion takes about 180 s on the described computational setup; however, it has to be performed only once for each trajectory, the result can be saved and for following reconstructions the inverted matrix can be loaded. Finally, the images were interpolated by a factor of two in both dimensions.

## 5.2.2 Single-Timestep IDEAL Spiral CSI

### Imaging Sequence

To demonstrate the feasibility of imaging in the rat heart, maps for acetate and ALCAR were firstly acquired at a single time point. Therefore, the timeslot with the highest ALCAR signal during the previously acquired spectra, which was about 15 s after injection, was chosen as the start time (Figure 36). The residual acetate excitation after an ALCAR-centered pulse, especially shortly after acetate injection (Figure 27), would distort the ALCAR images. To prevent this artifact pollution, the SPSP pulse was combined with three-step ( $Q = 3$ ) IDEAL encoding (Figure 30) for the ALCAR acquisition in order to encode the two frequencies ( $M = 2$ ). Overdetermination ( $Q > M$ ) ensures robustness in the spectral domain and thus decreases pollution due to misattribution between the two frequencies. Figure 29 shows the NSA (see chapter 3.4.2) for three echoes calculated for different echo time shifts  $\Delta T_E$ , considering a spectral linewidth of 20 Hz for both metabolites. The optimal echo time spacing was found to be  $\Delta T_E = 1.20 \text{ ms}$ . This ensured that no SNR was lost despite the  $T_2^*$  decay during the echo time (maximum of 2.40 ms). Note that the NSA curve is the same for both molecules, since there are only  $M = 2$  frequencies and therefore only a single frequency difference.

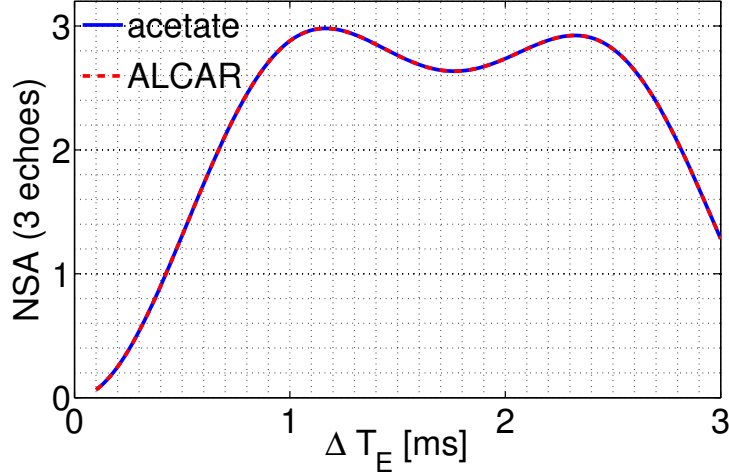


Figure 29: Number of signal averages (NSA) for the frequencies of acetate and ALCAR ( $\Delta f = 275$  Hz) with three IDEAL encoding steps.

The last flip angle for ALCAR acquisition was set at  $90^\circ$  to use the entire magnetization at the chosen time point (see Figure 30). The other two flip angles were chosen to provide an identical signal intensity after each excitation [108]:

$$\vartheta_n^{const} = \cos^{-1} \left( \sqrt{\frac{1 - e^{2(n_{tot}-n)(\frac{-T_R}{T_1})}}{1 - e^{2(n_{tot}-n+1)(\frac{-T_R}{T_1})}}} \right) \quad (42)$$

where  $T_R$  denotes the repetition time (500 ms), and  $n_{tot}$  is the number of echo timesteps (here  $n_{tot} = 3$ ). With an estimated  $T_1$  of 20 s, the result is that the  $n^{\text{th}}$  flip angle  $\vartheta_n^{equal} = (33^\circ, 44^\circ, 90^\circ)$ . Note that  $T_1$  plays a negligible role in the flip angle calculation because the repetition time  $T_R$  is much shorter than  $T_1$ . The sequence was triggered on the respiration of the rat, and the respiratory rate was controlled to approximately  $60 \text{ min}^{-1}$  by adjusting the administered isoflurane. Two excitations were acquired during each gating cycle, so the total acquisition time was approximately 2 s. As only one ALCAR image is acquired, this technique is called "single-shot" in this work.

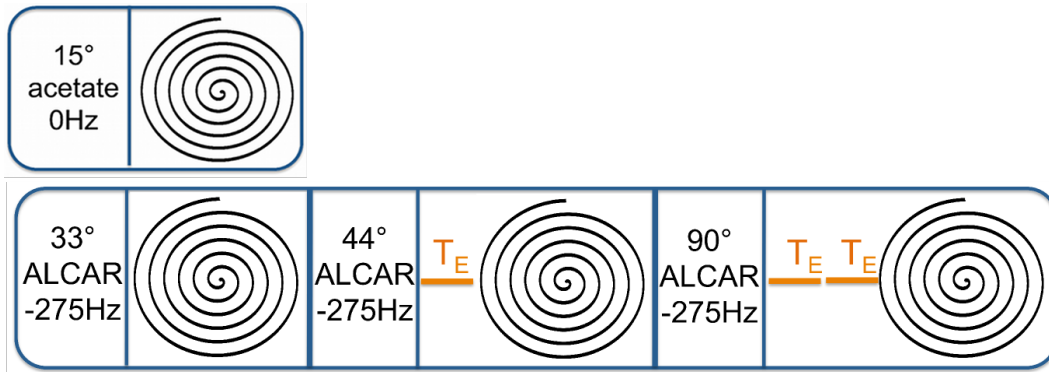


Figure 30: Imaging sequence: The acetate map is acquired with a single shot, whereas IDEAL encoding prevents pollution of the ALCAR map stemming from residual acetate excitation.

### In Vivo Results

To test the imaging sequence, in vivo tests on two healthy Fisher rats were performed. They were prepared and monitored during the MR session as described in chapter 5.3. In this work, all the images were acquired in a slice containing the heart, where the conversion is expected to be highest and which has huge potential for metabolic studies to detect changes in various pathologies (see chapter 3.1). Two imaging sequence setups were tested; once the acetate and ALCAR map were acquired with the same resolution in one rat, ALCAR was acquired in the other rat with the low-resolution spiral described above (see the trajectories in Figure 28). The results for both tests are shown in Figure 31.

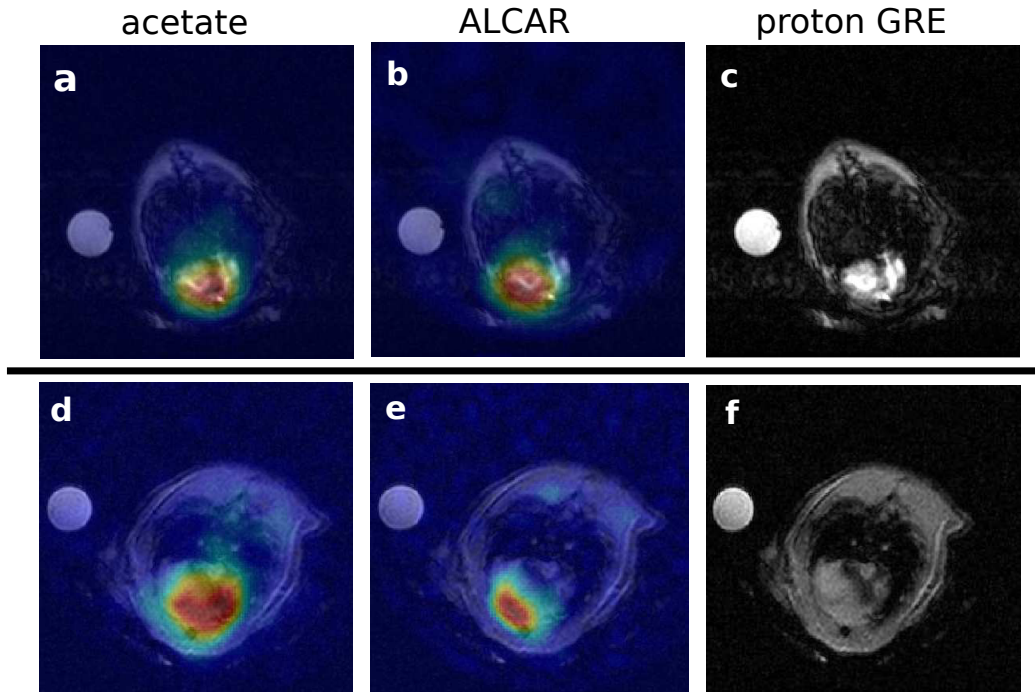


Figure 31: In vivo images acquired in heart slices of two different rats. In the upper row, the ALCAR image (b) was acquired with a lower resolution than the acetate image (a). In the lower row, both maps (d and e) have the same resolution. Additionally, the  $^1\text{H}$  gradient echoes are shown (c and f).

The images show that the acetate and ALCAR signals arise mainly from the heart. As expected, acetate is distributed over the entire heart because the substrate is distributed within the blood after intravenous administration. The ALCAR signal appears primarily within the left ventricle, particularly the muscular area at the front of the ventricle, as one can see in the higher-resolution ALCAR image (Figure 31e). This confirms the initial expectation that acetate is taken up and metabolized by myocardial cells, especially in the left ventricle, where the energy demand is highest. Particularly in the lower-resolution images, the ALCAR signal is spread over the entire left cavity, although ALCAR is confined to the myocardial cells. The real resolution of  $10 \times 10 \text{ mm}^2$  does not allow the muscle and cavity area to be distinguished. However, the image quality is well suited to defining ROIs in order to quantify the conversion over the entire ventricle, which is essential for the imaging study performed in chapter 5.3. The IDEAL-encoded images of acetate after ALCAR excitation (data not shown) were dominated by noise. The SNR of the higher-resolution ALCAR images ( $5 \times 5 \text{ mm}^2$ ) is sufficient and thus can be recommended for imaging at a single timepoint.

### 5.2.3 Time-Resolved IDEAL Spiral CSI

A major advantage of HP  $^{13}\text{C}$  studies is that metabolic reactions can be assessed on a timescale of seconds. Increasing the temporal resolution reduces the SNR for each image because the polarization is consumed with every excitation. The acquisition timing involves a trade-off between the SNR of each image, which must be high enough to maintain data reliability, and the temporal resolution of the image series. If a saturation recovery sequence is used [89], as it was for the ALCAR images, the repetition time addresses this trade-off. A series of substrate (acetate) images can be acquired with a relatively low flip angle to preserve the magnetization. Since the substrate is acquired independently of the metabolite (ALCAR), it is practical to record the substrate series with a higher temporal resolution in order to obtain well-defined intensity curves. A  $T_R$  of 2 s and a flip angle of  $15^\circ$ , which result in depletion of approximately 3.4% of the acetate magnetization for each image, were chosen. For the ALCAR images, which were acquired with three subsequent IDEAL-encoded excitations, a repetition time of 6 s was selected (see Figure 32). This ensured that three acetate images were always acquired between two ALCAR images.

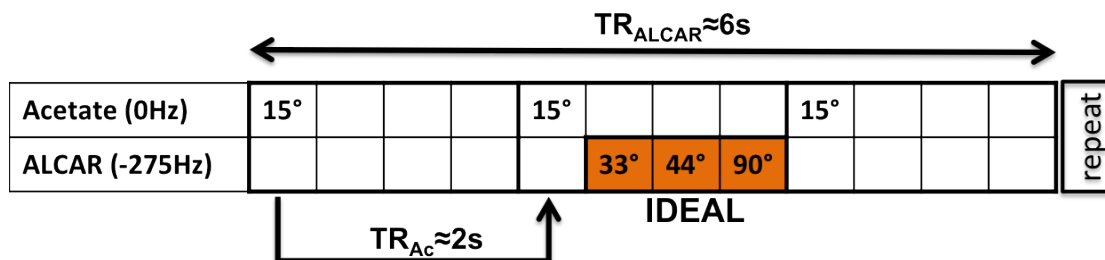


Figure 32: The time resolution of the acetate maps (single-shot spirals) was set three times higher than that for the IDEAL-spiral-encoded ALCAR maps (orange). The numbers in the table cells represent the flip angles of each excitation.

#### Signal Quantification and Calculation of the Apparent Conversion Rate

In magnitude MR images with low SNR, like those for the ALCAR maps here, the probability density function for the measured intensities deviates significantly from a Gaussian shape and is described by the Rice distribution [109]. That means that in a pixel with low SNR, the measured intensity values are biased on average toward higher intensities. In this work, this would cause overestimation of the intensity of low-SNR ALCAR maps at later timepoints. The acetate maps have a higher SNR; hence, they are not affected by this phenomenon. Therefore, unrealistically high apparent conversion rates would be measured at these timepoints [eq. (46)]. To address this problem, the unbiased intensity for each pixel can be estimated from the measured (biased) value with knowledge of the standard devia-

tion of the raw data from a maximum likelihood estimation, as described in [110]. To calculate the standard deviation, thermal noise images were acquired before each acetate injection. The described method is called Rice correction below. In spectroscopy, the SNR is usually higher, so the bias is low and has only a negligible effect on the correct quantification.

To quantify the time-resolved metabolic maps, ROIs were generated on the basis of the proton reference image. One ROI targeted the left ventricle of the heart in order to quantify the myocardial conversion. The images acquired for studying the effects of dobutamine-induced stress (presented in chapter 3.1) showed that, at least under stress, the ALCAR and acetate signals can also be localized in the muscular region of the back skeletal muscle. To investigate these effects, a second ROI was drawn around the back skeletal muscle.

The signal amplitudes within each ROI were pointwise Rice corrected and subsequently summed. For the quantitative analysis, an SNR threshold of 3 was designated as the relevant signal in the ROI. The metabolic conversion from acetate to ALCAR can be simplified using a two-site exchange model [28] [111]:

$$\frac{dM_{AL}}{dt} = k_{AcAL}M_{Ac} - \frac{1}{T_{1,AL}^*}M_{AL} \quad (43)$$

$M_{Ac}$  and  $M_{AL}$  are the acetate and ALCAR magnetizations, respectively, and  $T_{1,AL}^*$  is the effective ALCAR relaxation time. It includes the longitudinal relaxation  $T_{1,AL}$  as well as the decay of ALCAR signal due to further metabolic conversion of ALCAR to citrate via AcCoA at the conversion rate  $k_{ALCi}$ :

$$\frac{1}{T_{1,AL}^*} = \frac{1}{T_{1,AL}} + k_{ALCi} \quad (44)$$

One potential source of error in the model is the assumption that the effective relaxation time, and therefore the flux out of the labeled ALCAR pool, does not change between two experiments. The apparent conversion rate  $k_{AcAL}$  was calculated by using an assumed relaxation time  $T_{1,AL}$  of 20 s and measuring the magnetization of the two compounds. ALCAR excitation by a 90° pulse saturates the magnetization at this timepoint ( $t = 0$ ). Thus,  $M_{AL}(t = 0)$  equals zero, and the entire signal at the next timepoint ( $t = \Delta t$ ) reflects the conversion of acetate to ALCAR between the two measurements (see Figure 33). The differential equation (43) is then solved as follows:

$$M_{AL}(\Delta t) = -k_{AcAL}M_{Ac}T_{1,AL}^* \exp\left(-\frac{\Delta t}{T_{1,AL}^*}\right) + k_{AcAL}M_{Ac}T_{1,AL}^* \quad (45)$$

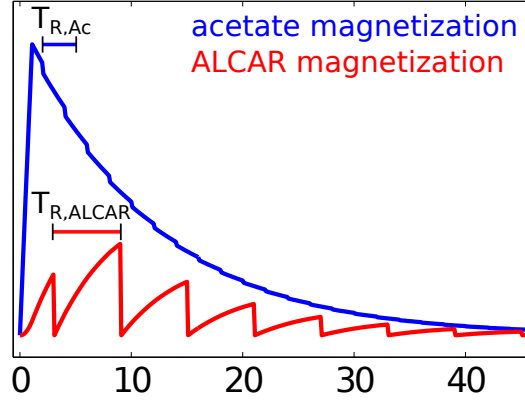


Figure 33: Schematic illustration of the behavior of the magnetization of acetate and ALCAR. The ALCAR magnetization is depleted at each acquisition; the entire signal at the next timepoint represents conversion during the time  $T_{R,ALCAR}$ .

The conversion rate is determined by

$$k_{AcAL} = \frac{M_{AL}}{M_{Ac}} \cdot \frac{1}{-T_{1,AL}^* \exp(-\frac{\Delta t}{T_{1,AL}^*}) + T_{1,AL}^*} \quad (46)$$

$M_{AL} = S_{AL}$ , and  $M_{Ac} = S_{Ac}/\sin(\vartheta_{Ac})$ . The signals  $S_{AL}/S_{Ac}$  were measured for acetate/ALCAR;  $\vartheta_{Ac}$  is the flip angle for acetate. Notably, the second factor in eq. (46) can be approximated as  $1/\Delta t$ , as shown in [89] for pyruvate conversion rates. This is not the case here, as a longer duration  $\Delta t$  is required for the slower acetate conversion to build up the ALCAR pool and gain sufficient SNR. To calculate  $k_{AcAL}$ , the three acetate intensities between the two ALCAR excitations were averaged in each ROI and are denoted as  $S_{Ac}$  in eq. (46). Note that the measured rate  $k_{AcAL}$  is called the apparent conversion rate, as there are some uncertainties. It is affected by the ROI selection, pulse imperfections, and the assumed relaxation rate  $T_{1,AL}^*$ . However, it makes it possible to quantify the activity of the conversion for comparison studies in which alterations of this metabolic system are of interest.

### In Vivo Test

The time-resolved imaging sequence was tested in a healthy Fisher rat prepared and monitored as described in chapter 5.3. The images acquired in this test and the results of the quantification of the conversion rate are shown in Figure 34. Each metabolic image in Figure 34a is scaled to its maximal intensity, to give an impression of the SNR and artifact performance.

The acetate excitation yields maps (Figure 34 a; first row) with a high SNR for all the timepoints considered for quantification. This is important for quantification,

since the signal intensity determines the denominator in the calculation of  $k_{AcAL}$ . Hence, high variance in this value would lead to an extremely unreliable result.

In the first ALCAR map (Figure 34 a; second row), some spiral artifacts from spectral misinterpretation of the acetate signal are visible; this image was acquired during acetate bolus arrival and should be excluded for the  $k_{AcAL}$  evaluation in any event, since acetate saturation would cause underestimation of the conversion. As in the single-timestep images, the ALCAR maps differ from the acetate map because the ALCAR signal originates from the left ventricle, whereas the acetate signal arises over the entire heart. The SNR is acceptable for six measurements after injection (Figure 34 b), so averaging five timesteps enables a robust estimation of the conversion rate (Figure 34 c).

The IDEAL-encoded acetate images after ALCAR excitation (Figure 34 a; third row) exhibit considerable signal in the cardiac region in the first three images. This shows again that IDEAL encoding is necessary, as residual excitation of acetate would cause image distortion after ALCAR excitation.

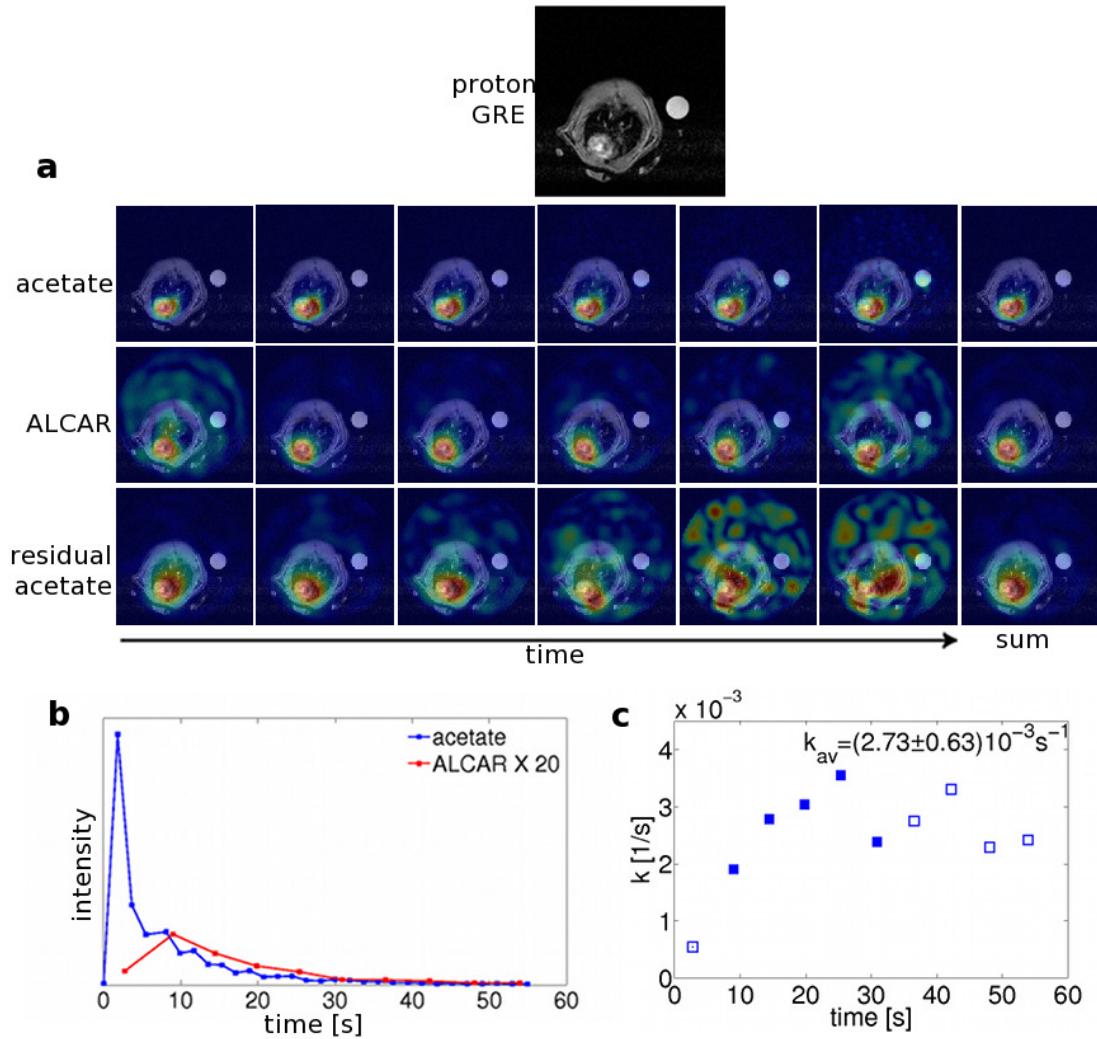


Figure 34: a: Single-shot acetate maps with the pulse centered on the acetate frequency (first row); IDEAL-decoded ALCAR and acetate maps with the pulse centered on ALCAR (second and third rows). The images are scaled to their maximal intensity. b: Time development of the acetate and ALCAR signals inside an ROI drawn manually over the left ventricle. c: Apparent conversion rate  $k_{AcAL}$  calculated according to eq. (46). Open symbols are excluded from the average estimation.

#### 5.2.4 Discussion

The proposed imaging method provides the first published maps of acetate and ALCAR in cardiac and skeletal muscle. The single-shot images are robust against artifacts and provide good image quality; for this approach, the higher resolution can be recommended. For time-resolved imaging, the lower resolution for ALCAR

demonstrated that the saturation recovery approach offers an ALCAR signal that can be quantified for several timepoints and that a stable result for the apparent conversion rate can be obtained.

To improve the image quality, the sequence could be triggered on the heartbeat, which was technically not possible using our setup. The data stability for single-shot imaging could be further improved by applying bolus tracking [112], which would better determine the optimal timepoint where the ALCAR signal is assumed to be highest. An SPSP pulse could also be designed as a multiband pulse [90], and all the images could be acquired in combination with IDEAL encoding. These images would benefit in originating from the same excitation. Both metabolites would have to be recorded with the same trajectory. However, the independence of the ALCAR and acetate maps is advantageous for the time-resolved imaging approach. More timepoints can be recorded for acetate than for ALCAR, and the additionally measured data between the relatively long  $T_R$ , during which the metabolite magnetization accumulates, improve the quantification of the substrate.

## 5.3 Investigation of the Effect of Dobutamine-Induced Stress on Acetate Metabolism

For potential clinical implementation of metabolic HP [1-<sup>13</sup>C]acetate imaging, the low SNR of ALCAR would be a diagnostic challenge. Especially for studies in which the signal ratio serves as a negative marker for pathological changes, it would be favorable to have a higher baseline ratio to improve the contrast between healthy and diseased tissue. To this end, the catecholamine dobutamine, which induces stress and increases cardiac workload, could potentially improve the ALCAR SNR and image quality. The effect of dobutamine-induced stress on cardiac signal development of acetate and ALCAR was investigated in healthy rats with HP MR spectroscopy and imaging.

### 5.3.1 Methods

For this study, the SPSP pulse described in chapter 5.1 was used to optimize the SNR for slice-selective spectroscopy as well as for imaging. The pulse was combined with the IDEAL spiral encoding scheme (chapter 5.2). For time-resolved imaging, the saturation recovery sequence described in chapter 5.2.3 was used to quantify the apparent conversion rates in the heart as well as in the skeletal muscle.

#### Experimental Setup

The substrate was prepared as described in chapter 4.2. Fifteen seconds after dissolution, the acetate solution (120 mM) was administered at a dose of 5 ml per kilogram of body weight into the tail vein inside the MR scanner for approximately 3 s. The rats were anesthetized with 1%–3% isoflurane, and the electrocardiogram, blood oxygenation, respiratory rate, and temperature were monitored (*SA Instruments*, Stony Brook, NY, US). Body temperature was maintained using a circulating warm water heating pad. Eleven male Lewis rats ( $304 \pm 31$  g) and six male Fisher rats ( $291 \pm 53$  g) were measured for the spectroscopy and imaging studies, respectively. The study was approved by the local government committee for animal protection and welfare (Tierschutzbehörde, Regierung von Oberbayern). All in vivo measurements were performed on a 3 T GE HDx scanner, and the <sup>13</sup>C MR scans and proton reference scans were acquired with a dual-tuned <sup>1</sup>H–<sup>13</sup>C volume coil for RF transmission and reception ([102]) (see chapter 4.1).

#### Spectroscopy

Spectra were measured in a 12 mm axial slice containing the entire heart but also a part of the animals' skeletal back muscle. Acquisition of spectra began with acetate administration; the alternating excitations had a repetition time of 5 s for each of the two frequencies. The flip-angle-corrected signal intensities of both

molecules during the first 60 s after administration were summed, and finally the total signal ratio of ALCAR/acetate was calculated.

### Dobutamine-Induced Stress

All animals underwent two  $^{13}\text{C}$  MR measurements, the first in the basal state at the beginning of anesthesia and the second approximately 75 min later. In all the rats (except for the control group,  $n = 4$ ), stress was induced with dobutamine, which was administered before the second scan through another tail vein catheter.

A previously established dosage regime for dobutamine administration [113] was used ( $5 \mu\text{g}/\text{min}/\text{kg}$  for 2 min;  $10 \mu\text{g}/\text{min}/\text{kg}$  for 2 min;  $20 \mu\text{g}/\text{min}/\text{kg}$  for 9 min). The heart rate increased from approximately 300 bpm initially to more than 450 bpm at the end of dobutamine administration; this stress reaction occurred in every animal. This dobutamine protocol was applied to seven rats for spectroscopy and to all six rats for the imaging study. To control for potential metabolic influence of the first acetate administration on the second one and for the effects of anesthesia, a control group of four animals underwent two  $^{13}\text{C}$  MR sessions without any dobutamine injection.

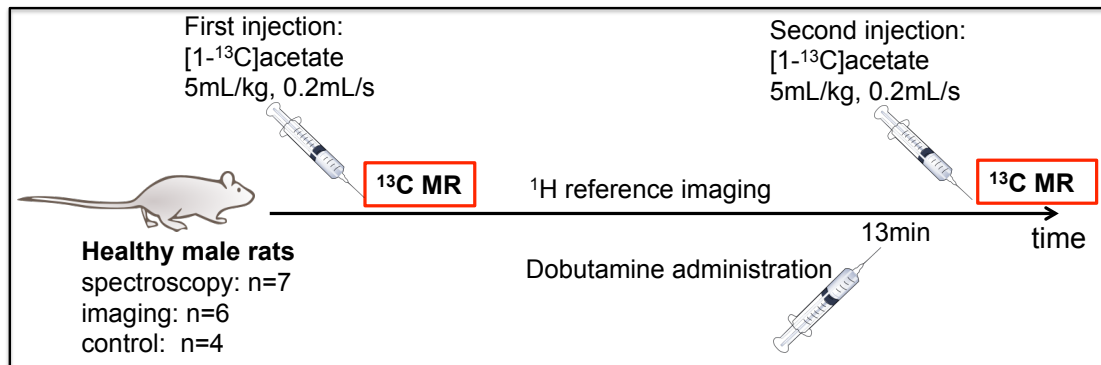


Figure 35: Overview of the study protocol. Except for the animals in the control group, stress was induced with dobutamine before the second acetate injection.

## 5.3.2 Results

### Spectral Acquisition

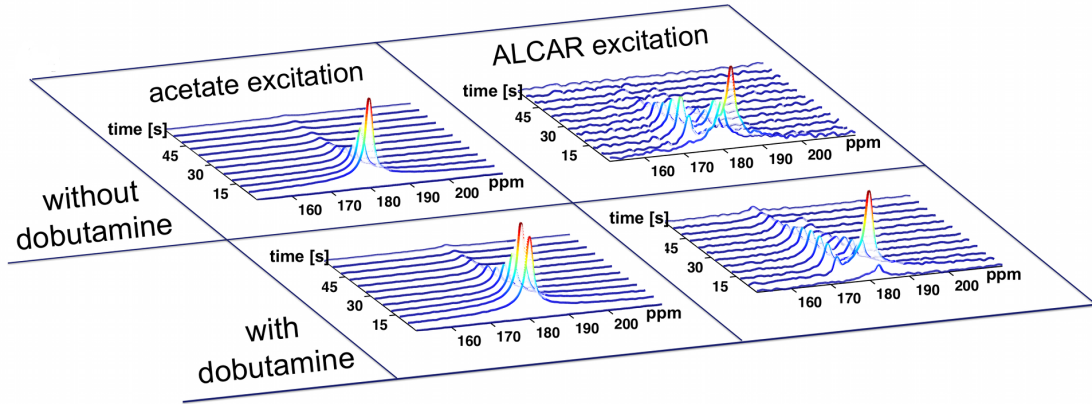


Figure 36: Spectra acquired after acetate and ALCAR excitation in two states: Without dobutamine induced stress (upper row) and under stress (lower row). Figure previously published in [53].

Figure 36 shows the time course of two representative spectral datasets containing the rat heart and part of the back muscle; i.e., the spectral data are the sums of signals from these areas. The presented spectral dataset is evaluated in Figure 37 (first row) together with the time curves of signal amplitudes measured in another animal (second row). The amplitudes were significantly affected by the induced stress, which is reflected by the consistent increase in the ALCAR/acetate ratio across the datasets. During the first acetate injection, the average ALCAR/acetate ratio ( $n = 7$ ) was  $3.83 \pm 1.14\%$ . With dobutamine administration before the second acetate injection, the ratio increased to  $5.64 \pm 1.31\%$  (Figure 38). A paired one-tailed  $t$ -test revealed a significant increase ( $p < 0.05$ ) in the ALCAR/acetate ratio by an absolute value of  $0.49\%$ , which is  $12.8\%$  of the average ratio without dobutamine injection. The measured cardiac ratios of the rats in the rest/stress group (D1–D7) are given in Table 2 with the values of the control group (C1–C4). In addition to the increased ratio, higher signals of both acetate and ALCAR were observed in the stressed state at later timepoints (Figures 36 and 37).

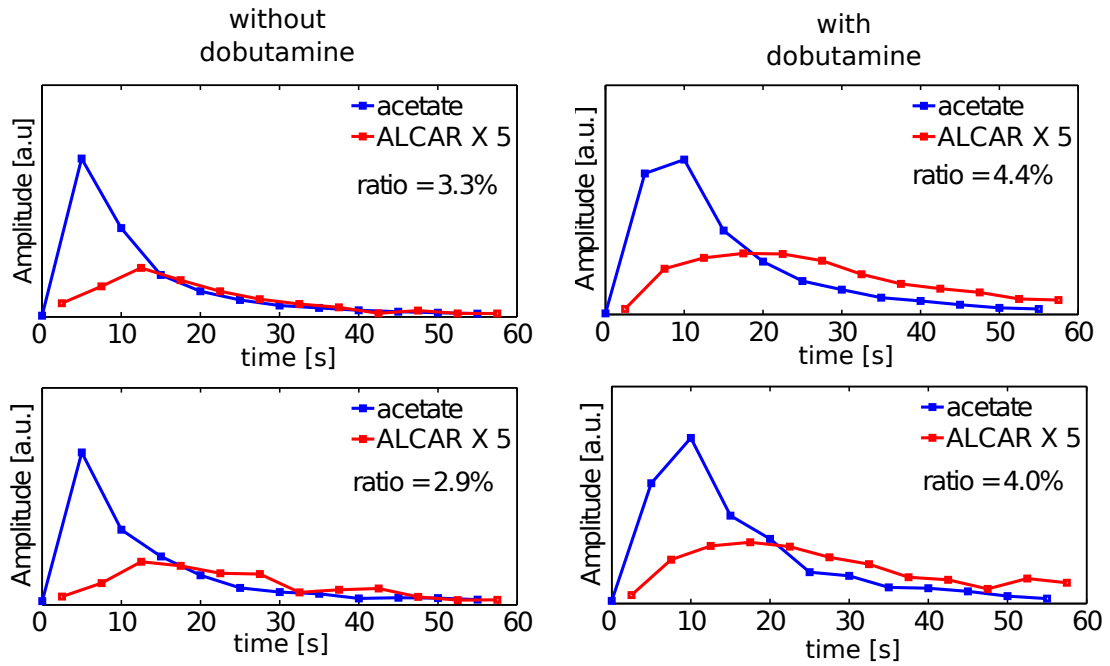


Figure 37: Examples of the time development of the acetate and ALCAR signals in two animals (one animal each row). The sums over the signal intensities during 60 s after the start of the injection were used to calculate the ALCAR/acetate ratios. The ALCAR/acetate ratio and the absolute signals of both molecules increase, especially at later timepoints (same scaling in both graphs for each animal). Partly previously published in [53].

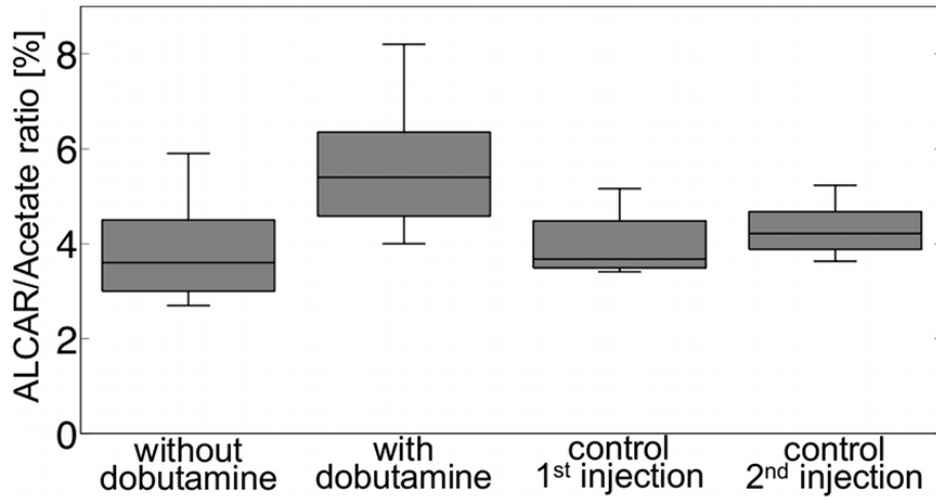


Figure 38: ALCAR/acetate ratio without and with dobutamine-induced stress. The box plot shows minima, 25th percentiles, medians, 75th percentiles, and maxima. A paired one-tailed  $t$ -test confirms a significant increase ( $p < 0.05$ ) in the ratio by a value of 0.49% (12.8% of the ratio without stress). Previously published in [53].

| <b>a: Rest/Stress</b> | D1  | D2  | D3  | D4  | D5  | D6  | D7  | Mean $\pm$ STD  |
|-----------------------|-----|-----|-----|-----|-----|-----|-----|-----------------|
| Ratio w/o Dob. [%]    | 3.6 | 2.7 | 2.9 | 5.9 | 3.6 | 3.3 | 4.8 | 3.83 $\pm$ 1.14 |
| Ratio w/o Dob. [%]    | 6.5 | 6.2 | 4.0 | 5.1 | 5.4 | 4.4 | 5.9 | 5.64 $\pm$ 1.31 |

| <b>b: Control</b> | C1  | C2  | C3  | C4  | Mean $\pm$ STD  |
|-------------------|-----|-----|-----|-----|-----------------|
| Ratio 1st In. [%] | 5.2 | 3.6 | 3.8 | 3.4 | 3.98 $\pm$ 0.80 |
| Ratio 2nd In. [%] | 5.2 | 3.7 | 4.1 | 4.3 | 4.32 $\pm$ 0.67 |

Table 2: a: Measured ALCAR/acetate signal ratios for the rats that underwent one injection without and one injection with dobutamine-induced stress ( $n = 7$ , rats D1–D7). b: Measured ratios for the control group (C1–C4) with two  $^{13}\text{C}$  acetate injections without any dobutamine administered.

### Imaging study

The same protocol was used for the imaging study as for the spectroscopy (see Figure 35) in order to localize the metabolic changes after stress induction. Therefore, rats were assessed using single-timepoint imaging as well as the time-resolved saturation recovery sequence. Typical results of single-timepoint imaging are shown in Figure 39, where again the ALCAR images were acquired with different resolutions. The maps in the rest and stressed states appear similar overall; the SNR in the cardiac region is also similar. However, an important difference in the signal distributions was found in these images: In the stressed condition, the ALCAR map shows an enhanced signal originating from the back skeletal muscle. Additionally, an elevated acetate signal was located in this region. These observations are clearest in the lower-resolution images, which have a higher SNR. This indicates that the muscle is better perfused under stress, and more acetate is converted here during the observation time window.

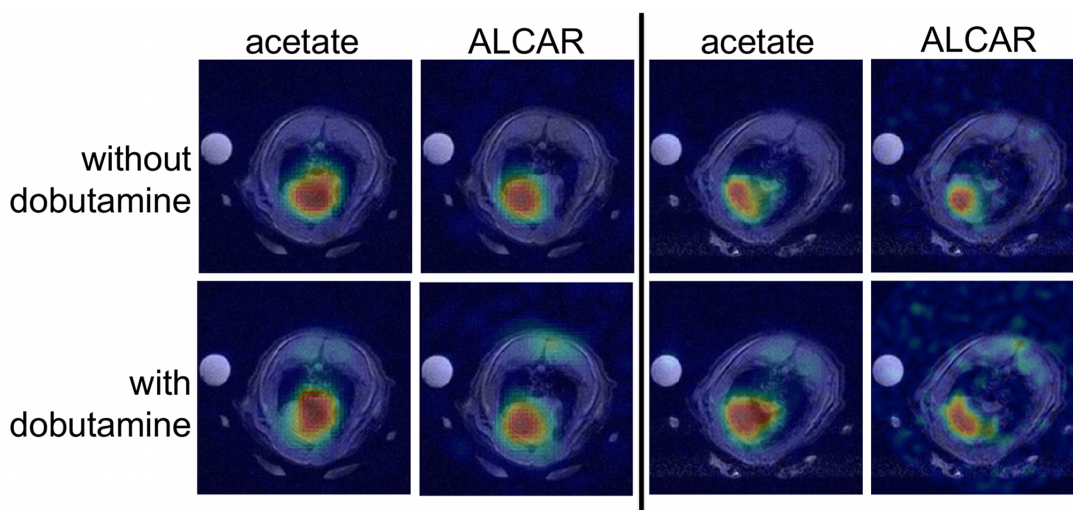


Figure 39: Comparison of lower-resolution (real resolution:  $10 \times 10 \text{mm}^2$ ) (left) and higher-resolution (real resolution:  $5 \times 5 \text{mm}^2$ ) (right) ALCAR images before and after dobutamine treatment. The real resolution of the acetate images was  $5 \times 5 \text{mm}^2$  in both cases. Most of the ALCAR signal stems from the cardiac region, but after dobutamine treatment, there is also significant signal from the skeletal muscle in the back. Previously published in [53].

Figure 40 shows a series of images over time before (a) and after (b) dobutamine administration. The ALCAR images (second row) show an acceptable cardiac SNR in four to five images, depending on the respiration trigger timing. At the first timepoint, the images of the peripheral musculature are corrupted because part of the cardiac signal is projected onto this region by spiral chemical shift artifacts. Therefore, the first timepoint should be excluded from quantitative analysis of the

skeletal muscle.

Using the quantitative analysis of the signal intensities according to eq. (46), the apparent conversion rates  $k_{AcAL}$  (shown in Figure 41) were calculated. In the heart, the result was stable within 30 s after acetate administration. Therefore, several  $k_{AcAL}$  measurements can be averaged after one injection, which increases data reliability. In agreement with the previous single-shot imaging results, under induced stress no measurable increase of the cardiac conversion rate was observed; it actually decreased slightly. In skeletal muscle,  $k_{AcAL}$  is hardly measurable without induced stress. As mentioned above, the ALCAR images initially contain artifacts in the back muscle area, and subsequently the SNR decreases to below the threshold value of 3. Furthermore, the conversion rate is more sensitive to contamination by artifacts due to the low acetate signal in the skeletal muscle, since the measured magnetization  $M_{Ac}$  is in the denominator of eq. (46). As a result, the apparent conversion rate measured without stress may be overestimated. In contrast, the skeletal muscle clearly converts more acetate at a higher conversion rate in the stressed condition. This causes a higher overall SNR of ALCAR and enables  $k$ -value measurement at several timepoints. These results are consistent with the observations in the spectroscopy study, as the signal measured there reflects the sum of that in the cardiac and skeletal muscle areas.

To merge the data obtained using the different imaging techniques in order to investigate the effects of dobutamine, for each dataset the total signal ratio was calculated for a cardiac and a skeletal muscle ROI. The calculated ratio without induced stress was designated as 100%, and the ratio change after dobutamine administration was calculated and averaged for the existing six datasets. The average signal ratio change ( $n = 6$ ) was  $-20 \pm 27\%$  in the heart ROI and  $+27 \pm 54\%$  in the skeletal muscle. The ratio over the entire slice increased under stress by  $+16 \pm 41\%$ .

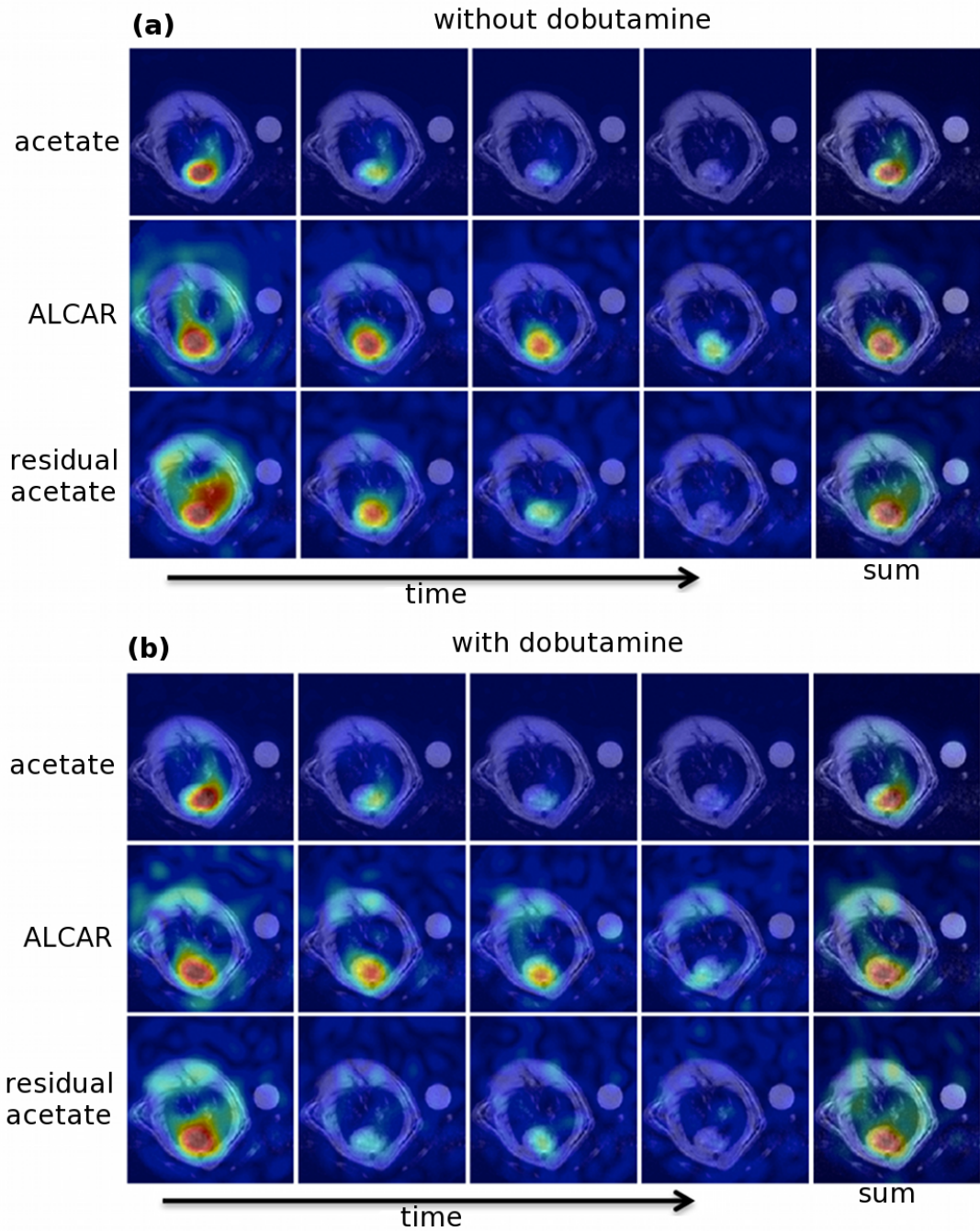


Figure 40: Time-resolved imaging; without dobutamine (a), the ALCAR signal originates primarily from the heart, whereas under stress (b), metabolism is also visualized in the skeletal muscle area. The images show an acceptable SNR for four to five timepoints depending on the trigger. Each row is scaled to its maximum signal. Previously published in [53].

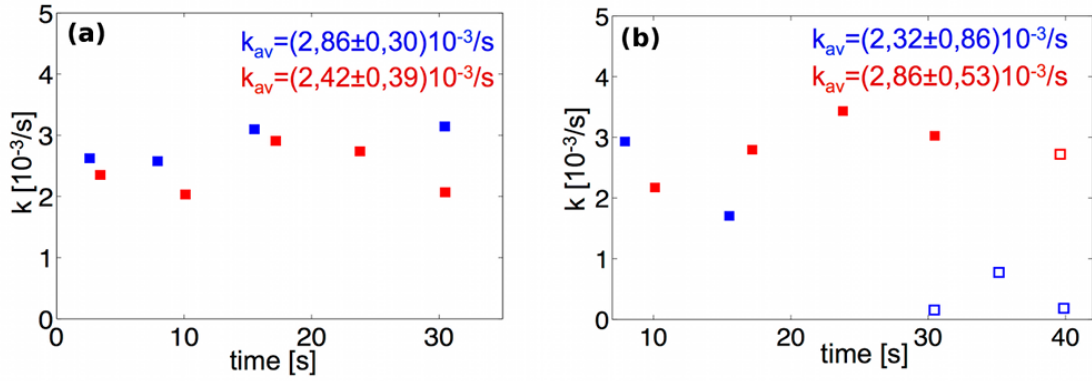


Figure 41: Apparent conversion rates without (blue) and with (red) dobutamine-induced stress in cardiac (a) and skeletal (b) muscle regions. Open symbols represent timepoints that were excluded because of low ALCAR SNR. Previously published in [53].

### 5.3.3 Discussion

In the spectroscopy study, the signal ratio increased significantly under stress, as expected. The enhanced acetate signal, particularly at later timepoints ( $>30$  s), may indicate higher acetate uptake into myocardial cells. However, it could also originate from the skeletal muscle within the same slice.

The results of the imaging study concerning the alteration of the ALCAR/acetate ratio during dobutamine-induced stress are remarkable. Although most of the ALCAR and acetate signal originates from the heart, a notable signal arises from skeletal muscle, where the activity is clearly increased under stress. Ignoring the impact of the skeletal muscle could cause misinterpretation of the slice-selective spectra. We assume that under stress, substrate transport into the highly vascularized skeletal muscle is faster. Consequently, more acetate could be metabolized during the time window of an HP experiment. Contrary to expectations, the results show that dobutamine administration does not increase the ALCAR/acetate ratio in cardiac muscle and that therefore the SNR of ALCAR does not increase. On the one hand, it is possible that the activation of acetate via ACS and CAT-1 to ALCAR does not increase. On the other hand, more activation (as expected) combined with more flux out of the labeled ALCAR pool toward the TCA cycle into citrate would yield the same result. These two scenarios cannot be distinguished using this setup, since the low chemical shift difference between citrate and acetate does not allow separation of their signals. Thus, the presented method of quantifying the apparent conversion rate does not directly represent the activity of acetate metabolism. However, it could be used as a marker of metabolic pathologies that affect the activation of acetate via ACS to ALCAR, such as ischemia [30]. To

separate and quantify the citrate signal, imaging at a higher magnetic field with improved spectral resolution could potentially enable an extension of the kinetic model of eq. (43) in order to investigate the TCA cycle activity of acetate.

The merged imaging data also imply that the signal ratio decreases in cardiac tissue and increases in skeletal muscle. However, the high data variability, particularly in the single-shot images, prevents statistical analysis of the significance.

## 5.4 Investigation of Metabolic Changes in STZ-Diabetic Rats with Hyperpolarized [1-<sup>13</sup>C]Acetate

### 5.4.1 Introduction

As described in chapter 3.1.4, acetate might serve as a marker for pathological changes in cells' fuel selection, as they occur in diabetes patients. This study investigates whether the ratio of ALCAR to acetate, measured with noninvasive HP [1-<sup>13</sup>C]acetate MR spectroscopy, could serve as a marker for myocardial, hepatic, and renal metabolic changes in rats with STZ-induced diabetes in vivo. This study shows that the conversion of acetate to ALCAR could be detected and quantified in all three organs of interest and, more interestingly, that the HP ALCAR/acetate ratio is independent of the blood glucose level and prolonged hyperglycemia following diabetes induction in a type-1 diabetes model.

### 5.4.2 Methods

#### <sup>13</sup>C MR Acquisition

For this study, the pulse described in chapter 5.1 was used. Slice-selective spectra of three 12-mm-thick slices including the heart, liver, and kidneys, respectively, were acquired in each animal with a  $T_R$  of 3 s for each metabolite. The flip angle was set to 4° for acetate and 15° for ALCAR excitation.

Additionally, time-resolved acetate maps were acquired with a single-arm spiral trajectory over an  $8 \times 8$  cm<sup>2</sup> FOV with a real resolution of  $5 \times 5$  mm<sup>2</sup> at a flip angle of  $\vartheta = 10^\circ$  and  $T_R = 3$  s. The trajectory and reconstruction are described in chapter 5.2. As a reference for these images, <sup>1</sup>H gradient echoes for each slice were recorded before the injection.

#### Quantification

The spectra of both molecules during the first 60 s after acetate injection began were flip angle corrected and summed. The total ALCAR/acetate signal ratio was calculated from the absolute value of this sum. Additionally, an in vivo estimation of the relaxation time was extracted from the data. Therefore, the acetate intensities starting 20 s after injection were evaluated and fitted to a monoexponential decay curve. The last intensity considered for this fit was determined by the first SNR value below 3. The fitting result was considered relevant if the fitted data included at least eight signal intensities. As this fit does not distinguish relaxation from metabolism, the result of the fit is called the apparent longitudinal relaxation time  $T_1^*$ .

## Statistics

The values of the signal ratios were investigated for their agreement with the normal distribution by a quantile–quantile plot. The values differing from the normal distribution by a  $p$  value of 0.05 were excluded and marked as outliers, most likely due to an error in the acquisition of the metabolic information. For a statistical investigation of the ratios of the healthy and the diabetic group, an unpaired student's  $t$ -test was applied.

## Animals

A group of  $n = 12$  eight-week-old female Wistar rats (Taconic, Ry, Denmark) weighing  $178.5 \pm 8.4$  g were included in the study. Rats were randomized to control ( $n = 5$ ) or diabetes ( $n = 7$ ) groups. Diabetes was induced by an intravenous injection of STZ (55 mg per kilogram of body weight; Sigma-Aldrich, St. Louis, MO, US) dissolved in 10 mmol/l of cold citrate buffer (pH 4.5). The MR session occurred three weeks later. The blood glucose of each animal was measured in tail capillary blood with a Contour blood glucose meter (Bayer Diabetes Care, Copenhagen, Denmark). All animals had free access to water and standard chow throughout the study. The rats were kept in cages with a 12 : 12 h light–dark cycle, a temperature of  $21 \pm 2$  °C, and a humidity of  $55 \pm 5\%$ . Before the MR session, the diabetic rats had an average blood glucose concentration of  $15.9 \pm 5.9$  mmol/l and a body weight of  $216 \pm 9$  g. The healthy control group's blood glucose concentration was  $7.5 \pm 0.3$  mmol/l and weight was  $222 \pm 13$  g. During the MR session, the animals were anesthetized with 2.5% sevoflurane in oxygen as the breathing gas. The body temperature was kept constant at 37.0°C, and oxygenation of the blood was monitored with a blood oximeter; because of the breathing gas, the blood of all the rats was close to oxygen saturation (98% – 100%). The study complied with the guidelines for the use and care of laboratory animals and was approved by the Danish Inspectorate of Animal Experiments.

## Substrate Preparation and Hardware

The substrate was prepared by mixing 48 wt% of sodium [1-<sup>13</sup>C]acetate with 30 wt% water and 22 wt% glycerol and adding 15 mM OXO63 radical [104]. The mixture (150 ml) was polarized in a 5 T SPINlab for 180 min and dissolved in a PBS-buffered solution. This procedure yielded a liquid polarization level of about 20%. All the MR experiments were performed on a 3 T GE HDx scanner. Proton reference scans and <sup>13</sup>C scans were acquired with a dual-tuned <sup>1</sup>H–<sup>13</sup>C volume coil for RF transmission and reception [102] (chapter 4.1).

### 5.4.3 Results

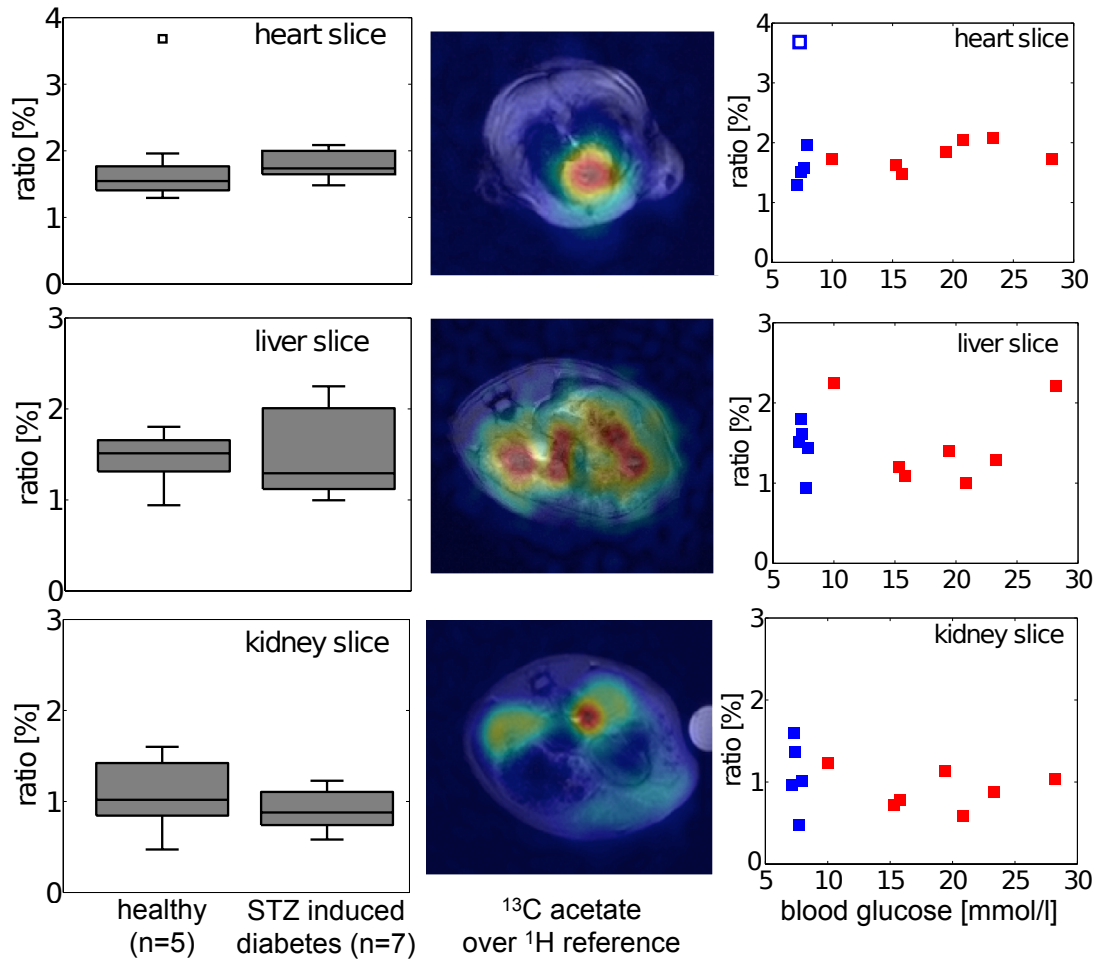


Figure 42: ALCAR/acetate ratio in healthy and diabetic rats. First column shows box plots giving median, 25th and 75th percentile, maximum, and minimum values for each slice. In the third column, the ratio is plotted versus the blood glucose concentration (healthy animals, blue; diabetic animals, red).

The measured ALCAR/acetate ratios in the heart, liver, and kidney slices are shown in Figure 42. The box plots of the ratios measured in the diabetic and control groups show the median, 25th and 75th percentiles, minimum, and maximum values of each dataset. In all three slices, no statistically significant difference was found between the healthy and diabetic groups. The  $p$  values calculated with the student's t-test (given in Table 3) confirm that there is no statistically significant difference between the two groups. The mean and standard deviation of the values measured in the healthy ( $n = 5$ ) and diabetic ( $n = 7$ ) rats are also given in Table

3. In the heart slice, one datapoint was excluded as an outlier (see Figure 42) and was not considered in the statistical analysis.

In the second column of Figure 42, typical acetate maps for the three slices are shown; the proton reference images are given as background. These maps were averaged over three excitations acquired from 15 to 24 s after the end of the injection in a diabetic animal. The images demonstrate that the substrate is well distributed in each organ of interest, whereas the signal from skeletal muscle regions is negligible.

Furthermore, in the third column of Figure 42, the ALCAR/acetate signal ratios are plotted versus the measured blood glucose levels. No significant correlation appears for any of the three organs of interest.

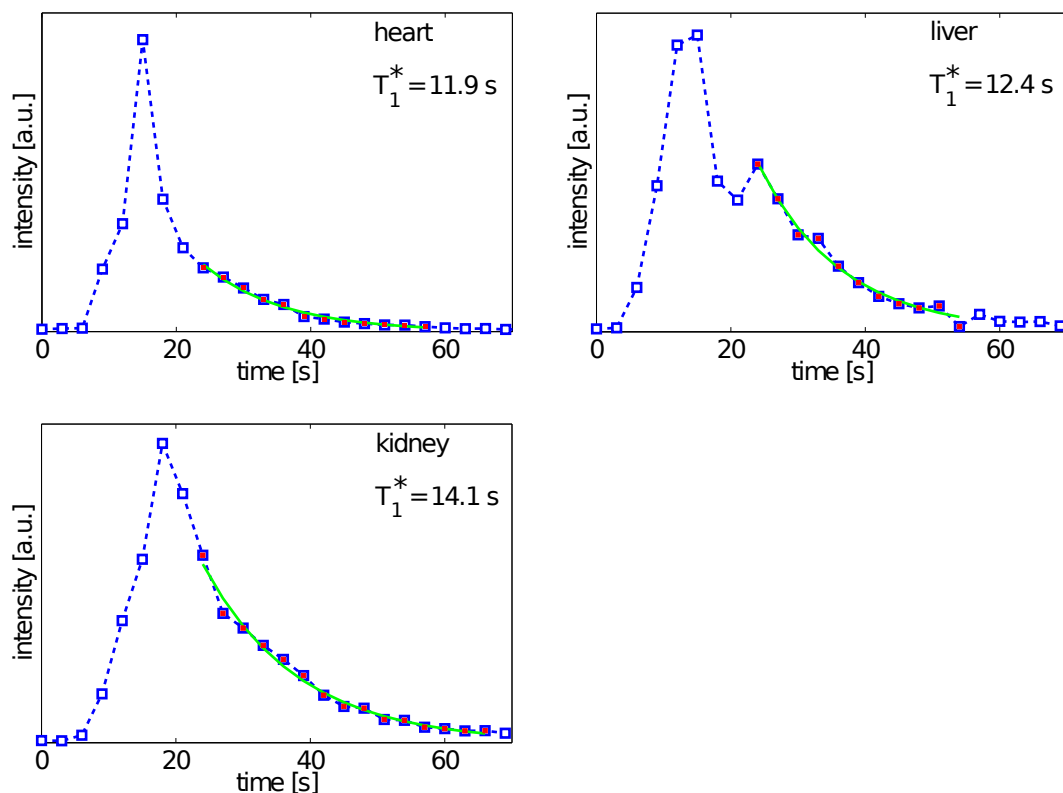


Figure 43: Example of acetate time course and fitting of the apparent longitudinal relaxation times  $T_1^*$ . The datapoints relevant for the fit are shown in solid red; the monoexponential fitting curve is drawn in green.

The apparent longitudinal relaxation times  $T_1^*$  fitted for each slice and averaged over all ( $n = 12$ ) of the animals are shown in Table 3. As an example, the acetate curve and  $T_1^*$  fit for one diabetic animal are shown in Figure 43. Considering the data for all the animals, the relaxation times did not differ between the healthy and

diabetic groups in any of the three slices. Thus, the relaxation time was averaged over all animals. In the heart slice, the value is slightly shorter ( $12.4 \pm 1.2$  s) than in the other organs (liver  $14.3 \pm 2.6$  s, kidneys  $14.0 \pm 1.7$  s). The in vivo time  $T_1^*$  averaged over all three slices, neglecting conversion through metabolism of  $[1-^{13}\text{C}]$ acetate at 3 T, was  $13.7 \pm 2.1$  s.

| Slice  | Ratio Healthy ( $n$ ) | Ratio Diabetic ( $n$ ) | $p$ Value | $T_1^*$ ( $n = 12$ ) |
|--------|-----------------------|------------------------|-----------|----------------------|
| Heart  | $1.59 \pm 0.28\%$ (4) | $1.79 \pm 0.22\%$ (4)  | 0.21      | $12.4 \pm 1.2$ s     |
| Liver  | $1.46 \pm 0.32\%$ (5) | $1.49 \pm 0.52\%$ (4)  | 0.33      | $14.3 \pm 2.6$ s     |
| Kidney | $1.08 \pm 0.43\%$ (5) | $0.91 \pm 0.23\%$ (4)  | 0.64      | $14.0 \pm 1.7$ s     |

Table 3: ALCAR/acetate signal ratios in healthy and diabetic groups for the three slices investigated. The  $p$  values were calculated with an unpaired student's t-test. The apparent longitudinal relaxation time  $T_1^*$  was averaged over all rats.

#### 5.4.4 Discussion

This study demonstrates that it is feasible to quantify the acetate-to-ALCAR metabolism in a clinical setup using a human 3 T MR system in combination with a polarizer authorized for human studies. The primary limitation of this study is a relatively large variation in the ALCAR/acetate ratio, which is due to the low SNR of the ALCAR data.

The SNR might be increased in a preclinical MR system for small animals with a higher  $B_0$ -field, or by the use of surface coils, which could be placed more closely in particular to the rats heart. However, for hyperpolarized experiments it has to be taken into account, that a higher field leads to shorter longitudinal relaxation times, which could predominate the benefits of the high field [114] [115].

The ALCAR/acetate ratio was not significantly affected in STZ-diabetic animals three weeks after induction of diabetes. This might be explained by the fact that the first step – the reaction from acetate to ALCAR via ACS – is the rate-limiting step of the metabolic pathway. Consequently, an increase in ACC would not strongly affect the amount of ALCAR converted in the time range of interest (1 min). Furthermore, the limited concentration of free CoA might restrict the reaction toward AcCoA, which has the same effect. However, ALCAR is also an intermediate product of acetate metabolism. As mentioned in chapter 5.3.3, conversion away from ALCAR could also be increased by conversion away from ALCAR toward the TCA cycle. Again, this would reduce the ALCAR pool and therefore decrease the examined signal ratio. These signals could potentially be separated in an MR scanner with a stronger field  $B_0$ .

In the kidney slice, there was a slight decrease of the ratio perceptible; however,

this decrease is not statistically significant. The same holds true for the liver, where the variation of the data is bigger, since the SNR of ALCAR is lower than in the heart or the kidney slice.

In addition, this work publishes in vivo measured relaxation times of  $[1-^{13}\text{C}]$ acetate. Neglecting the conversion leads to an underestimation of the real  $T_1$ -time. However, if one takes into account a conversion rate of maximal  $6 \cdot 10^{-3}\text{s}^{-1}$  as reported in other studies for the heart [106] or for the skeletal muscle [28], this systematic error is below 10%. The shorter  $T_1$ -time in the heart could be due to more conversion of acetate, but also due to a net flux out of this slice, especially out of the blood pool. In general the relaxation rate, measured in the heart is dominated by the blood, because of the big pool of blood inside the ventricles. In contrast to that in the kidney the substrate accumulates during the time of the experiments, so that averaging over all three slices leads to a better estimation of the in vivo relaxation time.



## 6 3D Whole-Heart Cardiac Metabolic Imaging in the Pig with [1-<sup>13</sup>C]Pyruvate using IDEAL Spiral CSI

### 6.1 Introduction

Metabolic imaging with HP [1-<sup>13</sup>C]pyruvate has strong potential for examination of myocardial viability and ischemia, as described in chapter 3.2. Therefore, the concentration of bicarbonate and lactate with respect to the pyruvate concentration is very interesting for clinical diagnosis of myocardial abnormalities [23] (see chapter 3.2). Here, a 3D CSI sequence was implemented for whole-heart porcine cardiac imaging. The 3D spatial and 1D spectral image encoding require rapid repetitive excitations, which is advantageous for motion averaging but rapidly depletes the HP magnetization. To address this problem, a multiband pulse [48] was designed with a profile tailored to the metabolites of interest; hence, the magnetization was used very efficiently. This profile was combined with a 3D imaging sequence using IDEAL encoding to limit the number of necessary excitations. The content in this following chapter was previously presented at the 22<sup>nd</sup> conference of the *ISMRM* [116].

### 6.2 Methods

#### Multiband Pulse Design

The multiband pulse was designed to excite the lower-concentration pool of HP lactate and bicarbonate with a fivefold higher flip angle than the injected pyruvate. Additionally, the excitation of alanine and pyruvate hydrate is suppressed (see Figure 44). These molecules are of limited diagnostic interest, and the omission of their excitation reduces the number of frequencies that have to be encoded with the CSI sequence after the RF pulse. This makes it possible to reduce the number of CS encoding steps and thus allows more rapid acquisition. A disadvantage of the relatively long multiband pulse is that it implies a slight loss of signal due to  $T_2^*$  decay of the magnetization during the effective echo time.

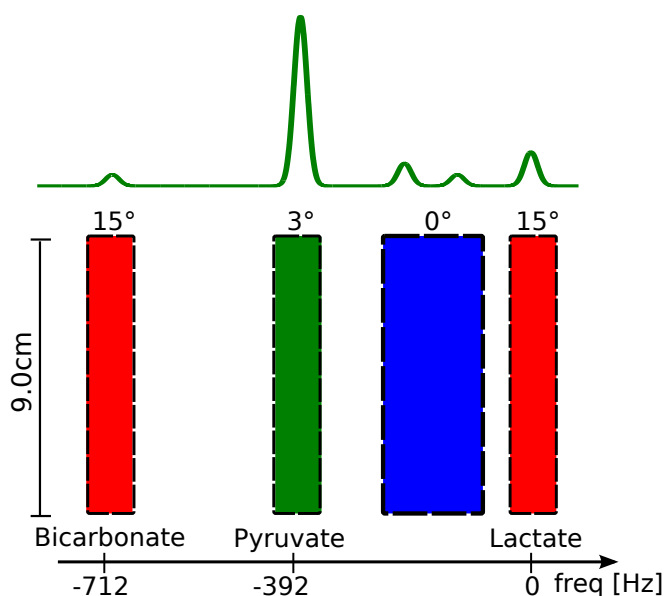


Figure 44: Desired SPSP pulse profile: The lower-concentration pools of HP lactate and bicarbonate are excited with a fivefold higher flip angle than the substrate pyruvate. Excitation of pyruvate hydrate ( $-125$  Hz) and alanine ( $-215$  Hz) are suppressed for more effective chemical shift encoding.

For the pulse design, flyback gradient modulation was chosen because of its high stability against gradient errors; e.g., gradient–RF delays can occur and degrade the profile. The system’s maximal gradient strength (40 mT/m) and slew rate (150 T/sm) were exploited. An aliasing pattern was used to excite lactate and bicarbonate with the same flip angle. This means that the subpulse duration was set to the inverse of their chemical shift difference (712 Hz) of their Larmor frequency: ( $\tau_{sub} = 1/712$  Hz  $\approx 1.4$  ms). In contrast to the SPSP pulse designed for acetate application, the pulse profile required here is not symmetric. It can be realized only by changing the RF during the pulse, which can be described mathematically as phase accumulation during the excitation, which is represented by a complex waveform. Fifteen sublobes were chosen as a compromise between a well-defined spectral pulse profile and a limited pulse duration. As a result, the total duration was 21 ms, which was achieved with an isodelay (the time between the center of the RF amplitude and the end of the pulse) of  $t_{iso} = 9.1$  ms. The pulse was fitted to the desired profile as described in chapter 3.3. Figure 44 shows the waveform of the multiband pulse (a) and a magnified view of the shape of one subpulse (b). The spectral–spatial pulse profile (c) was measured in the proton setup with a water phantom doped with 4% Dotarem using the method described in chapter 5.1.2.

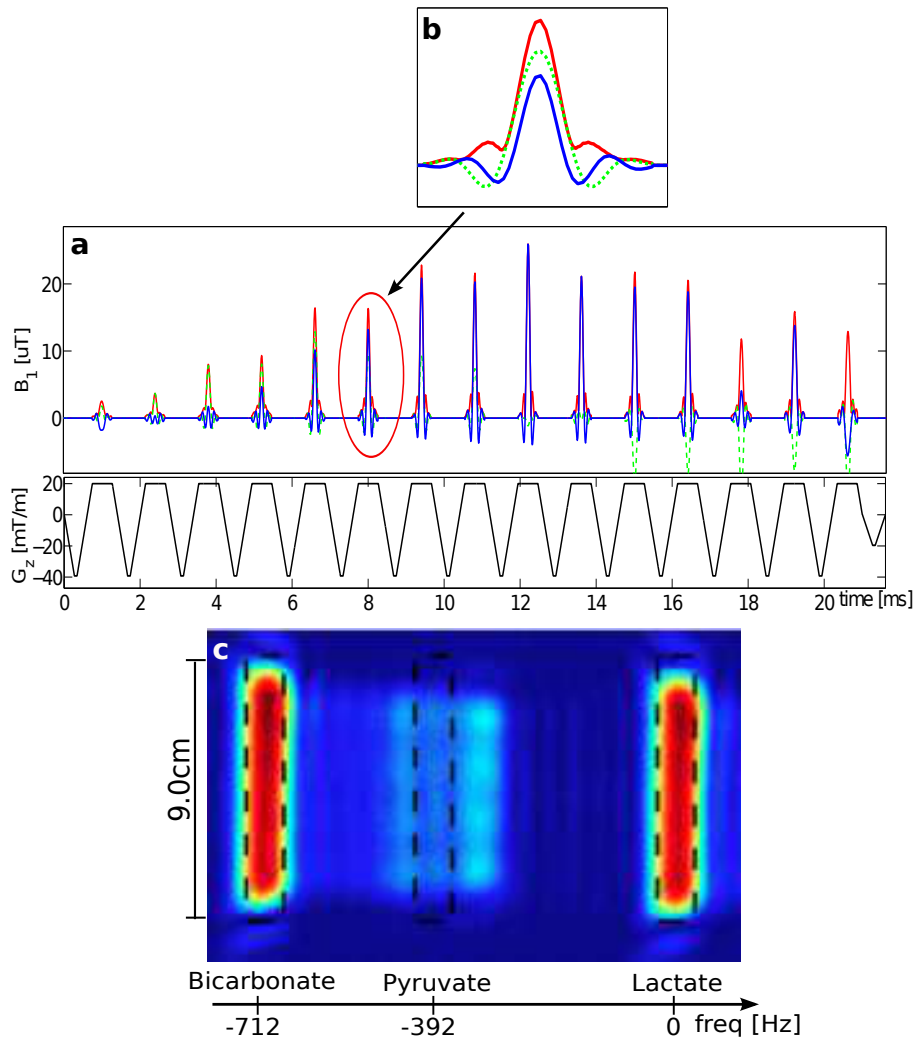


Figure 45: a: Waveform of the multiband pulse. Top: RF waveform. Real part (blue), imaginary part (green), and absolute value (red). Bottom: Gradient waveform. b: Shape of one subpulse, which defines the spatial excitation. c: Spectral-spatial pulse profile measured using a  $^1\text{H}$  phantom.

### Sequence Design

Figure 47 shows an overview of the 3D  $^{13}\text{C}$  imaging sequence. After the excitation of a 9.0-cm-thick slab containing the whole heart, the signal was phase-encoded in the  $z$  direction. The density of the  $k_z$ -space sampling was Gaussian weighted around the  $k_z$ -space center, which gives the PSF a Gaussian shape in the  $z$  direction. For the slab thickness of 9.0 cm, nine encoding steps were recorded. As a third step, IDEAL spiral encoding was performed with an IDEAL echo time shift optimized to maximize the NSA (see chapter 3.4.2). Five ( $Q = 5$ ) IDEAL

timesteps were chosen for robust encoding of the spectral information for the three ( $M = 3$ ) metabolite frequencies (lactate: 0 Hz, pyruvate:  $-392$  Hz, bicarbonate:  $-712$  Hz). The numerically calculated NSA, which is measuring the conditioning of the IDEAL encoding matrix for each frequency of interest (see chapter 3.4.2), is plotted for each frequency versus the echo time shift  $\Delta T_E$  (Figure 6.2). An optimal NSA value for the three frequencies is reached at a  $\Delta T_E$  value of 0.56 ms.

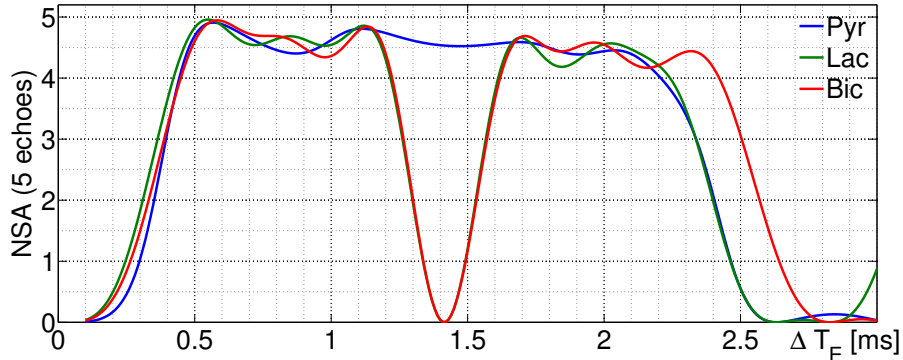


Figure 46: NSA for the frequencies of pyruvate, lactate, and bicarbonate with five IDEAL encoding steps.

The in-plane ( $x,y$ ) readout was a single-shot spiral trajectory with an FOV of 30 cm, a nominal resolution of 8 mm, and a duration of 42 ms using the maximal gradient strength (40 mT/m) and maximal slew rate (150 T/m) of the system. Additionally, five FIDs of the entire slice were recorded during acquisition and used as target frequencies for IDEAL reconstruction and for inspection of the signal development during acquisition. The sequence orientation was set to the short-axis orientation defined for the anatomical proton images. Acquisition was started 18 s after injection, at which the maximum of the bicarbonate signal appeared in previous spectroscopy studies [29]. With the described settings, 45 excitations (+5 FIDs) are necessary for one set of metabolite maps. With a potential repetition time of  $T_R \sim 100$  ms, this leads to a total acquisition time of 4.5 s. In principle, the technique can acquire several images at different timepoints. The major limitation of the metabolite maps is the SNR, so there is a trade-off between time resolution and image quality. In this work, only single-timepoint images were acquired, and the acquisition was triggered on the pigs' heartbeat (about  $80 \text{ min}^{-1}$ ). Within each cardiac cycle, four excitations were performed. The resulting effective echo time was about 190 ms (total time of about 9 s), depending on the current cardiac rate.

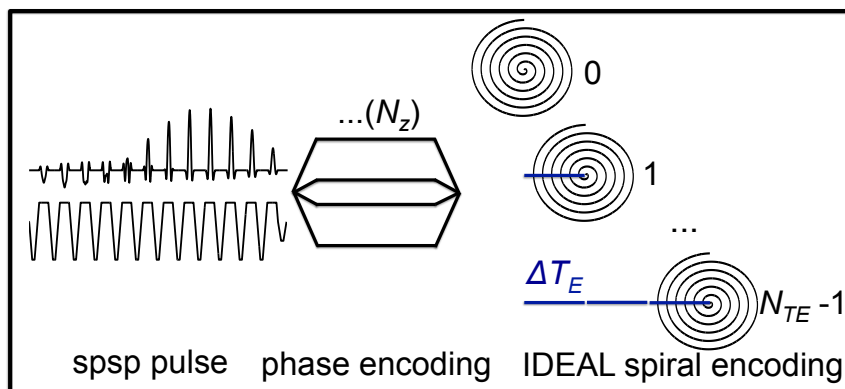


Figure 47: 3D pulse sequence: The multiband pulse excites a slab, followed by one of  $N_z$  Gaussian-weighted phase-encoding steps in the  $z$  direction and one of  $N_{TE}$  IDEAL-spiral-encoding steps. The excitation has to be repeated  $N_z \cdot N_{TE}$  times for one set of 3D metabolic maps.

### Experimental Setup

The protocol for the polarization of a large dose of HP [1- $^{13}\text{C}$ ]pyruvate was previously established at the *Fondazione CNR Regione Toscana* in Pisa and is described in more detail in [117]. Therefore, a dose of 350  $\mu\text{l}$  of [1- $^{13}\text{C}$ ]pyruvate was formulated with concentrations of [[1- $^{13}\text{C}$ ]pyruvate] = 14 M, [OXO63] = 15 mM, and [Dotarem] = 1 mM. The polarizer in Pisa is the same model (DNP HyperSense, Oxford Instruments, UK) as that described in chapter 4.1. The probe was dissolved in 10 ml of dissolution medium (0.27 mM  $\text{Na}_2\text{EDTA}$  in water); the final formulation was obtained by external dilution of the dissolution medium in a buffered aqueous solution (200 Trizma, 0.4 mM  $\text{NaOH}$  in MQ water) to a final [1- $^{13}\text{C}$ ]pyruvate concentration of 230 mM at body temperature and an isotonic pH. Finally, 20 ml of the HP [1- $^{13}\text{C}$ ]pyruvate solution was manually injected in a bolus of about 10 s into the right ear vein of the pig (effective injected dose: 0.13 mmol per kilogram of body weight). Simultaneously, 1 ml was transferred to a 1 T spectrometer (chapter 4.1) to assess the  $T_1$  relaxation time and liquid-state polarization. The MR experiments were conducted on a 3 T GE HDx system (chapter 4.1). A single-tuned quadrature  $^{13}\text{C}$  birdcage coil with an inner diameter of 35 cm was used for transmission. Reception was performed with a 16-channel phase array coil (for more details, see chapter 4.1, [103]). Proton reference and positioning scans were performed with the product's body coil integrated into the MR scanner. Automatic shimming was executed during the prescan of the proton scan; the resulting shimming values were applied during  $^{13}\text{C}$  acquisition.

Reconstruction was performed as described in chapter 3.4.2. After IDEAL decoding, demodulation, and spatial reconstruction, the data finally have to be reconstructed for phase encoding in the  $z$  direction. For spiral in-plane encoding, a Gaussian filter (15 Hz) was applied to account for the  $T_2^*$  decay during spiral

$(k_x, k_y)$  acquisition.

### 6.3 Results and Discussion

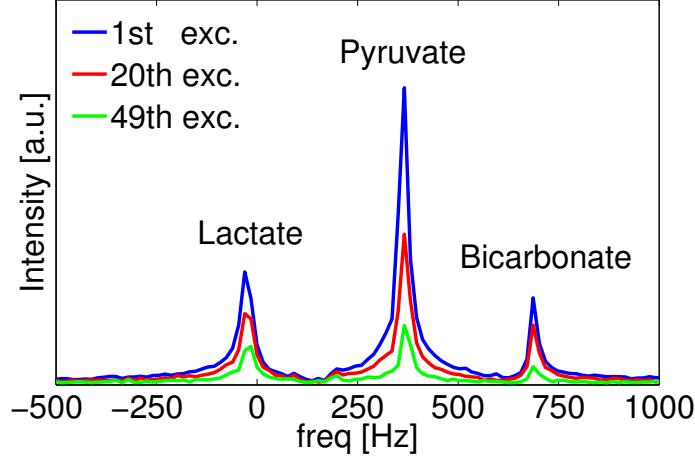


Figure 48: Magnitude spectra acquired between 3D imaging sequences.

The absolute spectra acquired during the 3D imaging sequence (Figure 6.3) exhibit a high SNR of both metabolites of interest (lactate and bicarbonate). The difference between the first (blue) and the last acquisition (green) shows that most of the signal is used up owing to excitation and  $T_1$  decay during the measurement. Furthermore the spectra demonstrate, that the signals of pyruvate-hydrate (125Hz) and alanine (215 Hz) are effectively suppressed.

The results of 3D imaging of this exemplary dataset are shown in Figure 6.3 in the short-axis and long-axis orientations. The myocardium of the left ventricle is clearly depicted in both the bicarbonate and lactate images. The long-axis-oriented map shows that the reaction toward both metabolites occurs over the entire myocardium, as expected for a healthy animal.

The bicarbonate maps exhibit the lowest SNR in all ( $n = 4$ ) datasets. An increase in the lactate signal at the cost of a decrease in the bicarbonate signal was observed with increasing anesthesia time. As the sequence was tested along with other sequences developed for the porcine heart, two datasets were acquired after a second injection of pyruvate in the same animal; thus, the pig was under anesthesia for more than 90 min. In the datasets acquired after the second pyruvate injection, bicarbonate was not detectable. Thus, it is recommended to acquire only one HP dataset per pig in each session and to keep the anesthesia as short as possible. Furthermore, the control of blood oxygenation and the use of intubation

in combination with oxygen-enriched air potentially improves the reproducibility of the results by minimizing the biological variation and breathing movement during the acquisition time. Because an array of surface coils was used, the myocardial tissue close to the arrays has a higher SNR than the areas deeper inside the animal's body owing to the varying sensitivity of the reception coils. Since any pathological diagnosis requires the relative signal (bicarbonate to lactate), the variation in the SNR within one image can be tolerated if both signals are strong enough to be quantified at any point.

The pyruvate maps exhibit a high SNR, although they were acquired with a low flip angle of only  $3^\circ$ . As expected, they are dominated by the blood pool inside the two ventricles, where the pyruvate concentration is relatively high.

The signal was well confined to the cardiac region overall, so the trajectory could be adapted to a smaller FOV (e.g., 20 cm). Furthermore, bolus tracking (described for HP [ $1\text{-}^{13}\text{C}$ ]pyruvate in [112]) could be applied to find the optimal starting time for the sequence. With this approach, acquisition starts at a defined time after the arrival of the substrate and thus excludes the variations in the sequence timing depending on the injection speed.

As a next step, the sequence should be tested in a disease model for cardiac ischemia and reperfusion, as it is described in [118]. With that the conversion from HP pyruvate to bicarbonate and lactate could be correlated with both, proton MR images acquired with a relaxation agent, giving evidence about the perfusion of the tissue and following histological analysis. This would enable a more detailed view onto the potential of the technique for clinical diagnosis.

In conclusion, this work demonstrates that 3D localization of [ $1\text{-}^{13}\text{C}$ ]pyruvate metabolism by accurate depiction of the [ $1\text{-}^{13}\text{C}$ ]lactate and [ $1\text{-}^{13}\text{C}$ ]bicarbonate distributions over the entire left ventricle – which represent the activity of the enzymes LDH and PDH, respectively (chapter 3.2) – is feasible. IDEAL spiral CSI in three dimensions, in combination with the use of a multiband pulse, provides artifact robustness and high image quality.

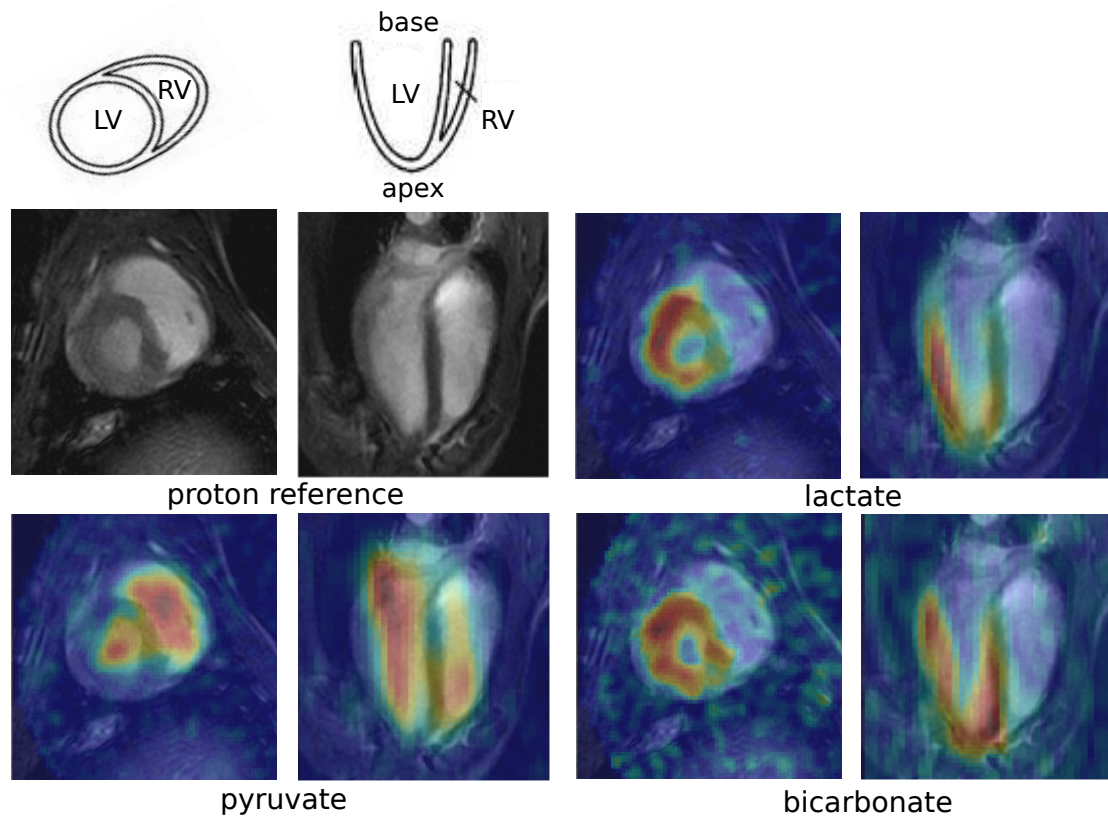


Figure 49: Pyruvate, lactate, and bicarbonate maps in short-axis (left) and long-axis (right) views overlying the proton reference scan (shown upper left). The color maps are scaled to the maximum of each metabolite map. The myocardium of the left ventricle is clearly visible in both metabolite images (lac, bic), whereas pyruvate is localized mainly in the blood pool inside both ventricles.



## 7 Conclusion

### 7.1 Summary

The major goal of this work was to investigate the potential of [1-<sup>13</sup>C]acetate as a tracer for in vivo hyperpolarization studies using a clinical MR scanner. This investigation yielded an imaging framework that demonstrated the feasibility of quantitative ALCAR-to-acetate mapping.

First, the DNP procedure for Na[1-<sup>13</sup>C]acetate highly concentrated in glycerol with an OXO radical and a small concentration of gadoteric acid was optimized (chapter 4). This resulted in a high polarization level of about 22%, which is above the previously published levels for Na[1-<sup>13</sup>C]acetate [28], and a  $T_1$  time of 72 s in the dissolution media.

The pulse implementation described in chapter 5.1 opens the door to in vivo investigation of acetate using a clinical 3 T scanner. It enables the separation of the ALCAR signal from the dominant acetate peak and thus makes it possible to record slice-selective spectral time curves. In vivo spectroscopy demonstrates that acetate is a potential tracer for the heart, where the conversion rate is highest, and for the kidneys, where more acetate accumulates with a lower conversion rate. The spectra ultimately delivered a valid in vivo estimate of the longitudinal relaxation time  $T_1$  of about 14 s.

The imaging framework for acetate and ALCAR, described in chapter 5.2, combines the high encoding efficiency of spectral separation via IDEAL with the benign SNR behavior of a spiral gradient readout. Single-timepoint images show high-quality ALCAR maps with a resolution down to  $5 \times 5 \text{ mm}^2$ . For dynamic imaging, the combination of IDEAL spiral encoding with the saturation recovery technique enables robust quantification of the conversion from acetate to ALCAR inside a cardiac ROI for several timepoints (about five). However, the limited resolution of  $10 \times 10 \times 12 \text{ mm}^3$  does not allow spatial separation of the blood pool and myocardium.

The proposed imaging sequence can be adopted for metabolic imaging with any other HP substance with a relatively low conversion rate, where the substrate peak folds into the spectral area of the relatively low metabolite peak, as for example for bicarbonate and CO<sub>2</sub> imaging [119].

An investigation of the effects of dobutamine-induced stress (chapter 5.3) on the ALCAR/acetate ratio yielded remarkable results: Spectroscopy over a slice containing a whole rat heart showed a significant increase in the ratio. The imaging studies suggested that this increase can be attributed to the skeletal muscle area in the animal's back. Whether the stable ratio in the heart is due to further reaction out of the labeled ALCAR pool toward the TCA cycle, or cardiac acetate conversion is limited by the concentrations of the (co-)enzymes (ACS, CAT, and CoA) remains unclear. Investigations at a higher field strength with an increased

spectral resolution are necessary to resolve this issue, since the chemical shift difference between acetate and the next metabolic product, citrate, is relatively small.

Chapter 5.4 describes an investigation of the ALCAR/acetate ratio in a rat model of type-1 diabetes. This study demonstrated that the signal ratio does not change significantly with the blood glucose level and prolonged hyperglycemia (three weeks) following diabetes induction. When an experimental setup similar to the human HP MR setup is used, acetate is not suitable as a marker for cardiac, renal, or hepatic metabolic changes occurring in early diabetes. Again, investigations at a stronger magnetic field might yield more information about acetate metabolism, in particular about its contribution to energy production via the TCA cycle.

Finally, 3D IDEAL spiral CSI with multiband excitation was demonstrated to be feasible for  $[1-^{13}\text{C}]$ pyruvate metabolic imaging of the porcine heart by accurately depicting pyruvate lactate and bicarbonate distributions over the entire left ventricle. The images exhibit convincing quality, as they are artifact-free maps of the metabolites lactate and bicarbonate and have a suitable SNR.

## 7.2 Outlook

As mentioned above, an investigation of the cardiac acetate metabolism at a higher field strength in order to increase the chemical shift separation is of huge interest and will be performed in the near future in healthy rats as well as in rats with STZ -induced diabetes.

Furthermore, it could be of preclinical interest to validate the hindered reaction of acetate to acetylcarnitine for myocardial ischemia, as it was demonstrated in perfused rat hearts [30] in an in vivo setting. Therefore, the implementation of an imaging framework, as presented here, is crucial.

In order to get more closer to a clinical application, spectroscopy was recently performed with HP acetate in pigs [120]. For imaging, the bigger structures in the porcine heart and the slower heartbeat – enabling cardiac triggering – in comparison to rats are an advantage. However, the final concentration of the tracer will be lower in the big animal model. As a first step to potentially establish acetate imaging in pigs, it has to be tested whether the signal of acetylcarnitine is high enough to reach a reasonable resolution in order to draw meaningful pathological statements.

Moreover, an investigation of the cardiac acetate metabolism might be interesting in combination with HP pyruvate, which could give explicit information about the heart's fuel selection and investigate correlations between changes in the metabolism of both molecules. If the experiments were conducted with HP  $[1-^{13}\text{C}]$ acetate and  $[1-^{13}\text{C}]$ pyruvate, the injections would have to be performed one after another, since the chemical shift of  $[1-^{13}\text{C}]$ acetate and  $[1-^{13}\text{C}]$ lactate is simi-

lar, which would lead to an overlapping of the spectra and hence to difficulties in peak-separation.

In conclusion, the in vivo investigation of HP acetate is of high significance for researching a variety of diseases and disorders particularly in the myocardium. Metabolic imaging of acetate opens the door for the localization of changes in the activity of enzymes and coenzymes involved in the pathway, namely acetylco synthetase, carnitine acetyltransferase, and coenzyme-A. Thus, the technique has a huge impact on preclinical research in order to help to investigate metabolic alterations as a basis for myocardial abnormalities. However, the slow conversion from acetate to acetylcarnitine via two metabolic steps diminishes the propability that cardiac imaging of HP acetate will be relevant for clinical praxis as a diagnostic tool.

Cardiac metabolic imaging with hyperpolarized pyruvate offers huge potential for the diagnosis of left ventricular dysfunction in clinical application, since the delivered metabolic information, the differentiation of healthy, ischemic, and viable myocardium, is unique. 3D sequences are of huge interest; they are preferable versus a stack of two-dimensional acquisitions due to their artifact behavior. The proposed sequence is convincing due to the restriction of the number of necessary encoding steps by IDEAL encoding and the supression of excitations of metabolites of minor interest with the multiband pulse. Additionally, the multiband pulse offers the possibility to exploit the HP magnetization very efficiently. This enables high quality imaging of the whole heart. An imaging method could similarly be set up for human trials with HP [1-<sup>13</sup>C]pyruvate.

In general, the field investigating HP <sup>13</sup>C substances is rapidly growing, since currently several new DNP polarizers are becoming operational. The majority of them is certified for clinical applications under sterile conditions. With the translation from preclinical science in animal models to clinical trials in human, the impact of this technology will be clearer. Establishing the DNP procedure in a clinical surrounding creates a variety of new challenges, including a longer waiting time in between the dissolution and the injection for an adequate filtering and quality control of the solution, which leads to a loss of polarization. Following the example of successfully demonstrating the tumor detection with [1-<sup>13</sup>C]pyruvate in prostate tumor patients [18], several groups are currently working to overcome these issues and to implement cardiac imaging with pyruvate for human trials. This could open the door for a highly beneficial tool for diagnosis, treatment response, and clinical decision-making for cardiac diseases.



## References

- [1] W. Gerlach and O. Stern, “Der experimentelle nachweis der richtungsquantelung im magnetfeld,” *Zeitschrift für Physik A Hadrons and Nuclei*, vol. 9, no. 1, pp. 349–352, 1922.
- [2] I. I. Rabi, “Space quantization in a gyrating magnetic field,” *Physical Review*, vol. 51, no. 8, pp. 652–654, 1937.
- [3] F. Bloch, W. W. Hansen, and M. Packard, “Nuclear induction,” *Physical Review*, vol. 69, no. 3-4, p. 127, 1946.
- [4] E. M. Purcell, H. C. Torrey, and R. V. Pound, “Resonance absorption by nuclear magnetic moments in a solid,” *Physical Review*, vol. 69, no. 1-2, pp. 37–38, 1946.
- [5] P. Mansfield and P. K. Grannell, “Nmr ‘diffraction’ in solids?,” *Journal of Physics C: solid state physics*, vol. 6, no. 22, p. L422, 1973.
- [6] P. C. Lauterbur *et al.*, “Image formation by induced local interactions: examples employing nuclear magnetic resonance,” *Nature*, vol. 242, no. 5394, pp. 190–191, 1973.
- [7] J. Hennig, A. Nauerth, and H. Friedburg, “RARE Imaging: A Fast Imaging Method for Clinical MR,” *Magnetic Resonance in Medicine*, vol. 3, pp. 823–833, 1986.
- [8] A. Haase, J. Frahm, D. Matthaei, W. Haenicke, and K.-D. Merboldt, “FLASH Imaging. Rapid NMR Imaging Using Low Flip-Angle Pulses,” *Journal of Magnetic Resonance*, vol. 67, pp. 258–266, 1986.
- [9] P. B. Roemer, W. A. Edelstein, C. E. Hayes, S. P. Souza, and O. M. Mueller, “The NMR phased array,” *Magnetic Resonance in Medicine*, vol. 16, no. 2, pp. 192–225, 1990.
- [10] K. P. Pruessmann, M. Weiger, M. B. Scheidegger, and P. Boesiger, “SENSE: Sensitivity Encoding for Fast MRI,” *Magnetic Resonance in Medicine*, vol. 42, no. 5, pp. 952–962, 1999.
- [11] M. A. Griswold, P. M. Jakob, R. M. Heidemann, M. Nittka, V. Jellus, J. Wang, B. Kiefer, and A. Haase, “Generalized Autocalibrating Partially Parallel Acquisitions (GRAPPA),” *Magnetic Resonance in Medicine*, vol. 47, no. 6, pp. 1202–1210, 2002.
- [12] J. Frahm, K.-D. Merboldt, and W. Hänicke, “Functional mri of human brain activation at high spatial resolution,” *Magnetic Resonance in Medicine*, vol. 29, no. 1, pp. 139–144, 1993.

- [13] J. H. Ardenkjaer-Larsen, B. Fridlund, A. Gram, G. Hansson, L. Hansson, M. H. Lerche, R. Servin, M. Thaning, and K. Golman, "Increase in signal-to-noise ratio of  $> 10,000$  times in liquid-state nmr," *Proc Natl Acad Sci U S A*, vol. 100, no. 18, pp. 10158–63, 2003.
- [14] M. J. Albers, R. Bok, A. P. Chen, C. H. Cunningham, M. L. Zierhut, V. Y. Zhang, S. J. Kohler, J. Tropp, R. E. Hurd, Y.-F. Yen, *et al.*, "Hyperpolarized  $^{13}\text{C}$  lactate, pyruvate, and alanine: Noninvasive biomarkers for prostate cancer detection and grading," *Cancer research*, vol. 68, no. 20, pp. 8607–8615, 2008.
- [15] A. P. Chen, M. J. Albers, C. H. Cunningham, S. J. Kohler, Y.-F. Yen, R. E. Hurd, J. Tropp, R. Bok, J. M. Pauly, S. J. Nelson, *et al.*, "Hyperpolarized  $c\text{-}^{13}$  spectroscopic imaging of the tramp mouse at 3t? initial experience," *Magnetic resonance in medicine*, vol. 58, no. 6, pp. 1099–1106, 2007.
- [16] S. E. Day, M. I. Kettunen, F. A. Gallagher, D.-E. Hu, M. Lerche, J. Wolber, K. Golman, J. H. Ardenkjaer-Larsen, and K. M. Brindle, "Detecting tumor response to treatment using hyperpolarized  $^{13}\text{C}$  magnetic resonance imaging and spectroscopy," *Nature medicine*, vol. 13, no. 11, pp. 1382–1387, 2007.
- [17] S. Kohler, Y. Yen, J. Wolber, A. Chen, M. Albers, R. Bok, V. Zhang, J. Tropp, S. Nelson, D. Vigneron, *et al.*, "In vivo  $^{13}\text{C}$  metabolic imaging at 3t with hyperpolarized  $^{13}\text{C}$ -1-pyruvate," *Magnetic Resonance in Medicine*, vol. 58, no. 1, pp. 65–69, 2007.
- [18] S. J. Nelson, J. Kurhanewicz, D. B. Vigneron, P. E. Larson, A. L. Harzstark, M. Ferrone, M. van Criekinge, J. W. Chang, R. Bok, I. Park, *et al.*, "Metabolic imaging of patients with prostate cancer using hyperpolarized [1- $^{13}\text{C}$ ] pyruvate," *Science translational medicine*, vol. 5, no. 198, pp. 198ra108–198ra108, 2013.
- [19] M. E. Merritt, C. Harrison, C. Storey, F. M. Jeffrey, A. D. Sherry, and C. R. Malloy, "Hyperpolarized  $^{13}\text{C}$  allows a direct measure of flux through a single enzyme-catalyzed step by NMR," *Proceedings of the National Academy of Sciences of the United States of America*, vol. 104, no. 50, pp. 19773–19777, 2007.
- [20] K. Golman, J. S. Petersson, P. Magnusson, E. Johansson, P. Åkeson, C.-M. Chai, G. Hansson, and S. Månsson, "Cardiac metabolism measured non-invasively by hyperpolarized  $^{13}\text{C}$  MRI," *Magnetic Resonance in Medicine*, vol. 59, no. 5, pp. 1005–1013, 2008.
- [21] M. E. Merritt, C. Harrison, C. Storey, A. D. Sherry, and C. R. Malloy, "Inhibition of carbohydrate oxidation during the first minute of reperfusion

- after brief ischemia: NMR detection of hyperpolarized  $^{13}\text{CO}_2$  and  $\text{H}^{13}\text{CO}_3^-$ ,” *Magnetic Resonance in Medicine*, vol. 60, no. 5, pp. 1029–1036, 2008.
- [22] M. A. Schroeder, L. E. Cochlin, L. C. Heather, K. Clarke, G. K. Radda, and D. J. Tyler, “In vivo assessment of pyruvate dehydrogenase flux in the heart using hyperpolarized carbon-13 magnetic resonance,” *Proceedings of the National Academy of Sciences of the United States of America*, vol. 105, no. 33, pp. 12051–12056, 2008.
- [23] C. R. Malloy, M. E. Merritt, and A. D. Sherry, “Could  $^{13}\text{C}$  mri assist clinical decision-making for patients with heart disease?,” *NMR Biomed*, vol. 24, no. 8, pp. 973–9, 2011.
- [24] G. D. Lopaschuk, J. R. Ussher, C. D. Folmes, J. S. Jaswal, and W. C. Stanley, “Myocardial fatty acid metabolism in health and disease,” *Physiol Rev*, vol. 90, no. 1, pp. 207–58, 2010.
- [25] W. C. Stanley, F. A. Recchia, and G. D. Lopaschuk, “Myocardial substrate metabolism in the normal and failing heart,” *Physiol Rev*, vol. 85, no. 3, pp. 1093–129, 2005.
- [26] V. Lionetti, W. C. Stanley, and F. A. Recchia, “Modulating fatty acid oxidation in heart failure,” *Cardiovasc Res*, vol. 90, no. 2, pp. 202–9, 2011.
- [27] A. L. Kerbey, P. J. Randle, R. H. Cooper, S. Whitehouse, H. T. Pask, and R. M. Denton, “Regulation of pyruvate dehydrogenase in rat heart,” *Biochem J*, vol. 154, no. 2, pp. 327–48, 1976.
- [28] J. A. Bastiaansen, T. Cheng, M. Mishkovsky, J. M. Duarte, A. Comment, and R. Gruetter, “In vivo enzymatic activity of acetylcoa synthetase in skeletal muscle revealed by  $^{13}\text{C}$  turnover from hyperpolarized  $[1-^{13}\text{C}]$ acetate to  $[1-^{13}\text{C}]$ acetylcarnitine,” *Biochim Biophys Acta*, vol. 1830, no. 8, pp. 4171–8, 2013.
- [29] L. Menichetti, F. Frijia, A. Flori, F. Wiesinger, V. Lionetti, G. Giovannetti, G. D. Aquaro, F. A. Recchia, J. H. Ardenkjaer-Larsen, M. F. Santarelli, *et al.*, “Assessment of real-time myocardial uptake and enzymatic conversion of hyperpolarized  $[1-^{13}\text{C}]$  pyruvate in pigs using slice selective magnetic resonance spectroscopy,” *Contrast media & molecular imaging*, vol. 7, no. 1, pp. 85–94, 2012.
- [30] P. R. Jensen, T. Peitersen, M. Karlsson, R. In ’t Zandt, A. Gisselsson, G. Hansson, S. Meier, and M. H. Lerche, “Tissue-specific short chain fatty acid metabolism and slow metabolic recovery after ischemia from hyperpolarized nmr in vivo,” *J Biol Chem*, vol. 284, no. 52, pp. 36077–82, 2009.

- [31] S. B. Reeder, M. Markl, H. Yu, J. C. Hellinger, R. J. Herfkens, and N. J. Pelc, “Cardiac cine imaging with ideal water-fat separation and steady-state free precession,” *J Magn Reson Imaging*, vol. 22, no. 1, pp. 44–52, 2005.
- [32] P. Zeeman, “The Effect of Magnetisation on the Nature of Light Emitted by a Substance,” *Nature*, vol. 55, p. 347, 1897.
- [33] A. Oppelt, *Imaging Systems for Medical Diagnostics*. Publicis Publishing, 2005.
- [34] M. F. Reiser, W. Semmler, and H. Hricak, *Magnetic Resonance Tomography*. Springer Verlag, 2008.
- [35] R. K. Harris, E. D. Becker, S. M. C. D. Menezes, R. Goodfellow, and P. Granger, “NMR nomenclature. Nuclear spin properties and conventions for chemical shifts,” *Pure and Applied Chemistry*, vol. 73, no. 11, pp. 1795–1818, 2001.
- [36] P. Tofts, *Quantitative MRI of the Brain*. John Wiley and Sons, 2003.
- [37] D. B. Twieg, “The k-trajectory formulation of the NMR imaging process with applications in analysis and synthesis of imaging methods,” *Medical Physics*, vol. 10, pp. 610–621, 1983.
- [38] J. W. Cooley and J. W. Tukey, “An algorithm for the machine calculation of complex Fourier series,” *Mathematics of Computation*, vol. 19, pp. 297–301, 1986.
- [39] J. Fessler and B. Sutton, “Nonuniform fast Fourier transforms using min-max interpolation,” *Trans Signal Processing*, vol. 51, pp. 560–574, 2003.
- [40] National High Magnetic Field Laboratory, “<http://nationalmaglab.org/education/magnet-academy/learn-the-basics/stories/mri-a-guided-tour/>,” May 2015.
- [41] M. A. Bouchiat, T. Carver, and C. Varnum, “Nuclear polarization in  $^3\text{He}$  gas induced by optical pumping and dipolar exchange,” *Phys. Rev. Letters*, vol. 5, 1960.
- [42] C. R. Bowers and D. P. Weitekamp, “Transformation of symmetrization order to nuclear-spin magnetization by chemical reaction and nuclear magnetic resonance,” *Phys Rev Lett*, vol. 57, no. 21, pp. 2645–2648, 1986.
- [43] E. R. McCarney, B. D. Armstrong, M. D. Lingwood, and S. Han, “Hyperpolarized water as an authentic magnetic resonance imaging contrast agent,” *Proc Natl Acad Sci U S A*, vol. 104, no. 6, pp. 1754–9, 2007.

- [44] P. Nikolaou, A. M. Coffey, L. L. Walkup, B. M. Gust, N. Whiting, H. Newton, S. Barcus, I. Muradyan, M. Dabaghyan, G. D. Moroz, M. S. Rosen, S. Patz, M. J. Barlow, E. Y. Chekmenev, and B. M. Goodson, "Near-unity nuclear polarization with an open-source  $^{129}\text{Xe}$  hyperpolarizer for nmr and mri," *Proc Natl Acad Sci U S A*, vol. 110, no. 35, pp. 14150–5, 2013.
- [45] G. Pileio, M. Carravetta, E. Hughes, and M. H. Levitt, "The long-lived nuclear singlet state of  $^{15}\text{N}$ -nitrous oxide in solution," *J Am Chem Soc*, vol. 130, no. 38, pp. 12582–3, 2008.
- [46] E. Chiavazza, A. Viale, M. Karlsson, and S. Aime, " $^{15}\text{N}$ -permethylated amino acids as efficient probes for mri-dnp applications," *Contrast Media Mol Imaging*, vol. 8, no. 5, pp. 417–21, 2013.
- [47] K. Golman, M. Lerche, R. Pehrson, J. H. Ardenkjaer-Larsen, *et al.*, "Metabolic imaging by hyperpolarized  $^{13}\text{C}$  magnetic resonance imaging for in vivo tumor diagnosis," *Cancer research*, vol. 66, no. 22, pp. 10855–10860, 2006.
- [48] K. Golman, J. S. Petersson, P. Magnusson, E. Johansson, P. Akeson, C. M. Chai, G. Hansson, and S. Mansson, "Cardiac metabolism measured noninvasively by hyperpolarized  $^{13}\text{C}$  mri," *Magn Reson Med*, vol. 59, no. 5, pp. 1005–13, 2008.
- [49] C. Laustsen, J. A. Ostergaard, M. H. Lauritzen, R. Norregaard, S. Bowen, L. V. Sogaard, A. Flyvbjerg, M. Pedersen, and J. H. Ardenkjaer-Larsen, "Assessment of early diabetic renal changes with hyperpolarized  $[1-^{13}\text{C}]$ pyruvate," *Diabetes Metab Res Rev*, vol. 29, no. 2, pp. 125–9, 2013.
- [50] M. A. Schroeder, L. E. Cochlin, L. C. Heather, K. Clarke, G. K. Radda, and D. J. Tyler, "In vivo assessment of pyruvate dehydrogenase flux in the heart using hyperpolarized carbon-13 magnetic resonance," *Proc Natl Acad Sci U S A*, vol. 105, no. 33, pp. 12051–6, 2008.
- [51] W. A. Edelstein, P. A. Bottomley, and L. M. Pfeifer, "A signal-to-noise calibration procedure for NMR imaging systems," *Medical Physics*, vol. 11, no. 2, pp. 180–185, 1984.
- [52] E. G. Larsson, D. Erdogmus, R. Yan, J. C. Principe, and J. R. Fitzsimmons, "Snr-optimality of sum-of-squares reconstruction for phased-array magnetic resonance imaging," *J Magn Reson*, vol. 163, no. 1, pp. 121–3, 2003.
- [53] U. Koellisch, C. V. Gringeri, G. Rancan, E. V. Farell, M. I. Menzel, A. Haase, M. Schwaiger, and R. F. Schulte, "Metabolic imaging of hyperpolarized  $[1-^{13}\text{C}]$ acetate and  $[1-^{13}\text{C}]$ acetylcarnitine - investigation of the influence of dobutamine induced stress," *Magn Reson Med*, 2014.

- [54] M. A. Schroeder, H. J. Atherton, M. S. Dodd, P. Lee, L. E. Cochlin, G. K. Radda, K. Clarke, and D. J. Tyler, "The cycling of acetyl-coenzyme a through acetylcarnitine buffers cardiac substrate supply: a hyperpolarized  $^{13}\text{C}$  magnetic resonance study," *Circ Cardiovasc Imaging*, vol. 5, no. 2, pp. 201–9, 2012.
- [55] F. Lundquist, N. Tygstrup, K. Winkler, K. Mellempgaard, and S. Munck-Petersen, "Ethanol metabolism and production of free acetate in the human liver," *J Clin Invest*, vol. 41, pp. 955–61, 1962.
- [56] T. L. Miller and M. J. Wolin, "Pathways of acetate, propionate, and butyrate formation by the human fecal microbial flora," *Appl Environ Microbiol*, vol. 62, no. 5, pp. 1589–92, 1996.
- [57] S. E. Knowles, I. G. Jarrett, O. H. Filsell, and F. J. Ballard, "Production and utilization of acetate in mammals," *Biochem J*, vol. 142, no. 2, pp. 401–11, 1974.
- [58] J. M. Berg, J. L. Tymoczko, and L. Stryer, *Biochemistry*. New York: W. H. Freeman, 6th ed., 2007.
- [59] P. J. Randle, P. B. Garland, C. N. Hales, and E. A. Newsholme, "The glucose fatty-acid cycle. its role in insulin sensitivity and the metabolic disturbances of diabetes mellitus," *Lancet*, vol. 1, no. 7285, pp. 785–9, 1963.
- [60] J. Sakamoto, R. L. Barr, K. M. Kavanagh, and G. D. Lopaschuk, "Contribution of malonyl-coa decarboxylase to the high fatty acid oxidation rates seen in the diabetic heart," *Am J Physiol Heart Circ Physiol*, vol. 278, no. 4, pp. H1196–204, 2000.
- [61] H. Sochor, H. R. Schelbert, M. Schwaiger, E. Henze, and M. E. Phelps, "Studies of fatty acid metabolism with positron emission tomography in patients with cardiomyopathy," *Eur J Nucl Med*, vol. 12 Suppl, pp. S66–9, 1986.
- [62] V. G. Davila-Roman, G. Vedala, P. Herrero, L. de las Fuentes, J. G. Rogers, D. P. Kelly, and R. J. Gropler, "Altered myocardial fatty acid and glucose metabolism in idiopathic dilated cardiomyopathy," *J Am Coll Cardiol*, vol. 40, no. 2, pp. 271–7, 2002.
- [63] C. R. Santos and A. Schulze, "Lipid metabolism in cancer," *FEBS J*, vol. 279, no. 15, pp. 2610–23, 2012.
- [64] J. V. Swinnen, T. Roskams, S. Joniau, H. Van Poppel, R. Oyen, L. Baert, W. Heyns, and G. Verhoeven, "Overexpression of fatty acid synthase is an early and common event in the development of prostate cancer," *Int J Cancer*, vol. 98, no. 1, pp. 19–22, 2002.

- [65] J. Czernin, M. R. Benz, and M. S. Allen-Auerbach, "Pet imaging of prostate cancer using 11c-acetate," *PET Clin*, vol. 4, no. 2, pp. 163–172, 2009.
- [66] B. Mohsen, T. Giorgio, Z. S. Rasoul, L. Werner, G. R. Ali, D. K. Reza, and S. Ramin, "Application of c-11-acetate positron-emission tomography (pet) imaging in prostate cancer: Systematic review and meta-analysis of the literature," *BJU Int*, vol. 112, no. 8, pp. 1062–72, 2013.
- [67] C. V. Gringeri, U. Koellisch, A. Frank, R. F. Schulte, A. Haase, M. Schwaiger, and M. Menzel, "Detection of Prostate Tumor Metabolism Using Hyperpolarized [1-13C]Acetate," *Proceedings of the International Society for Magnetic Resonance in Medicine*, vol. 22, p. 2801, 2014.
- [68] G. J. Crystal, J. M. Silver, and M. R. Salem, "Mechanisms of increased right and left ventricular oxygen uptake during inotropic stimulation," *Life Sci*, vol. 93, no. 2-3, pp. 59–63, 2013.
- [69] J. L. Hall, W. C. Stanley, G. D. Lopaschuk, J. A. Wisneski, R. D. Pizzurro, C. D. Hamilton, and J. G. McCormack, "Impaired pyruvate oxidation but normal glucose uptake in diabetic pig heart during dobutamine-induced work," *Am J Physiol*, vol. 271, no. 6 Pt 2, pp. H2320–9, 1996.
- [70] G. W. Goodwin, C. S. Taylor, and H. Taegtmeyer, "Regulation of energy metabolism of the heart during acute increase in heart work," *J Biol Chem*, vol. 273, no. 45, pp. 29530–9, 1998.
- [71] R. Azuero, C. Debata, M. Quinn, K. McDonough, J. Thomson, and D. Penn, "Dobutamine alters carnitine metabolism in the neonatal piglet heart," *Can J Physiol Pharmacol*, vol. 82, no. 7, pp. 493–501, 2004.
- [72] J. R. Neely and H. E. Morgan, "Relationship between carbohydrate and lipid metabolism and the energy balance of heart muscle," *Annu Rev Physiol*, vol. 36, pp. 413–59, 1974.
- [73] V. K. Murthy and G. Steiner, "Hepatic acetate levels in relation to altered lipid metabolism," *Metabolism*, vol. 22, no. 1, pp. 81–4, 1973.
- [74] M. M. Awan and E. D. Saggerson, "Malonyl-coa metabolism in cardiac myocytes and its relevance to the control of fatty acid oxidation," *Biochem J*, vol. 295 ( Pt 1), pp. 61–6, 1993.
- [75] P. Shreve, P. C. Chiao, H. D. Humes, M. Schwaiger, and M. D. Gross, "Carbon-11-acetate pet imaging in renal disease," *J Nucl Med*, vol. 36, no. 9, pp. 1595–601, 1995.

- [76] W. J. Yin, F. Liu, X. M. Li, L. Yang, S. Zhao, Z. X. Huang, Y. Q. Huang, and R. B. Liu, "Noninvasive evaluation of renal oxygenation in diabetic nephropathy by bold-mri," *Eur J Radiol*, vol. 81, no. 7, pp. 1426–31, 2012.
- [77] C. Laustsen, K. Lipso, J. A. Ostergaard, R. Norregaard, A. Flyvbjerg, M. Pedersen, F. Palm, and J. H. Ardenkjaer-Larsen, "Insufficient insulin administration to diabetic rats increases substrate utilization and maintains lactate production in the kidney," *Physiol Rep*, vol. 2, no. 12, 2014.
- [78] D. R. Ball, B. Rowlands, M. S. Dodd, L. Le Page, V. Ball, C. A. Carr, K. Clarke, and D. J. Tyler, "Hyperpolarized butyrate: A metabolic probe of short chain fatty acid metabolism in the heart," *Magn Reson Med*, vol. 71, no. 5, pp. 1663–9, 2014.
- [79] J. A. Bastiaansen, M. E. Merritt, and A. Comment, "Real time measurement of myocardial substrate selection in vivo using hyperpolarized  $^{13}\text{C}$  magnetic resonance," *Journal of Cardiovascular Magnetic Resonance*, vol. 17, no. Suppl 1, p. O15, 2015.
- [80] K. M. Brindle, S. E. Bohndiek, F. A. Gallagher, and M. I. Kettunen, "Tumor imaging using hyperpolarized  $^{13}\text{C}$  magnetic resonance spectroscopy," *Magnetic Resonance in Medicine*, vol. 66, no. 2, pp. 505–519, 2011.
- [81] M. E. Merritt, C. Harrison, C. Storey, A. D. Sherry, and C. R. Malloy, "Inhibition of carbohydrate oxidation during the first minute of reperfusion after brief ischemia: Nmr detection of hyperpolarized  $^{13}\text{CO}_2$  and  $\text{H}^{13}\text{CO}_3^-$ ," *Magnetic Resonance in Medicine*, vol. 60, no. 5, pp. 1029–1036, 2008.
- [82] M. I. Kettunen, D.-e. Hu, T. H. Witney, R. McLaughlin, F. A. Gallagher, S. E. Bohndiek, S. E. Day, and K. M. Brindle, "Magnetization transfer measurements of exchange between hyperpolarized  $[1-^{13}\text{C}]$  pyruvate and  $[1-^{13}\text{C}]$  lactate in a murine lymphoma," *Magnetic Resonance in Medicine*, vol. 63, no. 4, pp. 872–880, 2010.
- [83] O. Warburg, "On the origin of cancer cells," *Science*, vol. 123, no. 3191, pp. 309–314, 1956.
- [84] O. Warburg, F. Wind, and E. Negelein, "Uber den Stoffwechsel von Tumouren im Korper," *Klinische Wochenschrift*, vol. 5, pp. 829–832, 1926.
- [85] C. H. Meyer, J. M. Pauly, A. Macovskiand, and D. G. Nishimura, "Simultaneous spatial and spectral selective excitation," *Magnetic Resonance in Medicine*, vol. 15, no. 2, pp. 287–304, 1990.
- [86] W. Block, J. Pauly, A. Kerr, and D. Nishimura, "Consistent fat suppression with compensated spectral-spatial pulses," *Magnetic resonance in medicine*, vol. 38, no. 2, pp. 198–206, 1997.

- [87] C. H. Cunningham, A. P. Chen, M. Lustig, B. A. Hargreaves, J. Lupo, D. Xu, J. Kurhanewicz, R. E. Hurd, J. M. Pauly, S. J. Nelson, *et al.*, “Pulse sequence for dynamic volumetric imaging of hyperpolarized metabolic products,” *Journal of magnetic resonance*, vol. 193, no. 1, pp. 139–146, 2008.
- [88] A. Z. Lau, A. P. Chen, R. E. Hurd, and C. H. Cunningham, “Spectral-spatial excitation for rapid imaging of dnp compounds,” *NMR in biomedicine*, vol. 24, no. 8, pp. 988–996, 2011.
- [89] R. F. Schulte, J. I. Sperl, E. Weidl, M. I. Menzel, M. A. Janich, O. Khagai, M. Durst, J. H. Ardenkjaer-Larsen, S. J. Glaser, A. Haase, M. Schwaiger, and F. Wiesinger, “Saturation-recovery metabolic-exchange rate imaging with hyperpolarized [1-13c] pyruvate using spectral-spatial excitation,” *Magn Reson Med*, vol. 69, no. 5, pp. 1209–16, 2013.
- [90] P. E. Larson, A. B. Kerr, A. P. Chen, M. S. Lustig, M. L. Zierhut, S. Hu, C. H. Cunningham, J. M. Pauly, J. Kurhanewicz, and D. B. Vigneron, “Multiband excitation pulses for hyperpolarized 13c dynamic chemical-shift imaging,” *Journal of magnetic resonance*, vol. 194, no. 1, pp. 121–127, 2008.
- [91] K. Weiss, A. Sigfridsson, L. Wissmann, J. Busch, M. Batel, M. Krajewski, M. Ernst, and S. Kozerke, “Accelerating hyperpolarized metabolic imaging of the heart by exploiting spatiotemporal correlations,” *NMR in Biomedicine*, vol. 26, no. 11, pp. 1380–1386, 2013.
- [92] J. Pauly, D. Nishimura, and A. Macovski, “A k-space analysis of small-tip-angle excitation,” *Journal of Magnetic Resonance*, vol. 213, no. 2, pp. 544–557, 2011.
- [93] R. F. Schulte and F. Wiesinger, “Direct design of 2d rf pulses using matrix inversion,” *J Magn Reson*, vol. 235, pp. 115–20, 2013.
- [94] Y. F. Yen, S. J. Kohler, A. P. Chen, J. Tropp, R. Bok, J. Wolber, M. J. Albers, K. A. Gram, M. L. Zierhut, I. Park, V. Zhang, S. Hu, S. J. Nelson, D. B. Vigneron, J. Kurhanewicz, H. A. Dirven, and R. E. Hurd, “Imaging considerations for in vivo 13c metabolic mapping using hyperpolarized 13c-pyruvate,” *Magn Reson Med*, vol. 62, no. 1, pp. 1–10, 2009.
- [95] Y. S. Levin, D. Mayer, Y.-F. Yen, R. E. Hurd, and D. M. Spielman, “Optimization of Fast Spiral Chemical Shift Imaging Using Least Squares Reconstruction: Application for Hyperpolarized 13C Metabolic Imaging,” *Magnetic Resonance in Medicine*, vol. 58, no. 2, pp. 245–252, 2007.
- [96] D. Mayer, Y.-F. Yen, J. Tropp, A. Pfefferbaum, R. E. Hurd, and D. M. Spielman, “Application of Subsecond Spiral Chemical Shift Imaging to Real-Time Multislice Metabolic Imaging of the Rat In Vivo after Injection of

- Hyperpolarized  $^{13}\text{C}$ -Pyruvate,” *Magnetic Resonance in Medicine*, vol. 62, no. 3, pp. 557–564, 2009.
- [97] M. Durst, U. Koellisch, C. V. Gringeri, A. Frank, G. Rancan, E. V. Farell, V. Karas, F. Wiesinger, M. I. Menzel, A. Haase, M. Schwaiger, and R. F. Schulte, “Comparison of acquisition schemes for hyperpolarised  $^{13}\text{C}$  imaging,” *NMR in Biomedicine*, p. doi: 10.1002/nbm.3301, 2015.
- [98] W. T. Dixon, “Simple proton spectroscopic imaging,” *Radiology*, vol. 153, no. 1, pp. 189–194, 1984.
- [99] S. B. Reeder, J. H. Brittain, T. M. Grist, and Y.-F. Yen, “Least-Squares Chemical Shift Separation for  $^{13}\text{C}$  Metabolic Imaging,” *Journal of Magnetic Resonance Imaging*, vol. 26, no. 4, pp. 1145–1152, 2007.
- [100] F. Wiesinger, E. Weidl, M. I. Menzel, M. A. Janich, O. Khagai, S. J. Glaser, A. Haase, M. Schwaiger, and R. F. Schulte, “Ideal spiral csi for dynamic metabolic mr imaging of hyperpolarized  $[1-^{13}\text{C}]$ pyruvate,” *Magn Reson Med*, vol. 68, no. 1, pp. 8–16, 2012.
- [101] U. Koellisch, R. F. Schulte, M. Durst, A. Haase, and F. Wiesinger, “Joint Field Map and Metabolite Image Reconstruction Framework for Hyperpolarized  $^{13}\text{C}$  Spiral CSI,” *Proceedings of the International Society for Magnetic Resonance in Medicine*, vol. 22, p. 3453, 2014.
- [102] K. Derby, J. Tropp, and C. Hawryszko, “Design and evaluation of a novel dual-tuned resonator for spectroscopic imaging,” *Journal of Magnetic Resonance (1969)*, vol. 86, no. 3, pp. 645–651, 1990.
- [103] T. Lanz, M. Durst, and M. Müller, “A 16 Channel Cardiac Array for Accelerated Hyperpolarised  $^{13}\text{C}$  Metabolic Imaging on Pigs at 3T,” *Proceedings of the International Society for Magnetic Resonance in Medicine*, vol. 21, p. 3947, 2013.
- [104] S. Bowen and J. H. Ardenkjaer-Larsen, “Formulation and utilization of choline based samples for dissolution dynamic nuclear polarization,” *J Magn Reson*, vol. 236, pp. 26–30, 2013.
- [105] U. Koellisch, C. V. Gringeri, G. Rancan, M. Durst, M. Menzel, M. Schwaiger, A. Haase, and R. F. Schulte, “Hyperpolarized  $^{13}\text{C}$ -acetate for the detection of metabolic response of the heart to a stress protocol,” *Proceedings of the International Society for Magnetic Resonance in Medicine*, vol. 22, p. 988, 2014.
- [106] J. A. Bastiaansen, T. Cheng, and A. Comment, “In Vivo Real Time Cardiac Metabolism Using Hyperpolarized Acetate,” *Proceedings of the International Society for Magnetic Resonance in Medicine*, vol. 20, p. 4324, 2012.

- [107] Q. Qin, "Point spread functions of the  $t_2$  decay in k-space trajectories with long echo train," *Magnetic resonance imaging*, vol. 30, no. 8, pp. 1134–1142, 2012.
- [108] K. Nagashima, "Optimum pulse flip angles for multi-scan acquisition of hyperpolarized nmr and mri," *J Magn Reson*, vol. 190, no. 2, pp. 183–8, 2008.
- [109] S. O. Rice, "Mathematical analysis of random noise," *Bell System Technical Journal*, vol. 23, no. 3, pp. 282–332, 1944.
- [110] J. Sijbers, A. J. den Dekker, P. Scheunders, and D. Van Dyck, "Maximum-likelihood estimation of rician distribution parameters," *IEEE Trans. Med. Imaging*, vol. 17, no. 3, pp. 357–361, 1998.
- [111] K. M. Brindle, "Nmr methods for measuring enzyme kinetics in vivo," *Progress in nuclear magnetic resonance spectroscopy*, vol. 20, no. 3, pp. 257–293, 1988.
- [112] M. Durst, U. Koellisch, C. Gringeri, M. A. Janich, G. Rancan, A. Frank, F. Wiesinger, M. I. Menzel, A. Haase, and R. F. Schulte, "Bolus tracking for improved metabolic imaging of hyperpolarised compounds," *Journal of Magnetic Resonance*, vol. 243, pp. 40–46, 2014.
- [113] E. Croteau, S. Gascon, M. Bentourkia, R. Langlois, J. A. Rousseau, R. Lecomte, and F. Benard, "[ $^{11}\text{C}$ ]acetate rest-stress protocol to assess myocardial perfusion and oxygen consumption reserve in a model of congestive heart failure in rats," *Nucl Med Biol*, vol. 39, no. 2, pp. 287–94, 2012.
- [114] A. M. Coffey, M. L. Truong, and E. Y. Chekmenev, "Low-field mri can be more sensitive than high-field mri," *Journal of Magnetic Resonance*, vol. 237, pp. 169–174, 2013.
- [115] S. Duewel, P. Christ, U. Koellisch, M. Durst, C. V. Gringeri, F. Schilling, , M. Menzel, R. F. Schulte, S. Glaser, M. Schwaiger, and A. Haase, "Thermal  $t_1$  measurements for frequently used  $^{13}\text{C}$  hyperpolarization agents at clinically available field strengths," *Proceedings of the International Society for Magnetic Resonance in Medicine*, vol. 22, p. 4442, 2014.
- [116] U. Koellisch, R. F. Schulte, M. Durst, A.-L. J.H., F. Frijia, L. Menichetti, M. Lombardi, A. Haase, and F. Wiesinger, "3D Whole-Heart Cardiac Metabolic Imaging with [ $^{13}\text{C}$ ]pyruvate using IDEAL Spiral CSI," *Proceedings of the International Society for Magnetic Resonance in Medicine*, vol. 21, 2013.
- [117] A. Flori, F. Frijia, V. Lionetti, J. H. Ardenkjaer-Larsen, V. Positano, G. Giovannetti, R. F. Schulte, F. Wiesinger, F. A. Recchia, L. Landini, *et al.*, "Dnp

methods for cardiac metabolic imaging with hyperpolarized [1-13c]pyruvate large dose injection in pigs,” *Applied Magnetic Resonance*, vol. 43, no. 1-2, pp. 299–310, 2012.

- [118] G. D. Aquaro, F. Frijia, V. Positano, L. Menichetti, M. F. Santarelli, J. H. Ardenkjaer-Larsen, F. Wiesinger, V. Lionetti, S. L. Romano, G. Bianchi, *et al.*, “3d cmr mapping of metabolism by hyperpolarized 13c-pyruvate in ischemia–reperfusion,” *JACC: Cardiovascular Imaging*, vol. 6, no. 6, pp. 743–744, 2013.
- [119] D. J. Scholz, M. A. Janich, U. Köllisch, R. F. Schulte, J. H. Ardenkjaer-Larsen, A. Frank, A. Haase, M. Schwaiger, and M. I. Menzel, “Quantified ph imaging with hyperpolarized 13c-bicarbonate,” *Magnetic Resonance in Medicine*, 2014.
- [120] A. Flori, M. Liserani, S. Bowen, J. H. Ardenkjaer-Larsen, and L. Menichetti, “Dissolution dynamic nuclear polarization of non-self-glassing agents: Spectroscopy and relaxation of hyperpolarized [1-13c] acetate,” *The Journal of Physical Chemistry A*, vol. 119, no. 10, pp. 1885–1893, 2015.



# List of Publications

## Full Papers First Author / Joined Authorship:

- Metabolic Imaging of Hyperpolarized [1-<sup>13</sup>C]Acetate and [1-<sup>13</sup>C]Acetylcarnitine - Investigation of the Influence of Dobutamine Induced Stress  
**Ulrich Koellisch\***, Concetta V. Gringeri\*, Giaime Rancan, Eliane V. Farrell, Marion I. Menzel, Axel Haase, Markus Schwaiger, Rolf F. Schulte  
\*both authors contributed equally  
Magnetic Resonance in Medicine, 2014, doi: 10.1002/mrm.25485. [Epub ahead of print]
- Comparison of Acquisition schemes for Hyperpolarized <sup>13</sup>C Imaging  
Markus Durst\*, **Ulrich Koellisch\***, Annette Frank, Giaime Rancan, Concetta V. Gringeri, Vincent Karas, Florian Wiesinger, Marion I. Menzel, Axel Haase, Markus Schwaiger, Rolf F. Schulte  
\*both authors contributed equally  
NMR in Biomedicine, 2015, doi: 10.1002/nbm.3301. [Epub ahead of print]
- Investigation of Metabolic Changes in STZ Induced Diabetic Rats with Hyperpolarized [1-<sup>13</sup>C]Acetate  
**Ulrich Koellisch**, Christoffer Laustsen, Thomas S. Nørtinger, Concetta V. Gringeri, Marion I. Menzel, Rolf F. Schulte, Axel Haase, and Hans Stødkilde-Jørgensen  
Physiological Reports, 3 (2015), e12474.

## Conference Abstracts (only first author):

- Hyperpolarized <sup>13</sup>C-Acetate for the Detection of Metabolic Response of the Heart to a Stress Protocol  
**Ulrich Koellisch**, Concetta V. Gringeri, Giaime Rancan, Markus Durst, Eliane V. Farrell, Marion I. Menzel, Axel Haase, Markus Schwaiger, Rolf F. Schulte  
"Magna cum Laude" Awarded Oral Presentation at 22<sup>nd</sup> Joint Annual Meeting of the International Society for Magnetic Resonance in Medicine (ISMRM) 2014, Milan, Italy.
- Investigation of Metabolic Changes in STZ Induced Diabetic Rats with Hyperpolarized [1-<sup>13</sup>C]Acetate  
**Ulrich Koellisch**, Christoffer Laustsen, Thomas S. Nørtinger, Concetta V. Gringeri, Marion I. Menzel, Rolf F. Schulte, Axel Haase, and Hans Stødkilde-Jørgensen  
Traditional Poster Presentation at the 23<sup>rd</sup> Joint Annual Meeting of the International Society for Magnetic Resonance in Medicine (ISMRM) 2015, Toronto, Canada.

- Joint Field Map and Metabolite Image Reconstruction Framework for Hyperpolarized  $^{13}\text{C}$  Spiral CSI  
**Ulrich Koellisch**, Rolf F. Schulte, Markus Durst, Axel Haase, and Florian Wiesinger  
 Traditional Poster Presentation at the 22<sup>nd</sup> Joint Annual Meeting of the International Society for Magnetic Resonance in Medicine (ISMRM) 2014, Milan, Italy.
- 3D Whole-Heart Cardiac Metabolic Imaging in the Pig with  $[1-^{13}\text{C}]$ pyruvate using IDEAL Spiral CSI  
**Ulrich Koellisch**, Rolf F. Schulte, Markus Durst, Jan H. Ardenkjaer-Larsen, Francesca Frijia, Luca Menichetti, Massimo Lombardi, Axel Haase and Florian Wiesinger  
 Electronical Poster Presentation at the 21<sup>st</sup> Joint Annual Meeting of the International Society for Magnetic Resonance in Medicine (ISMRM) 2013, Salt Lake City, US.
- Design of a double-resonant  $^{19}\text{F}$ - $^1\text{H}$  resonator for in vivo MRI detection of amyloid plaques at 17.6T  
**Ulrich Koellisch**, Volker C. Behr, Cornelius Faber Traditional Poster Presentation at the 9<sup>th</sup> International Conference on Magnetic Resonance Microscopy, 2007, Aachen, Germany.

### Full-Papers Coauthored

- Bolus tracking for improved metabolic imaging of hyperpolarised compounds  
 Markus Durst, **Ulrich Koellisch**, Concetta Gringeri, Martin A. Janich, Giaime Rancan, Annette Frank, Florian Wiesinger, Marion I. Menzel, Axel Haase, Rolf F. Schulte  
 Journal of Magnetic Resonance, 243 (2014), 40-46.
- Diffusion of hyperpolarized  $^{13}\text{C}$ -metabolites in tumor cell spheroids using real-time NMR spectroscopy  
 Franz Schilling, Stephan Düwel, **Ulrich Koellisch**, Markus Durst, Rolf F. Schulte, Steffen J. Glaser, Axel Haase, Angela M. Otto, Marion I. Menzel  
 NMR in Biomedicine, 26 (2013), 557-68.
- Quantified pH imaging with hyperpolarized  $^{13}\text{C}$ -bicarbonate  
 David J. Scholz, Martin A. Janich, **Ulrich Koellisch**, Rolf F. Schulte, Jan H. Ardenkjaer-Larsen, Annette Frank, Axel Haase, Markus Schwaiger, Marion I. Menzel  
 Magnetic Resonance in Medicine, 2014, doi: 10.1002/mrm.25357. [Epub ahead of print]



## Acknowledgements

Here, I gratefully would like to thank all the people that supported me during the thesis:

- *Prof. Dr. Axel Haase* for his support and trust throughout the years as my scientific supervisor.
- *Dr. Rolf Schulte, Dr. Marion Menzel* and *Dr. Florian Wiesinger* for their scientific support and intensive feedback.
- *Prof. Dr. Markus Schwaiger, Dr. Kim Muñoz Alvarez, Annette Frank, Eliane Farell* and all the other people from Klinikum rechts der Isar for their help with in vivo experiments and medical questions.
- *Prof. Dr. Hans Stødkilde-Jørgensen, Dr. Christoffer Laustsen* and *Thomas Nørlinger* for their support and kindness during my stay in Aarhus.
- *Dr. Luca Menichetti, Dr. Francesca Frijia* and the MR-Team of the CNR in Pisa for their support during the experiments.
- *Markus* for the fruitful MR-related discussions.
- *Concetta, Tim, Stephan, Johannes, Markus, Christian, Patrick* and *BERTI* for being great colleagues inside and outside the office at the IMETUM and GRC.
- *Tim, Markus, Johannes, Nico* and *Benjamin* for the very exciting and high-class scientific meetings.
- All the people of the GEGRC and the IMETUM for the friendly working atmosphere.

Furthermore, I would like to acknowledge all the financial and material support, I received from the GEGRC, at the IMETUM, the BMBF (grant 13EZ1114) and the grant of the COST (action TD1103).